Surface-Enhanced Raman Spectroscopy of Analytes in Blood

A DISSERTATION
SUBMITTED TO THE FACULTY OF
UNIVERSITY OF MINNESOTA
BY

Antonio Renteria Campos II

IN PARTIAL FULFILLMENT OF THE REQUIREMENTS
FOR THE DEGREE OF
DOCTOR OF PHILOSOPHY

Christy L. Haynes, Advisor

April 2015

Acknowledgements

First and foremost, I would like to thank my advisor Professor Christy Haynes. Her relentless work ethic and guidance have been remarkable to experience. Thank you for allowing me to be apart of an amazing research experience and research group.

Secondly, I would like to the members of the Haynes group. In particular, I would like to thank Kyle Bantz and Audrey Meyer for their help when I first joined the group. Through a rough transition period, both Kyle and Audrey helped me tremendously.

Thirdly, I would like to thank the many collaborators that I have had the privilege of working with on many projects. To name a few: Professor Richard Van Duyne, Bhavya Sharma, Anne-Isabelle Henry, Marty Blaber, Rong Zhuang, Nathan Greeneltch, Professor George Schatz, Professor Milan Mrksich, Professor Cathy Murphy, Professor R. Lee Penn and Professor Sang-Hyun Oh. Thank you for the opportunities.

Fourthly, I acknowledge and thank all of the co-authors and contributors to the work contained within this document including: Dr. Dongyuk Kim, Dr. Ashish Datt, Cassandra Knutson, Ryan Knutson, Dr. Zhe Gao, Matt Styles, Sam Egger, and Nathan Klein.

I thank my parents for the support that they have given me throughout my graduate career. My father has supported me financially throughout my undergraduate and graduate life, and I have lived a much more comfortable life because of him.

Finally, I would like to thank the friends that have supported me throughout my research career. Brian Woods and Maria Miranda, thank you for the support when graduate school seemed like a misguided dream. Jeremy Bedard, thank you for the good times. Ryan and Cassie Knutson, thank you for all of the support and help. Drew Thompson, thank you for the puns. Jake, Sam, Dan, Arlon, and Claudia Gilk, thank you for showing me Minnesota.

Dedication

For my parents,
Antonio and Beatrice, always supportive, in all of my endeavors

For my sisters,
April and Monica, thank you for putting up with me

Abstract

Although Raman scattering has traditionally been considered a weak process, making analysis of low concentration analytes in complex matrices difficult, both methodological and instrumentation advances in the last couple decades have made Raman spectroscopy a viable and useful analytical tool. This is especially true for analyte species within aqueous environments because the Raman scattering cross-section of water is small; one particular example of a critical aqueous environment is analysis of and in blood. The work detailed in Chapter 1 will analyze much of the literature related to Raman analysis in blood within the last 20 years, including normal Raman, surface-enhanced Raman, and spatially offset Raman analyses. The first section will focus on direct analysis of blood samples, including determining the age of deposited or donated blood and blood content within body fluid mixtures. The second section will discuss intrinsic Raman-based detection of small molecules and protein analytes within blood as well as extrinsic Raman detection of tumors. The last section will review the recent use of spatially offset Raman and surface-enhanced spatially offset Raman spectroscopy to analyze molecular analytes, tissue, bone, tumors, and calcifications, including *in vivo* analysis. This focal point closes with perspective on critical gaps and upcoming developments for Raman analysis in blood. Raman detection in blood can be applied to different forensic fields and can also be used for the detection of foreign analytes.

In current events, ricin has been discussed frequently because of letters sent to high-ranking government officials containing the easily extracted protein native to castor beans. Ricin B chain, commercially available and not dangerous when separated from the

A chain, enables development of ricin sensors while minimizing the hazards of working with a bioterror agent that does not have a known antidote. As the risk of ricin exposure, common for soldiers, becomes increasingly common for civilians, there is a need for a rapid, real-time detection of ricin. To this end, aptamers have been used recently as an affinity agent to enable the detection of ricin in food products *via* surface-enhanced Raman spectroscopy (SERS) on colloidal substrates. One goal of this work is to extend ricin sensing into whole human blood; this goal required application of a commonly used plasmonic surface, the silver film-over-nanosphere (AgFON) substrate, which offers SERS enhancement factors of 10^6 in whole human blood for up to 10 days. This aptamer-conjugated AgFON platform enabled ricin B chain detection for up to 10 days in whole human blood. Principle component analysis (PCA) of the SERS data clearly identifies the presence or absence of physiologically relevant concentrations of ricin B chain in blood. In addition to the detection of ricin B chain at a relevant concentration, the development of a platform to perform a single experiment calibration curve was performed through the combination of microfluidic devices with SERS substrates.

Microfluidic sensing platforms facilitate parallel, low sample volume detection using various optical signal transduction mechanisms. Herein, we introduce a simple mixing microfluidic device, enabling serial dilution of introduced analyte solution that terminates in five discrete sensing elements. We demonstrate the utility of this device with on-chip fluorescence and surface-enhanced Raman scattering (SERS) detection of analytes, and we demonstrate device use both when combined with a traditional inflexible SERS substrate and with SERS-active nanoparticles that are directly

incorporated into microfluidic channels to create a flexible SERS platform. The results indicate, with varying sensitivities, that either flexible or inflexible devices can be easily used to create a calibration curve and perform a limit of detection study with a single experiment.

In Chapter 4, the synthesis of an ultrastable and reversible pH nanosensor using gold nanosphere aggregates functionalized with 4-mercaptobenzoic acid (MBA) that are encapsulated in mesoporous silica was performed. The pH nanosensor is stable and functional in human whole blood for a period of more than 3 months.

With the growing interest in nanoparticles and nanomaterials, a demonstration was organized for a high school AP Chemistry class. Spectrophotometry and colorimetry experiments are common in high school and college chemistry courses. Previous work has demonstrated that handheld camera devices can be used to quantify the concentration of a colored analyte in solution in place of traditional spectrophotometric or colorimetric equipment. Chapter 5 extends this approach to an investigation of a mesogold mineral supplement. With the addition of free Google applications, the investigation provides a feasible, sophisticated lab experience, especially for teachers with limited budgets.

Table of Contents

List of Figures

List of Tables

Chapter 1. Raman Spectroscopy of Blood

1.1 Introduction

Until the 1980s, Raman spectroscopy was limited in its scope for use in chemical analysis due to relatively low signal strength, background fluorescence, and inefficient light collection and detection.[7] While the most common detection techniques at the time were based upon the use of fluorescent tags and immunoassays, Raman spectroscopy was still pursued because it yield direct, intrinsic information about measured analytes i.e., each molecule has a unique combination of molecular vibrations leading to a spectroscopic fingerprint. While infrared absorption spectroscopy also reveals molecular characteristics, Raman spectroscopy offers a distinct advantage over infrared spectroscopy because it can be used to analyze aqueous solutions. The small Raman scattering cross-section of water (5.33×10^{27} cm^2/molecule sr) minimizes background interference from the matrix, allowing analysis of bodily fluids, which are complex mixtures of cells, proteins, enzymes, and small molecules in water.[91]

Utilizing this advantage, Raman spectroscopy has recently been employed to detect a myriad of analytes in biological systems, encouraging the application of Raman spectroscopy in biosensors. A biosensor is composed of a recognition element and a signal transducer. Binding of the target analyte to the recognition element generates a signal (e.g. electrons, light, mass effect) that is then detected by the transducer. Common examples of recognition elements include antibodies, enzymes, nucleic acids, aptamers, and other synthetic molecules. Common transducers include electrodes for

electrochemical sensors and CCD cameras for optical sensors.[2] Employing a recognition element for specific binding reveals not only molecular binding, but can also sometimes reveal critical characteristics of the binding event. Biosensors can exploit either extrinsic or intrinsic detection of the target analyte. Extrinsic detection methods, such as fluorescent tags, often require knowledge of the sample to be analyzed and also the identity of analyte that is to be detected. In contrast, intrinsic detection can be utilized to help ascertain the contents of a sample when minimal information is known about the sample. An area of study where minimal sample information is often the case is in forensics.

The use of Raman spectroscopy for forensic chemistry applications has recently gained popularity because of the technical advantages of the method, including the non-destructive nature of the measurements, minimal sample quantity required, rapid analysis, on-site identification (with the advent of portable Raman spectrometers), and the ability to distinguish different bodily fluids as well as mixtures of bodily fluids.[26] The most common bodily fluid found at crime scenes is blood, and the identification of mixtures of bodily fluids can be accomplished by comparing samples to a database of Raman spectra from bodily fluid components while at a crime scene. To this end, analysis of the different components of bodily fluids and, most commonly, blood can be useful to ascertain the age and origin of the fluid (i.e. the difference between venous blood and menstrual blood). Beyond identifying and dating blood, Raman spectroscopy can also be used to detect and identify analytes present in blood. The scope of this review is to detail

how Raman spectroscopy is being used to identify blood, blood components, and analytes in blood; the review also includes analysis in body tissue because of the complexity of interstitial fluid for analysis.

1.2 Raman Spectroscopy Overview

Vibrational Raman spectroscopy is the measurement of inelastic scattering of light during molecular vibrations. This phenomenon was predicted theoretically by Smekal in 1923, but was not observed until 1928 by Raman and Krishnan.[3-5] Because both offer a fingerprint identity of molecular vibrations of samples, Raman and IR spectroscopy are similar; however, unlike IR, Raman scattering is a two-photon process. While the absorption of photons translates directly into vibrational energy in IR, Raman scattering occurs as the interaction of the electric field of the incoming light induces a change in the polarizability of the molecule, thereby creating an induced dipole.[6] This virtual state of the molecule is not a true quantum state, but can be considered to be a very short-lived distortion of the electron cloud of the molecule by the incoming electric field of light.[7] The radiation emitted from this induced dipole moment contains both Stokes and anti-Stokes Raman scattered light as well as Rayleigh scattered light.

The drawback of Raman spectroscopy is the inherently low signal intensity; only one Raman scattered photon results from 10^{10} input photons.[6,8] To overcome the low signal strength, many techniques have been developed, including surface-enhanced Raman (SERS), surface-enhanced resonant Raman spectroscopy (SERRS), coherent anti-stokes Raman (CARS), hyper-Raman, and tip-enhanced Raman (TERS).[9-12] These

techniques rely on modifications of traditional normal Raman scattering and the advancement of instrumentation, including laser technology. Herein, rather than consider all the technique variations used in Raman spectroscopy, we focus on the techniques that make analysis of blood components and analytes in blood a possibility, including normal Raman, SERS, spatially offset Raman spectroscopy (SORS), and the related surface-enhanced spatially offset Raman spectroscopy (SESORS).

Both chemical and electromagnetic mechanisms contribute to the enhancement seen from SERS (with typical enhancements ranging from 10^6-10^8).[6,9,13] The chemical enhancement is predicted to provide an enhancement factor of about 100 and necessitates that the molecule is directly adsorbed to a noble metal surface. In the chemical mechanism, a charge-transfer state is created between the adsorbate and the metal surface, providing a pathway for a Raman transition. Some in the SERS community believe that the contributions of the chemical mechanism are minimal, especially when compared to electromagnetic enhancement.

In ensemble measurements of SERS, the electromagnetic enhancement mechanism can be correlated with the localized surface plasmon resonance (LSPR) of a noble-metal substrate near Raman-active analytes. Conduction band electrons in the substrate collectively oscillate upon excitation by a certain wavelength of light, determined by the composition, structure (size and shape), and spatial relationships of substrate components, generating large electromagnetic (EM) fields at the surface of the material. These EM fields influence the analyte induced dipole and are capable of

generating enhancements on the order of 10000 or greater compared to normal Raman scattering by the same molecule. Ag and Au are frequently used plasmonic substrates because they have convenient visible or near-infrared extinction wavelengths that match well with easily available lasers and detectors.

The plasmonic properties of SERS substrates are very sensitive to nanoscale roughness features, and control in fabrication of nanoscale features has improved significantly in recent years. A plethora of different fabricated nanostructures can be found in the literature including but not limited to nanparticle aggregates, on-wire lithography (OWLS), immobilized nanorod assemblies (INRA), and film-over-nanospheres (FONs).[14-19] Among the various substrate morphologies, there is a need to reproducibly fabricate substrates capable of stable performance in complex biological environments such as blood.

1.3 Analysis of Blood with Traditional Methods

Before reviewing Raman as a blood analysis tool, it will useful to first explore the current gold standard methods for blood analysis. Chemical analysis (both qualitative and quantitative) of blood is important to understand certain biological systems and for diagnostic purposes (including forensics).[20-24] Forensic identification of blood at crime scenes is performed first with a presumptive test, followed by a confirmatory test.[25-28] Presumptive tests such as those performed with luminol[29-32] can help to identify blood that is not clearly visible. However, luminol can generate false positives.[26]

To confirm the identity of the presumed blood, a test specific to blood must be performed. The simplest method to confirm the identity of blood is by identifying the red and white blood cells along with fibrin using a microscope.[33,34] Alternative methods to confirm the identity of blood include scanning electron microscopy (SEM), energy dispersive x-ray (EDX), crystallization, UV-vis, ELISA assays, and chromatography.[26] Of these methods, the most common method is crystallization of the blood. Of the crystallization techniques, the most popular are the Teichman and Takayama tests.[30,33] These tests rely on the formation of either rhombic or needle-shaped crystals under certain alkaline conditions;[34] however, the crystal tests for blood are susceptible to under and over-heating of the samples and require an experienced technician to perform the test correctly.

Recently, Raman spectroscopy has been utilized as a non-destructive and label-free method to evaluate body fluids for the purposes of forensic identification.[25] Raman spectroscopy has recently been shown to be a promising confirmatory test for blood. Both the Teichman and Takayama tests require a larger amount of blood than for Raman sampling and require modification to the sample ahead of analysis. In addition, blood has a unique Raman spectrum that can be distinguished from other body fluids such as saliva, sweat, semen and vaginal fluid.[25,27,28,35,36] Moreover, Raman facilitates the distinction between mixtures of body fluids and pure blood.[26]

Table 1.1 Components in blood and components that are Raman active.

Blood Components	Concentration Male	Concentration Female	Raman Active? Y/N	References
Hemoglobin* (Heme) (g/100 ml of blood)	16.3	14.5	Yes	20, 26, 27, 38, 41, 43
Phenylalanine*			Y	38
Glucose*			Y	37
Proerythroblasts	0-3.4		-	21
Normoblasts -Early -Intermediate -Late	 0-20.4 0-25		-	21
Myeloblasts	0-2.8		-	21
Promyelocytes	1.2-6.8		-	21
Myelocytes -Neutrophilic -Eosinophilic	 4.0-16.4 0-1.8		-	21
Metamyelocytes	3-10		-	22
Band cells	17-33		-	22
Segmented cells -Neutrophilic -Eosinophilic -Basophilic	 5-25 0-4 0-0.5		-	22
Lymphocytes	1.5-19.1		-	21
Monocytes	0-4		-	22
Megakaryocytes	0.03-3.00		-	23
Plasma cells	0-4.1		-	21
Reticulum cells	0.2-2.0		-	23
Unclassified cells	0-0.5		-	24

*Cells, % of total cell count

1.4 SERS

Blood observed after drying in the presence of Au nanoparticles shows a spectrum very similar to normal Raman of red blood cells: the approximate ratio of RBCs to WBCs to platelets is 600:1:40.[41,42] In this work, the authors observed several key differences

between normal Raman and SERS of RBCs. In particular, the normal Raman measurements exhibit bands that are not present in the SERS spectrum such as the amide I (1654 cm^{-1} shift), the CH_2/CH_3 amino acid deformation modes (1450 cm^{-1} shift), ν_{20} (1399 cm^{-1} shift), and the ν Fe-O_2 (568 cm^{-1} shift). The peaks that appear strong in the SERS spectrum, but not in the normal Raman spectrum, are 1513, 551, 1471, and 496 cm^{-1} shift bands. Although the authors do not assign the new vibrational bands present in the SERS spectrum to particular functional groups, they do mention many red shifts of certain vibrational bands when comparing normal Raman to SERS spectra. The "new" peaks in the SERS spectrum may possibly be attributed to vibrational modes present in the normal Raman spectrum, but with dramatic frequency shifts due to contact with the Au surface. The authors also hypothesize that the contributions found in the SERS spectrum could result from cell membrane components (glycoproteins, glycolipids, spectrin, cholesterol, phospholipids, transmembrane proteins, etc), which would be in contact with the Au surface; while the size of a RBC is on the order of several microns, SERS enhancement arises from only within about 5 nm from the Au surface.

SERS analysis of human whole blood has been performed by Ziegler et al.[38] Interestingly, these researchers observed that the dominant vibrational features in the recorded spectra can be attributed to changes in the vibrational bands of hypoxanthine over the course of 24 hours when blood was adsorbed onto Au nanoparticles.

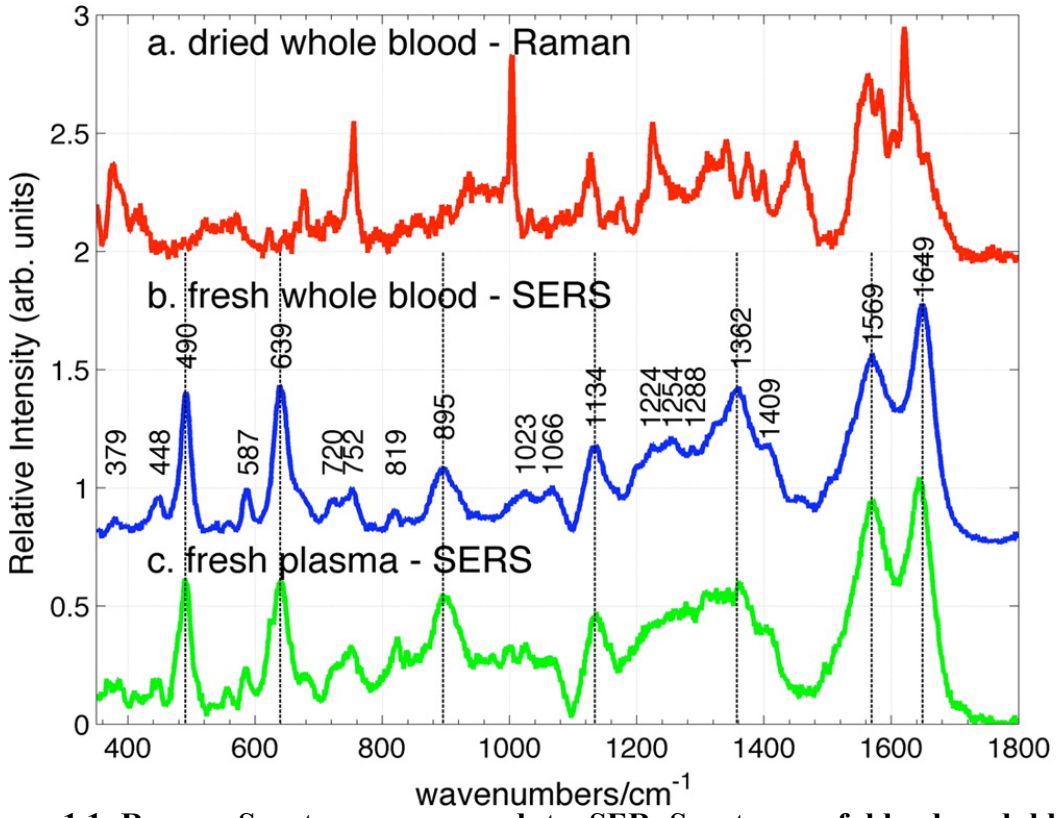

Figure 1.1 Raman Spectrum compared to SER Spectrum of blood and blood components

Hypoxanthine is the product of purine degradation in the plasma,[28] and is the major peak observed after about 10-20 hours aging of blood. In contrast, normal Raman spectra of human whole blood is dominated by oxyhemoglobin.[28,39,40] The hypoxanthine changes in the SERS spectrum observed from whole human blood can also be measured from plasma alone. The change in intensity of the hypoxanthine signal is not a linear

response with time; in fact, a dramatic increase in the intensity of the hypoxanthine signal is observed after about 15 hours of blood storage.[41] It is important to note that the authors did not observe the same hypoxanthine peaks when the surface was incubated with only RBC solutions (in saline or PBS) over the course of 1 day. While these studies reveal an interesting time dependent change of blood over the course of 24 hours, the blood donations used in this work are from only 2 individuals. Comparison of these results with a larger sample size would be interesting to observe the generality of these spectral signatures. If generalizable, this method of evaluation could be used in forensics as a time marker for the age of a blood sample.[43]

In addition to the peaks from hypoxanthine, peaks from uric acid can also be measured in blood samples.[43] Bonifacio et al compared silver nanoparticles incubated with uric acid and silver nanoparticles incubated with filtered serum and found that the peaks not attributed to hypoxanthine or heme can be attributed to uric acid.[43] The identification of the unknown peaks in blood has also shown that variations of the concentration of uric acid from person to person can affect the amount of uric acid observed.[43] Variation of the uric acid concentration between males and females is observed based on the intensity of the 637 and 1132 cm^{-1} peaks. [43] However, these variations from person to person and gender may be used as an analytical technique to quickly ascertain changes in uric acid levels after treatment for certain diseased people. [43] This person-to-person variability, however, may complicate the use of SERS forensic analysis of blood. Previously envisioned experiments using blood as a forensic

identification of blood based on age, source, and gender need to be examined further in future work.

Table 1.2 Observed Vibrational Bands of "Normal" (Non-SERS) Raman Spectrum of Whole Human Blood (Liquid Drop and Dried Blood) at 785 nm

Observed Band[b] (cm^{-1})	**Intensity**	**Assignment[a]**	**Observed Band[b] (cm^{-1})**	**Intensity**	**Assignment[a]**
347[d]	M	ν_8	1127[d], 1129[e]	m	ν_5
380[d]	W	$\delta(C_\beta C_c C_d)$	1173	w	ν30
417	M	δ(Fe-O-O)	1212[e]	m	$\nu_5 + \nu_{18}$
570	W	ν(Fe-O_2)	1224	w[e], m[d]	$\nu_{13} + \nu_{42}$
621	W	ν_{12}	1305[e], 1311[d]	w	ν_{21}
674[e], 677[d]	M	ν_7	1338[e], 1341	m	ν_{41}
716	W	λ_{11}	1374[d], 1377[e]	m[d], vw[e]	ν_4
754	S	ν_{15}	1398	m	ν_{20}
788	W	ν_6	1450	s	$\delta(CH_2/CH_3)$
825[e]	W	λ_{10}	1523[e]	m	ν_{38}
856	W		1545[e]	s	ν_{11}
900	W	p:C-C skeletal	1563	s	ν_{19}
937	M	ν_{46}	1582	m	ν_{37}
1003	S	phenylalanine	1605[e], 1603[d]	m	$\nu(C_a=C_b)$

1030	W	$\delta(=C_bH_2)_{asym}$	1621	s	$\nu(C_a=C_b)$
1054	W	$\delta(=C_bH_2)_{asym}$	1638	m[d], w[e]	ν_{10}
1115[e]	W		1654	w	amide I

Table adapted from Premasiri, W. R., Ziegler, L. D., J Phys Chem B, 2012, 116, 9376. **Table key: protein (p) $C_{\omega b}$, C_β, and C_m (carbon atoms at the alpha, beta, and meso positions of porphyrins, respectively); C_a and C_b (vinyl group carbons). [b]Estimated person ±1 cm^{-1}. [d]Dried blood sample. [e]Liquid blood sample.**

Additional challenges to Raman detection of blood and blood components for forensic use is NIR laser excitation of dried human blood produces heme aggregates, thereby shifting porphyrin ring vibrational bands by several wavenumbers.[44] Once blood is removed from the biological system and is stored, many denaturation products are observed in the spectrum. One denaturation product is reported to be methemoglobin and can be observed with intense laser powers or with blood that has been stored.[44] The vibrational signature of dried blood can be attributed to a single protein, hemoglobin. Previously reported vibrational bands arising from fibrin were found to be present because of hemoglobin aggregates and not from fibrin. While the auto-oxidation of hemoglobin occurs in ambient conditions outside of the body, it is feasible to use this aging process to determine the age of the dried blood at crime scenes.

1.5 Analyte detection in Blood via Raman spectroscopy

Monitoring blood composition for early diagnosis of disease is essential for human health. One of the paramount interests in the field of clinical analysis is to improve the detection of analytes in blood. Due to the many components present in human whole blood, detection of specific analytes may be difficult. This section will include review of the literature pertaining to Raman detection of analytes in body fluids and offer insights into future directions.

There are many portable devices for blood testing, such as the home glucose level monitor, which is based on the oxidation of glucose by an enzyme and electrochemical detection of a reaction byproduct (H_2O_2). Other blood tests (for analytes other than glucose), in general, require a relatively large amount of blood (5-10 mL per sample for conventional blood tests) and use medical lab equipment, thereby increasing the cost and time of analysis. Moreover, it is difficult to monitor analytes in blood continuously using current detection methods.

Blood is a complex matrix. Although, water has minimal Raman absorption,[45] there is significant fluorescence background interference from other blood components. Gerd et al. used a near-infrared laser for excitation to minimize the fluorescence background.[46] The fluorescence background of blood serum was also less intense when excited with a 785 nm laser beam compared to the visible excitation light.[47-49]

Raman bands are much narrower than fluorescence bands, therefore it is possible to identify sharp and distinct Raman peaks even in the presence of a broad florescence

background without pre-treatment of blood. Firdous et al. used Raman for direct, in vitro assessement of human blood glucose levels; they compared the Raman blood serum spectra of normal, healthy diabetic, and diabetic patients with other malignancies like cancer and hepatitis, and revealed a reliable glucose signature in all cases.[54] The fluorescence and Raman signatures of proteins, lipids and other tissue content were present in the spectra. The featured peaks of glucose that appeared at 1168, 1463, 1531 cm^{-1} shift differentiated the diabetic patients from healthy diabetic patients. However, the fat adsorption and interactions with other blood components reduced the optical absorption of glucose, making accurate prediction of the blood glucose concentration impossible by this method.

1.6 Analyte detection in Blood by SERS

Amplification of the Raman signal of analytes in highly light scattering and absorbing media is required to improve the quality of detection. In an attempt to amplify the target signal via SERS, various noble metal substrates have been introduced into blood samples to detect various bloodborne analytes. For example, Wang et al. utilized the hotspots generated from Au nanorods (AuNR)-Au nanoparticle (AuNP) assemblies to detect thrombin in diluted human blood serum (5% human blood serum).[55] AuNRs were modified with anti-thrombin antibodies, and AuNPs were functionalized with both a thrombin-binding aptamer (TBA) and a Raman reporter (mercaptobenzoic acid, MBA). A sandwich structure of AuNR-antibody-thrombin-aptamer-AuNPs was formed in the

presence of thrombin. The AuNR–AuNP junctions generated strong electromagnetic fields, and the localized Raman reporters in this field produced an enhanced Raman signal. Using this method, subnanomolar (as 887 pM) thrombin was detected in diluted human blood serum. The need for diluted blood serum and added nanostructures clearly indicates further method development would have to be done before this method could be used in vivo. In another example, Yuen et al. reported low-concentration detection of paclitaxel, an anti-cancer drug, in blood plasma using polystyrene beads coated with Au.[51] Using SERS, the concentration of paclitaxel was determined based on the intensity of the characteristic Raman peak of paclitaxel at 1605 cm^{-1} shift (due to C=C stretching mode) to an accuracy of 3.8×10^{-9} M (root mean squared error of prediction, RMSEP) within the range of 1.0×10^{-8} to 1.0×10^{-7} M. Also, Ross et al. detected a synthetic pterin analogue in mouse serum.[56] Pteridines, aromatic heterocyclic molecules, play a key role in enzymatic pathways for the production of neuorotransmitters such as dopamine, serotonin, and epinephrine.[56] Au nanoparticles mixed were used to determine the pterin signals in solution in mouse serum were similar to the standard solution (prepared in water at a concentration of 1×10^{-8}), only with reduced signal intensity

When the target analyte has a resonance Raman signature,[40] it is possible to do in situ detection of analytes without any blood pretreatment. For example, Casella et al. reported using colloidal AgNPs as the substrate to detect beta-carotene and hemoglobin detection in whole blood.[57] Two excitation wavelengths, 514 and 785 nm, were used in acquiring Raman spectra of the samples. The spectral features of proteins were minimal

in the Raman spectrum recorded with 514 nm excitation, but were very intense with 785 nm excitation. Conversely, the signal of β-carotene was missing entirely in the Raman spectrum that was recorded with 785 nm excitation, but was present when excited by the 514 nm laser (Figure 1.4a). The resonance effects selectively enhance the Raman signals of β-carotene while Raman scattering from the blood components is comparatively weak when the excitation wavelength was 514 nm, which is very close to the absorption maximum in the UV-vis electronic spectrum of β-carotene. The normal Raman and SERS spectra of whole blood via 514 nm excitation are compared in Figure 2b. Although the excitation wavelength lies within the resonance range of β-carotene, the SERS spectra

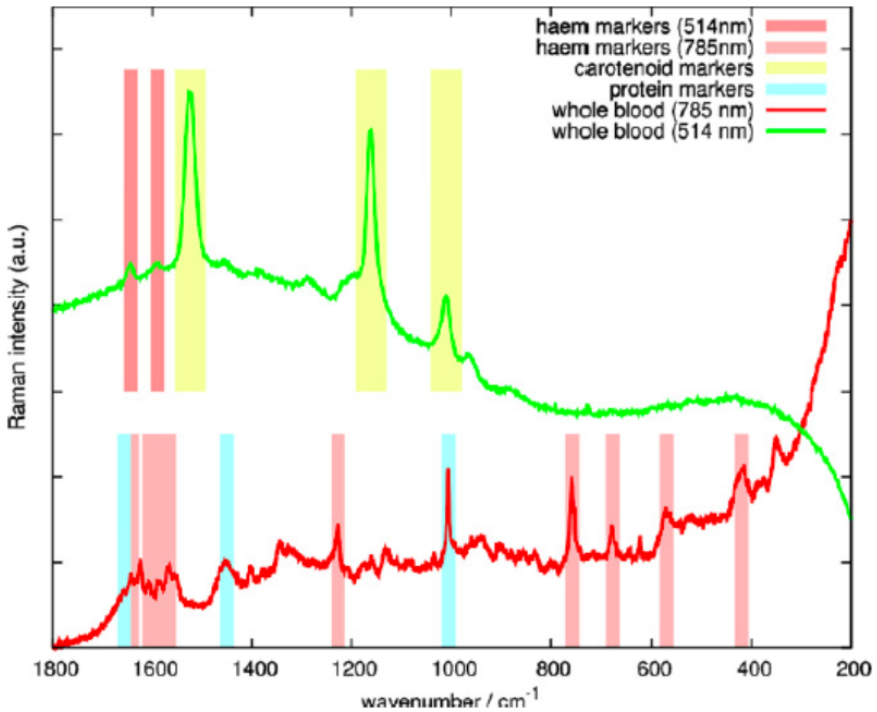

displayed more defined protein peaks rather than those of β-carotene.

a

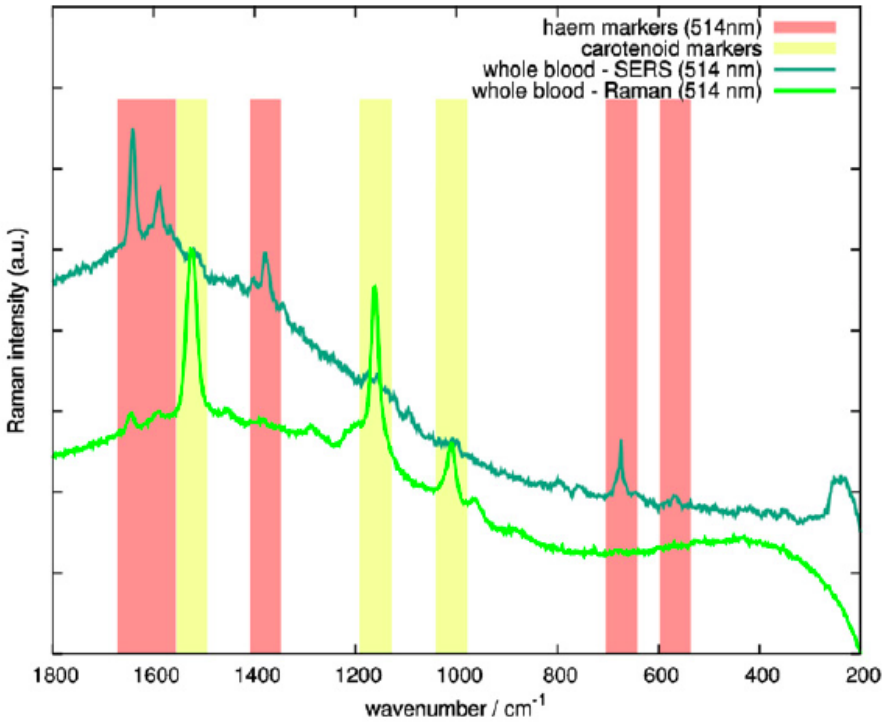

Figure 1.2. (a) Raman spectra of human whole blood excited by 514 and 785 nm laser. (b) Normal Raman spectrum and SERS spectrum of whole blood at 514 nm excitation.

The scattering and absorption by tissue limits excitation laser penetration depth and optical imaging *in vivo*. However, some strides have been made using SERS with well-chosen LSPRs. For example, Qian et al injected AuNPs with covalently bound Raman reporters into subcutaneous and deep muscular sites in live animals.[58] *In vivo* SERS spectra were obtained by focusing a 785 nm laser at the injection spots. After background subtraction, the obtained SERS spectral features, though lower in intensity,

were identical to the *in vitro* spectra. For *in vivo* SERS detection, the maximum depth of visualization reported to date is 1-2 cm.

Qian et al utilized PEGylated AuNPs for *in vivo* tumor detection in live animals. The thiolated PEG did not displace the Raman reporters (crystal violet, Nile blue, basic fuchsin and cresyl violet) that adsorbed on the surface of the AuNPs by electrostatic interaction and protected the Raman reporters from harsh conditions including acids, bases, high ionic strength and organic solvents. The targeting ligand on the AuNPs was a ScFv antibody, which can recognize the epidermal growth factor (EGFR) that is overexpressed in many types of tumor cells. They also found that the AuNPs provided much stronger emission intensity than quantum dots under the same experimental conditions.

Another way to minimize the background noise of blood is to extract the interested analytes from the blood. Gerd et al. detected various commonly applied drugs including codeine, dihydrocodeine, pipamperone, doxepine, citalopram, trimipramine, doxylamine, carbamazepine, and methadone in blood and urine by using the combination of high-performance liquid chromatography (HPLC) and SERS. The body fluids were first mixed with ethylacetate to extract the drugs into the oil layer. Since the extractions of the drugs of interest were not perfect, HPLC was performed on the extract to separate the mixture. HPLC analysis required at least 8 min for each separation of analytes at 5×10^{-8} M[50,51] and is not capable of identifying the analytes without a separate detection

method. The detection method used for this study was SERS because of its sensitivity and ability to distinguish structurally similar compounds.

Alternatively, if an analyte of interest is known then substrates can be functionalized to selectively extract the target. For example, Liu et al. used a SERS active substrate composed of Ag nanoparticles on arrays of anodic aluminum oxide (AAO) nanochannels functionalize with vancomycin, which can form hydrogen bonds with bacterial cell walls.[52] The bacteria were captured from blood and washed with water 5 times before SERS analysis. This allowed the group to efficiently remove the bacteria from the interfering media for analysis.

Reduction of the background of blood can also be achieved by simply removing the red blood cells and macromolecules. Hsu et al. applied silver colloidal nanoparticle-mediated SERS for rapid identification and quantification of lactic acid in human blood.[53] To reduce the background interference and improve the SERS resolution, the whole blood was first centrifuged to obtain serum and then ultrafiltration was applied to remove macromolecules from the blood. They achieved impressive accuracy of measuring lactic acid at the low physiological concentration of 0.55 mM.

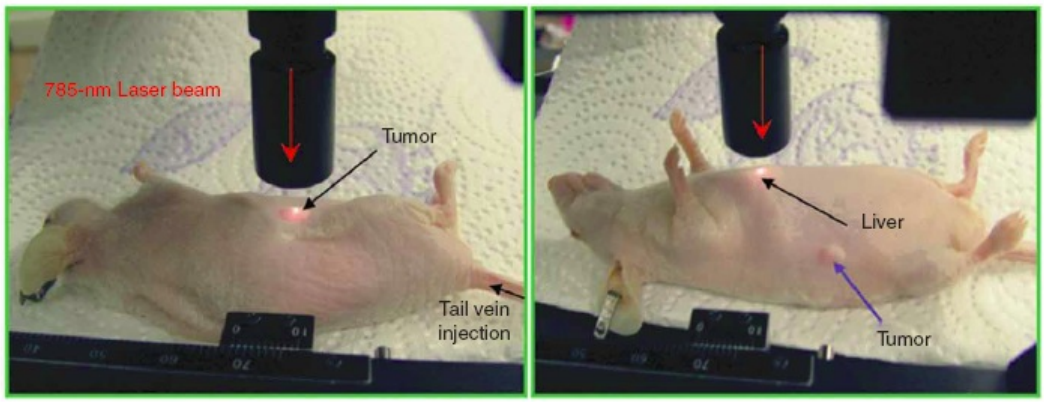

Figure 1.3. Photos of a live mouse with a AuNP injection. The laser beam is focusing on the tumor site and liver for SERS detection.

Developing Raman spectroscopy for sensing in blood has remained an elusive target. Although the application of Raman spectroscopy is still rare, these studies have demonstrated the utility of Raman spectroscopy for analyte detection in complex biological media. Achievement of accurate and detailed measurements of analytes for clinical usage requires the optimization of our techniques, specifically, amplification of signal intensity via SERS and the development of higher efficiency capture and target ligands.

1.7 SORS/SESORS/Transmission Raman

As previously mentioned, bio-media are highly heterogeneous and light scattering[59,60] making them extremely difficult to be analyzed by optical methods. Conventional Raman spectroscopy collects the photons scattered from the surface of a sample and is able to achieve information typically extending no more than a few millimeters into the sample due to the shallow penetration depth of the photons collected

in this way. Moreover, since the illumination and collection zones coincide, conventional Raman spectroscopy would also collect significant amount of fluorescence signal generated by the complex media leading to massive background noises. However, it is possible to utilize a modified Raman Spectroscopy technique, spatially offset Raman spectroscopy (SORS) to analyze the composition of the complex media and its components.

SORS is a technique that has been demonstrated to obtain Raman spectra from deeper layers of the sample and suppress fluorescence background.[61,62] Instead of collecting the photons directly from the backscattered light, SORS relies on the photons that emerge from positions that are spatially offset from the illumination spot. The photons that penetrate into the samples are scattered. As they propagate through a diffusely scattering media, the majority of the photons will be backscattered rapidly. Those photons not backscattered initially will diffuse through the media and emerge several centimeters away from the position of the incident laser. Consequently, the deeper the photons penetrate, the further they are emitted from the launch spot. The spectra acquired at different distances from the center point can provide details about the composition of the sample at different depths.

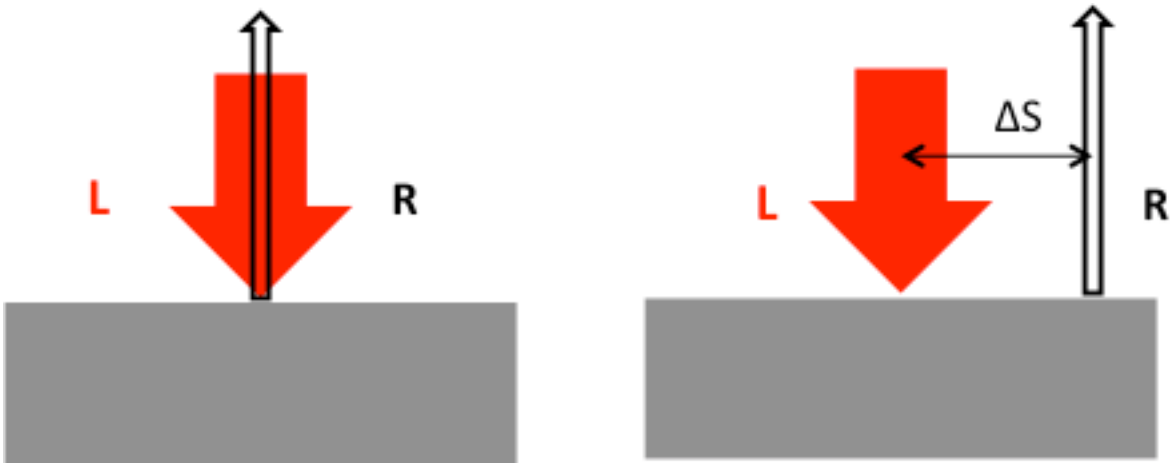

Figure 1.4. Normal Raman spectroscopy versus spatially offset Raman spectroscopy. The scheme shows the conventional backscattering Raman spectroscopy (left) and Spatial Offset Raman Spectroscopy (SORS, right). L stands for Laser and R stands for Raman. ΔS is the spatial offset.

Increasing the depth of penetration results in a wider distribution of photon emitting locations and significant attenuation of the intensity when photons diffuse through the media. Because a lower proportion of the incident photons reach farther depths, the resolution of SORS is quite limited. Usually, a set of SORS spectra are collected with ring fiber probes that are connected to different CCDs; Results vary between each individual CCD.[63] Distortion of post-processed SORS spectra also lowers the detection resolution of SORS.

The idea of inverse-SORS was introduced by Matousek[64] and Schulmerich et al.[65] They proposed that instead of illuminating the laser source in one spot and collecting the

spectra in a circle of a given radius, the fiber probes could be located at the center while the laser beam was supplied in a ring shape centered at the collection spot. The spatial offset can be simply accomplished by changing the radius of the laser ring. Since the excitation laser is spread over a larger area compared to point laser excitation, higher laser power would be used while maintaining the power density under the threshold of biological safety. Inverse-SORS shows significant improvement in the detection limit.

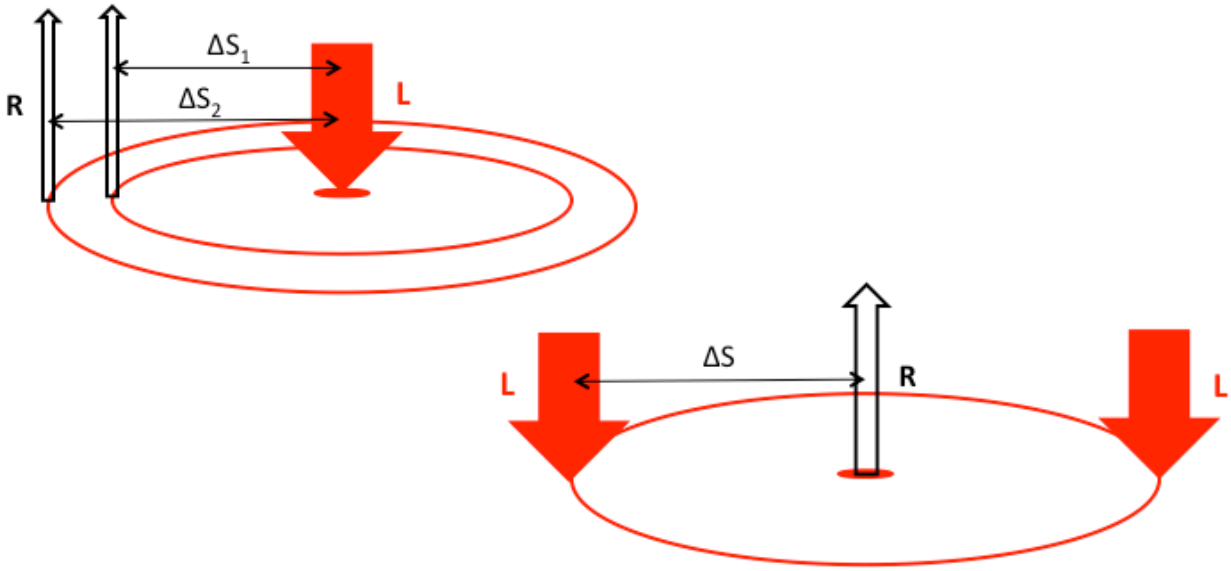

Figure 1.5. SORS variation of delta S based on the depth of penetration of the photons (upper-left) and inverse SORS (lower-right). Comparison of SORS and inverse SORS. delta S1 and delta S2 are spatial offsets of Raman scattering from different depths of the sample.

Transmission Raman spectroscopy is considered as a special case of SORS (Figure 1.3).[64] Instead of collecting photons from the incident surface, the photons that

pass through the sample are collected on the opposite side of the sample and therefore the overall bulk sample information is obtained by transmission Raman spectroscopy.

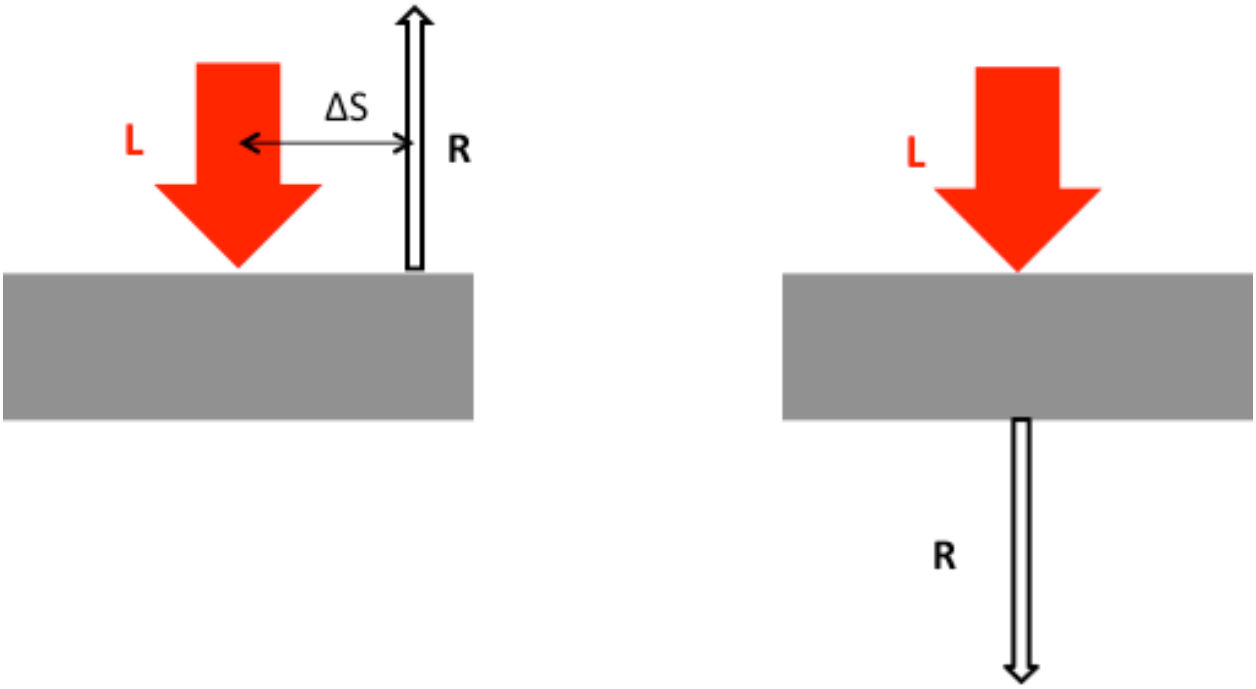

Figure 1.6. Diagram of SORS (left) and transmission Raman (right).

Current non-invasive clinical screening methods are unable to provide accurate and detailed chemical information of tissue components, such as veins, bones and other subsurface tissues. Because of the ability to analyze samples at different depths, SORS can be used in detecting analytes in concealed containers,[66] e.g., identifying the composition of encapsulated medicine or differences in tissue composition in vivo.[67] Successful attempts to screen analytes in plastic containers, the properties of non-invasive detection, clinically relevant detection depths, and low laser power density, permit the

application of SORS for in vivo monitoring of the chemical compositions of living tissues.[68,69]

Thus far, the bio-probing properties of SORS in and through bones and breast tissues have been investigated. Matousek et al[70] demonstrated the feasibility of SORS to obtain *in vivo* Raman spectra from human bones. The spectra were collected by ring fiber probe with zero and 3 mm spatially offset and acquired using a 2 mW laser beam for 200 seconds- far below the threshold for skin safety. The skin tissue signals and the fluorescence background were effectively minimized by the subtraction of spectra from the zero- offset spectra. Despite low-quality processed bone spectra, the results demonstrate a proof-of-concept trial requiring further research on the topic of SORS bone diagnosis.

Probing through soft tissues is more challenging than the flat and relatively simple composition of bones. Researchers have devoted significant effort towards developing techniques to diagnose breast cancer via SORS. The similarity between tumors and other soft tissue make distinguishing between them difficult. Keller et al. first demonstrated the possibility of discerning cancer tissue beneath as much as 2 millimeters of normal breast tissue.[71] Later, they developed a Monte Carlo code, which predicts the photon propagation, to evaluate the SORS performance in soft tissue.[72] Combining their numerical simulation and multi-separation SORS probe improved the sensitivity of the tumor signatures.[73]

Aside from direct detection of tumors using Raman spectroscopy, breast cancer may also be diagnosed by analyzing the calcification induced by benign tumors. The research of Holme et al.[74] demonstrated the relation between microcalcification and tumor metastasis. Different compositions of calcification deposits reflect the level and location of tumor cells.[75,76] Accurate diagnosis of breast cancer is possible by analysis of calcium deposits using SORS. Stone et al. demonstrated the feasibility of SORS to distinguish different calcification types through chicken breast and skin.[77] Note, the above two groups both used chicken breast as a sample tissue. However, chicken breast does not fully represent human breast tissue. Therefore, *in vivo* detection of breast cancer cells in human by SORS remains a challenge.

Surface-enhanced spatially offset Raman spectroscopy (SESORS) is a new methodology that combines SORS with SERS to accomplish deeper probe depth and higher detection sensitivity. The feasibility of SESORS was first introduced[78] and demonstrated by the Matousek group; they recovered the Raman signal from a 20 mm thick porcine tissue using a combination of signal enhancement from injected SERS active nanoparticles and transmission Raman spectroscopy.[79] The Van Duyne group expanded the applications of SESOR to include in vivo glucose sensing[51,80] and imaging through bones.[81] A silver film-over-nanosphere (AgFON) substrate functionalized with decanethiol (DT), and 6-mercapto-1-hexanol (MH) was implanted beneath the skin of rats. The transcutaneous glucose concentration was controlled by intravenous infusion of glucose or insulin. The SESORS measurements of glucose in the blood of a rat were

consistent with the readings from a home glucose level reader and achieved a successful 17-day continuous monitoring of glucose levels.

The detection of Raman reporter tagged nanoparticles through bones via SESORS was recently reported by the Van Duyne group. Silica coated 90 nm gold cores with trans-1,2-bis(4-pyridyl)- ethylene (BPE) as the Raman reporter were injected into the tissues adjacent to an ovine shoulder bone. Due to the surface plasmon enhancement, the Raman signal of BPE was detected through the bone with a maximum thickness of 8 mm. The authors propose using SESORS detection for *in vivo* detection of analytes in human brain tissue (with average skull thicknesses ranging from 3-8 mm). The prospects for SORS as an efficient non-invasive medical imaging and analysis tool remain promising; despite no reports of using SORS for blood analysis, it still has enormous potential for *in vivo* blood detection through skin tissue and veins.

1.8 Analysis of other bodily fluids

Recent work on SERS biosensing has resulted in extensive literature focused on applications in human blood plasma, seminal plasma, whole blood, and interstitial fluid. Low-level detection of several medicinal compounds has been achieved using SERS on blood plasma samples including the detection of apomorphine, used in treating Parkinson's disease, by adding silver colloid to a plasma sample following thin layer chromatography.[82] SERS immunosensors have been used in blood plasma by Li et al., to detect human immunoglobulin G (IgG) and the vascular endothelial growth factor, a biomarker for tumor angiogenesis. Using Au@Raman reporter@SiO_2 nanoparticles

coupled with a gold triangle nanoarray, a sandwich-assay was constructed with a reported limit of detection of 7 fg/mL IgG.[83]

Without a focus on specific biomarkers, computational methods for processing data can also help enhance and distinguish spectral features. For example, principle component analysis (PCA) of SERS spectra has been used in conjunction with membrane electrophoresis to analyze and distinguish blood plasma of healthy patients from patients with gastric cancer.[84] Zeng and coworkers have also combined PCA with linear discriminant analysis in the detection of nasopharyngeal, gastric, and cervical cancers from blood plasma samples.[85-87] This technique has been applied to seminal plasma, using polarized SERS to analyze semen quality.[88]

1.9 Future directions

There are many current methods that can be applied for the detection of components already present in blood such as handheld glucose monitors. Two branches of future technology include the detection of foreign analytes such as bacterial infections without the need for culturing the bacteria and blood diagnosis without the need for drawing blood. Culturing bacteria is often time consuming and treatment is delayed until the amount of live cultures can be assessed and analyzed facilitating the need for broad-spectrum antibiotics given to the patient. To give an example of these applications of SERS to human whole blood, two recent methods for the identification of bacteria in blood samples are: bimetallic silver-gold SERS surfaces were used by Sivanesan et al. with antibiotic coatings to selectively capture and identify E. coli, S. enterica, and S.

epidermidis;[89] and Yang and coworkers utilized a microfluidic platform and electrokinetic concentration to rapidly identify S. aureus, E. coli, and P. aeurignosa.[90]

Examples of blood diagnosis without the need for drawing blood have been mentioned previously thru the use of SESORS, these nanoparticles were functionalized with a widely used Raman reporter. In order to expand the technology towards the analysis of common blood tests such as glucose monitoring, cholesterol measurements, and other biomarkers there is a need to develop stable and sensitive nanoparticles able to withstand the blood environment while being able to remain in tact long enough to conduct measurements and biocompatible as to not cause harm to the patient.

Chapter 2. Surface-Enhanced Raman Spectroscopy Detection of Ricin B Chain in Human Blood

2.1 Introduction

Ricin is a naturally occurring toxin that is found in the castor bean to protect the plant from pests. The detailed protein structure and the mechanism of its toxicity have been extensively and thoroughly studied over the last two decades.[1-3] This globular protein is comprised of two chains linked by a single disulfide bond.[4] Ricin A chain is the ribosome-inactivating toxin that inhibits protein synthesis, while ricin B chain is a lectin that attaches to galactose residues on the cell surface facilitating entry.[5] Both chains are necessary for *in vivo* toxicity. [1,6-10] Once the protein translocates into a cell's cytosol, one molecule of ricin is sufficient to kill that cell. The median lethal dose (LD50) of crude ricin in mice is 8 μg/kg by injection and 10 μg/kg by inhalation.[11,12] After exposure to a lethal dose of ricin, the time to death is typically 60-90 hours.[13] The relative ease of extraction and isolation of ricin, combined with the ubiquitous presence of the castor plant, make ricin an easily obtainable and frequently used bioterror agent. Ricin is considered the third-most toxic substance due to its toxicity and abundance according to the U.S. Environmental Protection Agency and the Center for Defense Information.[14-17] Thus, rapid and easy-to-apply diagnosis of ricin infection in a bio-matrix like whole human blood remains a priority. Many methods have been developed to detect ricin in various media, including mass spectrometry, cell culture assays, and immunochemical

assays.[18,19] Most of the methods to detect ricin can be confounded by complex biological environments and a lack of accuracy. Enzyme-linked immunosorbent assays (ELISA) are the current commercial method in ricin detection. By using an antibody, ELISA is able to detect ricin selectively and sensitively. However, the antibody is expensive and sensitive to the environment, and non-specific interactions with other proteins or molecules and large variance also limits the application of this method in complex matrices.

Aptamers are short single DNA or RNA strands that, like antibodies, have specific affinity to analytes ranging from small inorganic molecules to proteins or even whole cells.[20,21] Aptamers show many advantages in the analytical detection applications competing with traditional antibody-based methods. In contrast to antibodies, aptamers are easily synthesized in high purity and modified with desired functional groups. Unlike antibodies, aptamers are more stable at various conditions and can reversibly fold and unfold.

Sreevatsan et al. selected an aptamer specific to ricin B chain (RBC) from a combinatorial oligonucleotide library by systematic evolution of ligands by exponential enrichment (SELEX).[22,23] This RBC aptamer is a 40-mer (5'-ACACCCACCGCAGGCAGACGCAACGCCTCGGAGACTAGCC-3') that contains a bulge loop and a hairpin loop, and it is thermally stable from 4-63 °C. The thiolated RBC aptamer used in the experiments presented herein were heated up to 95 °C for 5 minutes to fully unfold the hairpin structure and submerged in ice water to fold the aptamer into the most stable conformation prior to the modification of the substrate. Previous work

with this aptamer showed that it is able to detect 30 ng/mL of RBC from several liquid food matrices.[22-24] The authors also demonstrated that the RBC aptamer was capable of detecting intact ricin (even though it was developed using only ricin B chain) and demonstrated that this aptamer sequence had a binding constant better than other reported ricin aptamers and comparable to the current commercial ELISA antibodies.

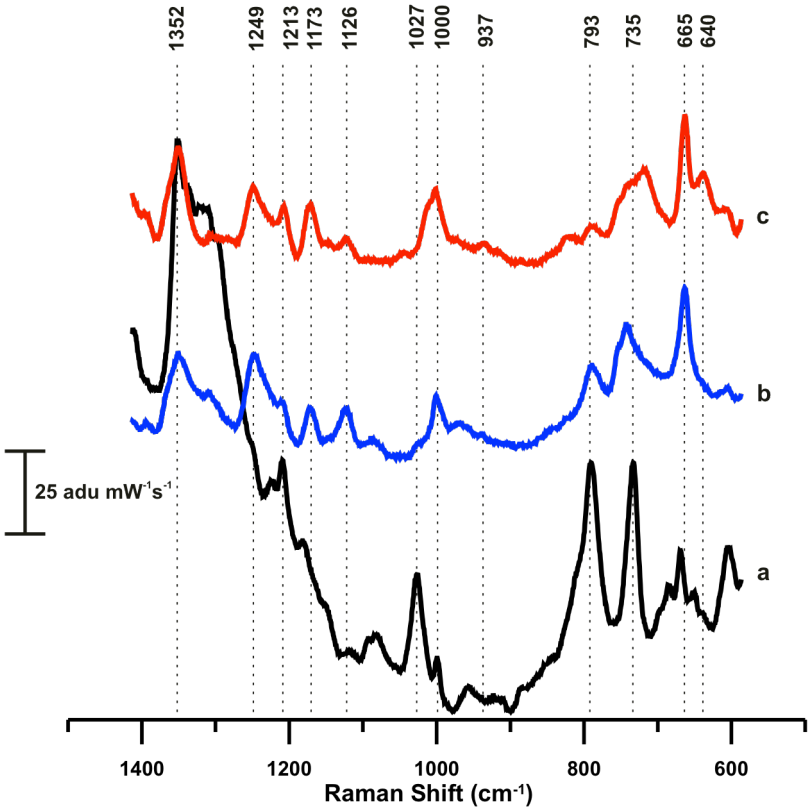

Figure 2.1. SERS on a AgFON of (a) ricin B chain aptamer (b) ricin B chain aptamer in blood and (c) ricin B chain aptamer in blood spiked with 1 μg/mL of ricin B chain. Spectra are vertically offset for clarity, λ_{ex} = 633 nm. Each trace is the average of 7 randomly chosen spots on the AgFON.

Upon binding to the target analyte, the conformational change of aptamers can be detected by various optical analysis methods. The Labuza group reported the use of the RBC aptamer and surface-enhanced Raman spectroscopy (SERS) to detect ricin in food matrices.[23] Because the Raman

scattering cross-section of water is very small, SERS is a promising label-free detection method for analyte detection in aqueous environments, including both food matrices and blood.[25,26] Especially, when one needs immediate detection, SERS as an optical analysis method shows a distinct time advantage over the conventional methods that would require culturing cells prior to detection. An additional advantage of using the aptamer affinity agent is that aptamers are small compared to antibodies, meaning that captured analytes are more likely to be detected by SERS, where signal exponentially decays with the distance between the analyte and the noble metal surface.

To efficiently detect and monitor ricin in the human body, it is desirable to capture and detect ricin directly in whole human blood; however, this is likely to be challenging based on the biological complexity of blood. Several research groups have successfully used SERS to detect analytes in simpler body fluids. For example, Ridente et al detected trace amount of amphotericin B, a drug for fungal infections in dilute plasma, *via* surface-enhanced resonance Raman spectroscopy in dilute plasma.[27,28] Also, Trachta et al combined the techniques of SERS and HPLC to detect codeine and carbazepine in human blood and urine.[29] Recently, several groups have reported SERS measurements in whole human blood. Liu et al utilized a vancomycin-coated SERS substrate to capture and detect bacteria from human blood without interference from blood cells.[19] Casella et al were able to recognize and assign the fundamental features of β-carotene and the blood protein hemoglobin in human blood by SERS.[30] Wang et al and Sha et al both reported the detection of circulating tumor cells in blood, relying on AuNPs conjugated with a

Raman-active tag.[31,32] Herein, ricin B chain captured by the aptamer-modified AuFON is directly detected by SERS in whole human blood. This study also includes consideration of the reversibility of binding between ricin B chain and the aptamer-modified SERS substrates. While the detection of RBC is exciting, this general approach could easily be adapted to detect other bloodborne protein targets.

2.2 Experimental:

2.2.1 SERS Substrates:Ag Film-over-Nanospheres

Silver film-over-nanospheres (AgFON) substrates were fabricated as has been previously reported.[33,34] Briefly, a silicon wafer was cleaned with a water:ammonium hydroxide: 30% hydrogen peroxide (10:1:1) mixture under sonication for 60 minutes. The wafers were thoroughly rinsed with water followed by silica microsphere (Thermo Scientific, Waltham, MA) drop coating. Typically, 1-10 μL of the silica microsphere solution was drop cast onto the wafer followed by gentle agitation/mixing and allowed to air dry. Silver metal (200 nm thick, 99.999% Ag Kurt J Lesker, Clairton, PA) was deposited with a vacuum evaporation chamber (Denton Vacuum, Moorestown, NJ) equipped with a quartz crystal microbalance. Ahead of aptamer modification, freshly fabricated AgFONs were plasma cleaned using argon gas for 4-6 minutes in a plasma chamber.[35] Then, 10-40 μM ricin B chain aptamer solution (5'ACA CCC ACC GCA GGC AGA CGC AAC GCC TCG GAG ACT AGC C3' dithiol spacer, Integrated DNA Technologies, Coralville, IA) was added to the plasma-cleaned AgFONs and incubated

at 4 °C overnight followed by rinsing with nuclease-free (Integrated DNA Technologies) water. The functionalized-AgFONs were then dried with a gentle stream of nitrogen gas.

2.2.2 Ricin B Chain Incubation Experiments

Individual AgFONs functionalized with the aptamer were incubated in either nuclease-free water, buffer, or whole human blood. The solution was then spiked with a known concentration of ricin B chain (Vector Laboratories, Burlingame, CA) and gently mixed by swirling. Following the defined incubation time, the AgFON was removed from the solution and rinsed with copious amounts of nuclease-free water. The AgFON was then dried with nitrogen gas ahead of SERS interrogation.

2.2.3 Surface-enhanced Raman Spectroscopy Measurements

Raman spectra were acquired using a 632.8 nm HeNe excitation laser (Research Electro-Optics, Inc, Boulder, Colorado) that passed through an interference filter (Melles-Griot, Rochester, NY) ahead of direction to the sample using an aluminum-coated prism (final laser spot size on the sample was 1.26 mm^2). The Raman scattered light was focused using a 50 mm-diameter achromatic lens (Nikon, Melville, NY), and the Rayleigh scattered light was rejected with a notch filter (Semrock, Rochester, NY). A 0.5 m SpectraPro 2500i single monochromator equipped with a Spec400B liquid nitrogen-cooled CCD (Princeton Instruments/Acton, Trenton, NJ) was used to collect and measure the Raman scattered light. The CCD was calibrated using the emission wavelengths of a Neon lamp.

2.2.4 Principal Component Analysis of SERS Data

Principal component analysis (PCA) has recently found use as a chemometric tool capable of removing the fluorescence background from Raman spectra as well the discrimination of the Raman spectra of pathogenic bacteria and paint pigments. [36-40] PCA is a statistical technique that reduces the dimensionality of a spectral dataset. It achieves this by reducing the dataset to a linear combination of orthogonal vectors in a way such that a majority of the variance between spectra is explained by the first vector. The dot product of the first vector with any spectrum gives the value of that spectrum's first principal component. The projection of the second vector (which explains the second most variance) gives the second principal component. Due to the variability in signal from SERS (due to subtle variations in laser power and substrate uniformity), PCA often does not discriminate well based on raw SERS spectra. Patel et al have proposed the use of the magnitude of the second derivative of the spectra as input to PCA.[40] Here, we remove cosmic rays from our spectra, followed by removing the baseline by subtracting a wide (500 cm^{-1}) Hamming Window from each spectrum, followed by normalization, a spline interpolation of the data onto a 1 cm^{-1} grid, and finally perform PCA analysis on the sign (+/-) of the second derivative of the dataset.

2.2.5 Thermal and Ionic Strength Stability Assessment

All of the stability experiments were performed with both benzenethiol (a standard high scattering cross-section Raman scatterer) and RBC captured on the AgFONs. In the thermal stability tests, the AgFONs, following analyte incubation, were placed in 2 mL of nuclease-free water at various temperatures ranging from 70 °C to 95 °C for either 30

seconds or 5 minutes. The AgFONs were then rinsed with 1 mL of nuclease-free water to remove any free analyte after the thermal treatment. The SER spectra were then measured from N_2 gas-dried AgFONs using the same experimental apparatus described above.

While elevated temperature is one possible way to compromise aptamer or protein stability, variations in ionic strength may have a similar effect by weakening electrostatic or H-bonding interactions. Herein, a 1M NaCl solution was utilized as a high ionic strength solution. Similar to the thermal stability tests, the AgFONs with bound analyte were immersed in 2 mL of NaCl solution for either 30 s or 5 min. The resulting AgFONs were then rinsed with nuclease-free water and SER spectra were measured.

Possible destabilization due to pH variation was also assessed. Dilute aqueous HCl with pH of 4.96 and dilute aqueous NaOH with pH of 7.99 were prepared. Similar to the previous stability tests, AgFONs with bound analyte were immersed in 2 mL of either solution for either 30 s or 5 min. After rinsing, SER spectra were measured.

2.2.6 Computational Modeling of Aptamer on a Ag Surface

Quantum chemistry calculations were carried out for geometry optimization of the aptamer on the SERS substrate by using B3LYP.[41-43] For C, H, N, and O atoms, the basis sets used were 6-311+G(d,f).[44,45] The polarizable continuum model was used to consider the influence of water.[26,46-49] On the basis of the optimized structures, the vibrational frequencies and Raman intensity were obtained. All calculations were performed with Q-chem 4.1.0.[50]

2.3 Results and Discussion

While single-stranded DNA has been used frequently on metal surfaces as reported in the literature, the use of this ssDNA in complex matrices (such as food or body fluids) is not widely reported due to likely interference from proteins, native DNA, or possible degradation of the DNA by nucleases.[51-55] Freshly prepared AgFONs were modified with nuclease-resistant ricin B chain aptamers then incubated with 20 μg/mL RBC solution. The SERS of the AgFON before and after the introduction of RBC were collected. The RBC aptamer is 7 nm in length. Although it is hard to prove the orientation of the RBC aptamer on the surface of the AgFON, there was a great chance that we would not be able to directly detect SERS of the protein because of the exponential decay of the electromagnetic field with the distance from the noble metal. Figures 2.1, 2.3, 2.4, and 2.7 show a typical RBC aptamer and RBC captured aptamer SERS on the AgFON. Figure 2.1 (bottom) shows the SERS spectrum of the ricin B chain DNA aptamer bound to the AgFON surface. The dominant peaks in the spectrum are the ring breathing modes of adenine (735 cm^{-1} shift) and guanine (793 cm^{-1} shift).[52] The peak locations correspond well to adenine and guanine Raman spectra reported in the literature.[52] After the aptamer-functionalized AgFON was exposed to whole human blood, the aptamer SERS spectral peaks broaden and the signal-to-noise decreases. The broadening may be attributable to a hypoxanthine scattering contribution near the observed 735 cm^{-1} shift peak or non-specific adsorption of albumin to the surface of the AgFON.[27,56] The decreased signal-to-noise ratio may be caused by native blood proteins non-specifically adsorbing to the AgFON-aptamer conjugate, contributing either Raman scatter or background

fluorescence. After exposure to 1 μg/ml ricin B chain, new spectral features are apparent at 640 cm^{-1} shift and 937 cm^{-1} shift; these peaks may be due to either Raman scatter from the protein or possible conformational change of the aptamer after a binding event. The nature of the binding of aptamers to ricin have been explored in other publications, and it has been shown that these aptamers may bind to various sites on ricin.[2,3] Identifying the exact binding interaction of this aptamer is difficult and not critical to achieve the purpose of this study. In fact, the spectral changes of the aptamer-ricin B chain interaction remain consistent over many measured spectra on multiple AgFONs, making these spectral changes potential predictors of ricin B chain concentration. While this initial study proved promising, our overarching goal was to be

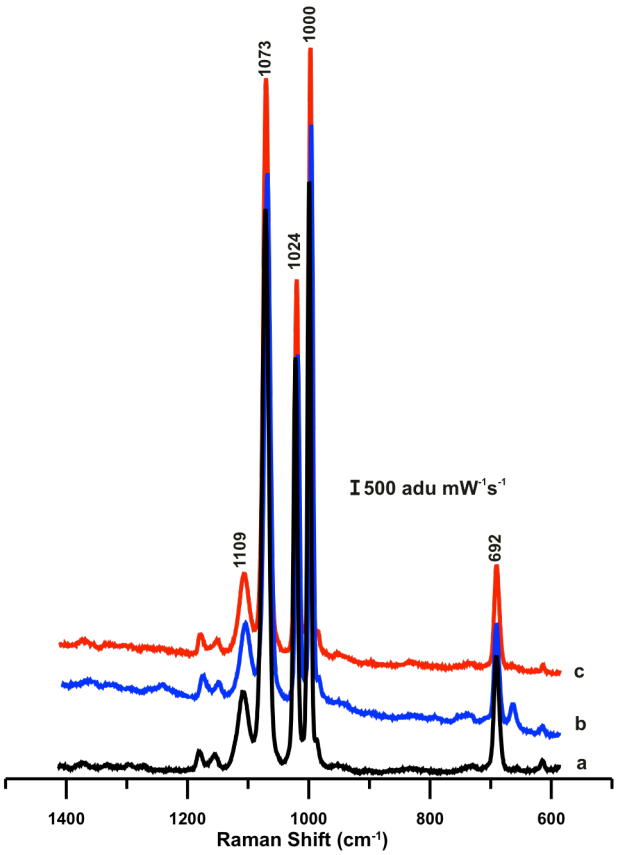

Figure 2.2. SERS of benzenethiol on a AgFON in human blood for (a) 0 days, (b) 3 days, and (c) 10 days. Each trace is an average of 7 spectra acquired from 7 randomly selected spots. Spectra are artificially offset for clarity.

able to detect ricin B chain in whole human blood over multiple days without any decline in performance of the AgFONs or the aptamer affinity agent.

To accomplish multi-day stability of the AgFONs in human whole blood, a study was initiated with a standard SERS reporter molecule (benzenethiol) rather than the more expensive aptamer/protein combination. Stability of AgFONs in whole human blood has not been previous been presented in the literature. To ensure that a SERS-active surface would be stable for an extended period of time in blood, the AgFON was functionalized with benzenethiol (1 mM in ethanol, overnight, Figure 2.2). A spectrum of the functionalized surface was acquired followed by incubation in blood. Spectra were acquired after incubation in blood for 3 and 10 days after copious rinsing with water. It should be noted that the AgFONs that were exposed to blood experienced significant degradation due to delamination of the Ag surface if care was not taken to rinse gently. After all the spectra were collected, a benezenethiol enhancement factor (EF) calculation was performed for the 0, 3, and 10 day exposure to blood, and the EFs for all 3 timepoints remain in the 10^6 range. This suggests that the roughened metal surface required for high EF SERS has not diminished after 10 day incubation in blood. While the AgFON performance itself does not diminish after many days in blood, the subsequent experiment incubating a AgFON functionalized with an aptamer was not successful. The 735 and 793 cm^{-1} shift peaks from adenine and guanine, respectively, were no longer present after 1 day. The spectral decline was likely due to nuclease degradation of the single-stranded DNA aptamer. Following literature precedent, we

considered various modifications to the DNA backbone and to the DNA bases to prevent binding of nuclease and therefore, increase the lifetime of the DNA in biological solutions.[57-59] The modification that was chosen was a phosphorothioate bond in the DNA backbone to decrease recognition of the nuclease binding sites while maintaining

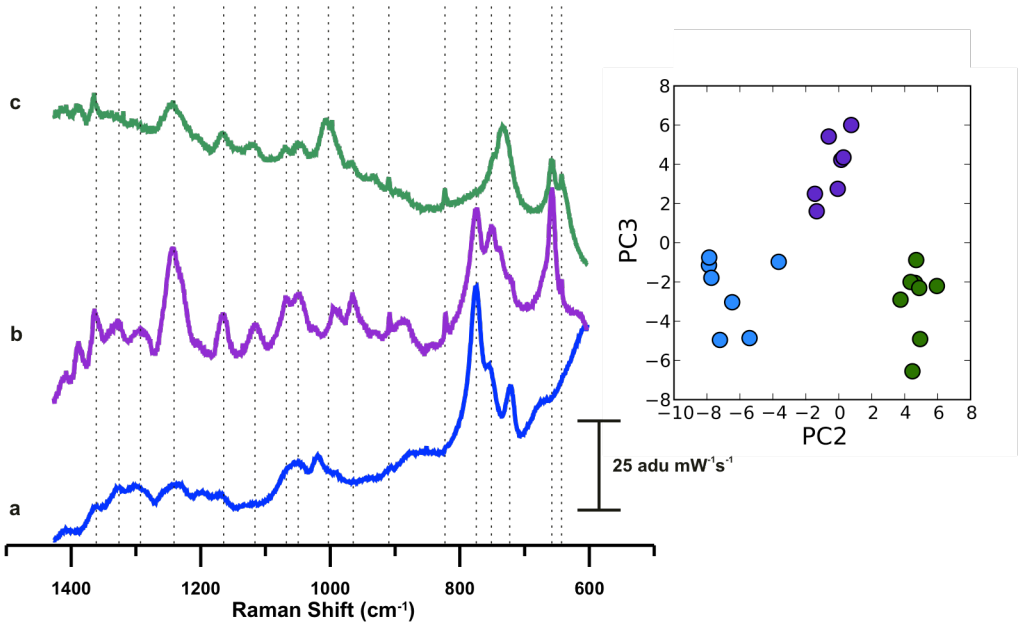

Figure 2.3. SERS on a AgFON of (a) nuclease-resistant ricin B chain aptamer (b) nuclease-resistant ricin B chain aptamer in whole-human blood for 3 days (c) nuclease-resistant ricin B chain aptamer after exposure to ricin B chain in blood. Each trace is an average of 7 spectra acquired from 7 randomly selected spots. Spectra are artificially offset for clarity. On the right, PCA plot shows grouping of the nuclease-resistant aptamer (blue dots), nuclease-resistant aptamer in blood (purple dots), and nuclease-resistant aptamer in blood after exposure to ricin B chain (green dots).

the aptamer sequence. [58,60] The aptamer-ricin B chain binding experiments were repeated with the nuclease-resistant aptamer after substrate exposure to whole human blood for either 3 or 10 days (Figure 2.3 and 2.4). Good signal-to-noise spectra were obtained from these experiments; however, the modifications to the DNA backbone also increased the

spectral complexity. Two strategies were employed to evaluate the sensor performance despite the spectral complexity. The first was computational modeling of the DNA SERS spectrum expected on a Ag plasmonic surface so that particular Raman bands could be attributed directly to the aptamer affinity agent. The second was principle component analysis (PCA) to help differentiate small changes in the spectral patterns in these complex environments.

The computational model of the aptamer Raman spectrum assumes that the aptamer is perpendicular to the surface.[22,23] In addition, based on the well-known distance dependence of SERS enhancement, the first few DNA bases, adjacent to the thiol, were given priority when considering contributions to the spectrum.[61-64] The bases after the first 7 were treated in one of two ways: either (1) the bases were all considered to be the same distance from the surface or (2) the bases were all considered to be too far away from the surface to contribute to the spectrum. While the aptamer does contain a hairpin loop and bulge at C15-G25 and G10-C29, respectively, these assumptions are not influenced based on the distance between both the hairpin and bulge from the Ag surface.[22] The intensity of the computationally derived aptamer spectrum can be expressed from Eq 1 and Eq 2 found in the supporting information, and the results of the aptamer spectral modeling can be seen in Figure S3 in the supporting information. The experimentally and computationally derived spectra are in good agreement (Figure 2.4) with the major contributions in the spectra resulting from adenine and guanine scattering. As can be seen, the spectrum of the nuclease-resistant aptamer still exhibits peaks from

adenine and guanine, although differing in intensity compared to the natural aptamer backbone. Due to the complexity of the spectrum when incubated in blood, PCA was utilized to evaluate the effectiveness of our detection method. In Figure 2.3, the principal component analysis shows the nuclease-resistant aptamer spectra clustering together, the

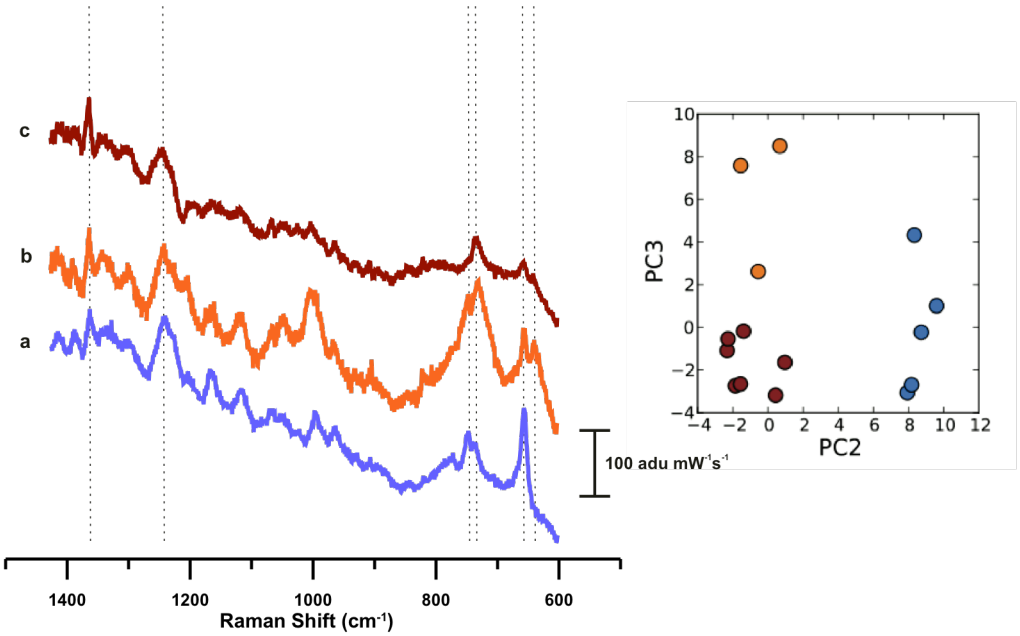

Figure 2.4. SERS on a AgFON of (a) nuclease-resistant ricin B chain aptamer in blood for 10 days (b) nuclease-resistant ricin B chain aptamer in whole-human blood for 10 days followed by ricin B chain exposure (c) AgFON in human whole blood for 10 days. Spectra are artificially offset for clarity. On the right, PCA plot shows grouping of the nuclease-resistant aptamer (blue dots), nuclease-resistant aptamer in blood (orange dots), and nuclease-resistant aptamer in blood after exposure to ricin B chain (red dots).

nuclease-resistant aptamer spectra captured after exposure to blood clustering together, and the nuclease-resistant aptamer spectra captured after exposure to both blood and ricin B chain clustering together. More importantly, there is no overlap between different spectral classes in the principle component analysis. In future experiments, this may be applied to a training data set to identify the presence of ricin B chain among unknown

protein analytes. To evaluate specificity of the aptamer-modified AgFON for ricin B chain, control experiments with BSA (bovine serum albumin) were conducted; the prinicipal components due to the BSA-exposed aptamer-functionalized substrates clustered separately from the ricin B chain exposure experiments. BSA was chosen to evaluate specificity because of the relatively high concentration of albumin in blood (3.5-5.0 g/dL) and its similarity in size to intact ricin.[13,65] Figure 4 shows the spectra recorded for the aptamer after exposure to blood for 10 days (bottom) and the aptamer after exposure to blood and ricin B chain for 10 days (middle). As can be seen in the spectra, the peaks that are normally very prominent for the aptamer after shorter blood exposure times are now shoulders of peaks due to blood components. The aptamer peaks are still present in the bottom two traces, however in the top control trace with just blood, there are no aptamer bands while the shoulders that appear in the bottom two spectra are not present in the control spectrum. While the typical experimental protocol was to measure at 7 different locations on each AgFON, the silver surface partially delaminated during these long-term blood exposure experiments, leaving only a few active areas on the substrate. During the ricin B chain exposure, the AgFON further delaminated, leaving only 3 locations to be measured. However, the three different classes of experiments cluster separately following PCA analysis, indicating that, of the surfaces that remained intact, it was still possible to distinguish between the nuclease-resistant aptamer in blood and the nuclease-resistant aptamer exposed to ricin B chain. Future work in substrate design will focus on increasing the mechanical robustness of these

plasmonic surfaces while maintaining the enhancement factor and the ability to modify the structure with desired affinity agents.

2.3.1 Reversibility

Ideally, the interaction between the aptamer and target analyte would be reversible so that the sensing platform could be reused. Ricin is known to be highly resistant to both heat and pH, [66-68] and there are limited publications on the inactivation of ricin.[67-69] In attempt to achieve reversibility, the interaction between the aptamer and RBC,

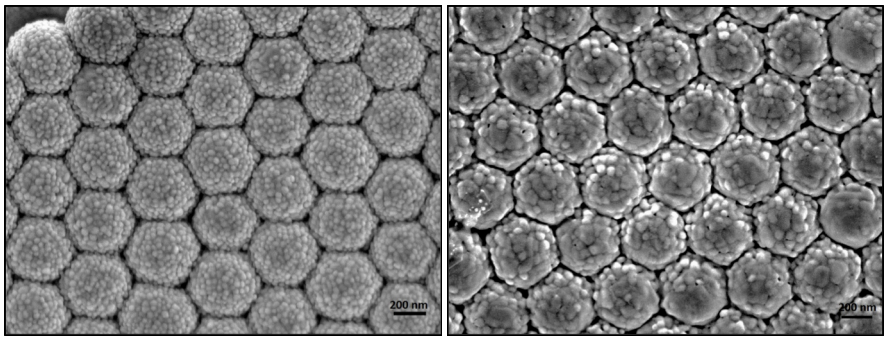

Figure 2.5. SEM images of AgFON before (left) and after (right) thermal treatment for 5 minutes at 95 C°. Scale bars indicate 200 nm.

association was studied under various conditions, including varied temperature, pH and ionic strength. SERS signal responses to all of these conditions were identical. For brevity, only the influence of elevated temperature on the sensor performance is discussed in detail.

Prior to direct study of the stability of the association between the protein and the aptamer, it was important to first characterize the physical conditions that might induce disassociation of the aptamer from the AgFON surface or cause damage to the AgFON

itself. Again, benzenethiol was employed as a model molecule to study the stability of the thiolate-silver interaction as well as the stability of the AgFONs themselves. While there is much precedent work exploring the thiolate-Au dissociation, there are no systematic studies of the stability of thiol-silver interactions.[67,68,70]

Herdt *et al* reported degradation of DNA-Au conjugation at 70 °C within hours.[54,69]Therefore, to study the stability of S-Ag interaction at elevated temperature, the temperature range considered herein is 70-95 °C, where 95 °C is the temperature typically used to fully unfold the aptamer (ricin B chain aptamer is known to maintain its conformation in the temperature range of 4-63 °C). [22] As shown in Figure 2.5, the Raman bands at 1073, 1024, 1001, and 695 cm^{-1} shift are attributable to benzenethiol while the 1349 cm^{-1} shift peak is due to residual ethanol. As one might predict, higher temperature accelerated the dissociation of the S-Ag conjugation. Taking the intensity of peak 1073 cm^{-1} shift as an example (other benzenethiol peaks followed the same trend), the peak intensity decreased with increasing temperature. After the thermal treatment at 95 °C, a significant decrease of the SERS signal was revealed by two-tailed t-test (p value after 30 s treatment is 0.0006 and after 5 min treatment is 6×10^{-6}). In addition, incubation at 70 °C for 30 s did not impact the SERS of benzenethiol (p value = 0.93) while the SERS signal variance at 70 °C for the 5 minute incubation was significant (p value = 0.01), indicating that the longer incubation time enhanced the dissociation of benzenethiol from AgFONs. While these signal intensity losses may, in fact, be due to dissociation of the thiolate-Ag interaction, there are other potential contributing factors to keep in mind.

First, silver is a highly oxidizable metal that can also undergo annealing processes, known to be even more vulnerable in nanoscale than bulk form.[71] Second, Raman scattering efficiency is highly dependent of the molecular orientation of the scatterer on the SERS substrate; it is possible that the temperature elevation, even for short time periods, causes a reorientation of the benzenethiol, rendering it a less efficient scatterer. Thus, we assume that all three factors, dissociation of thiolate-Ag conjugate, damage to the AgFON surface, and reorientation of molecular species contribute to the SERS signal decline. The post-thermal treatment AgFONs were reincubated in the benzenethiol stock solution and then analyzed by SERS again. The results showed that the AgFON treated at a lower temperature and for a shorter time period recovered the initial SERS benzenethiol signals following reincubation. In contrast, the AgFONs that were treated at the highest temperature did not recover the benzenethiol SERS spectra following reincubation. This experiment demonstrates that the SERS signal decay at high temperature includes some contribution of permanent damage to the AgFON nanostructure. Figure 2.6 shows the SEM images of the AgFONs before and after the thermal treatment at 95 °C. The sharp features on the original AgFON anneal, decreasing the roughness of the surface and leading to a lower SERS enhancement. The visible black spots on the SEM image in the post-thermal treatment AgFON indicate areas devoid of Ag coverage. Based on these experiments, it is clear that high temperatures and long temperature excursions times are not appropriate condition changes to induce reversibility in this ricin B chain sensing system.

Thermal treatments were performed on the RBC-exposed aptamer-functionalized AgFONs. The SERS signal of aptamer at 731 cm^{-1} shift decreased 31.6% after thermal treatment at 80 C°, significantly (p value = 0.03) more than the benzenethiol signal decline under the same conditions (SERS signal of benzenethiol at 1071 cm^{-1} decreased 13.5% after thermal treatment at 80 C°), indicating that the conformational change of ricin B chain aptamer caused by the thermal treatment contributes to the decline of the SERS signal. Even though there is a clear decline in the SERS signal intensity following thermal treatment, the 1274 cm^{-1} shift peak that indicates the presence of ricin B chain was still measurable (Figure 2.7). Slight modifications of the detailed thermal treatment have been performed, including heating under N_2 gas and heating at a lower and physiological temperature for an extended time period (37 °C for 24 h). In all these variations, the 1274 cm^{-1} shift peak remains in the SERS spectrum.

Ionic strength and pH are known to influence the conformation of DNA, thus, variation in these conditions present another potential avenue for intentionally destabilizing the aptamer/target interaction. SERS spectra of the post-treatment benzenethiol-functionalized AgFONs revealed no obvious changes when compared to the pre-treatment conditions (Figure S1 in supporting information), indicating that substrate and the S-Ag conjugate are stable in a 1 M NaCl solution and within the pH range from 5-8. Under these conditions, a decrease in the aptamer-RBC conjugate SERS signal would likely due to the dissociation of RBC from the aptamer. However, similar to thermal treatment, the association of aptamer and RBC was intact during the treatment

according to the SERS spectra. In summary, 95 °C, 1 M NaCl and pH 5-8 were not able to induce the dissociation of RBC from the capture aptamer without also irreversibly damaging the plasmonic substrate.

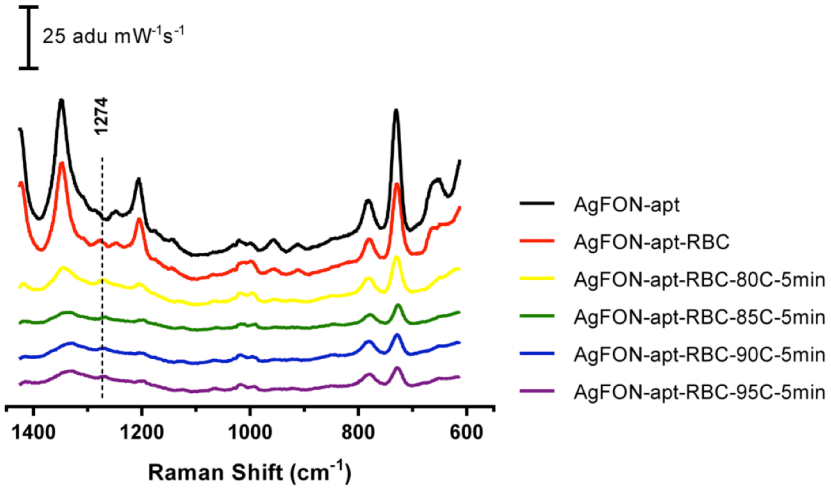

Figure 2.6. SERS of aptamer and aptamer-ricin B chain conjugates on AgFONs before and after thermal treatments.

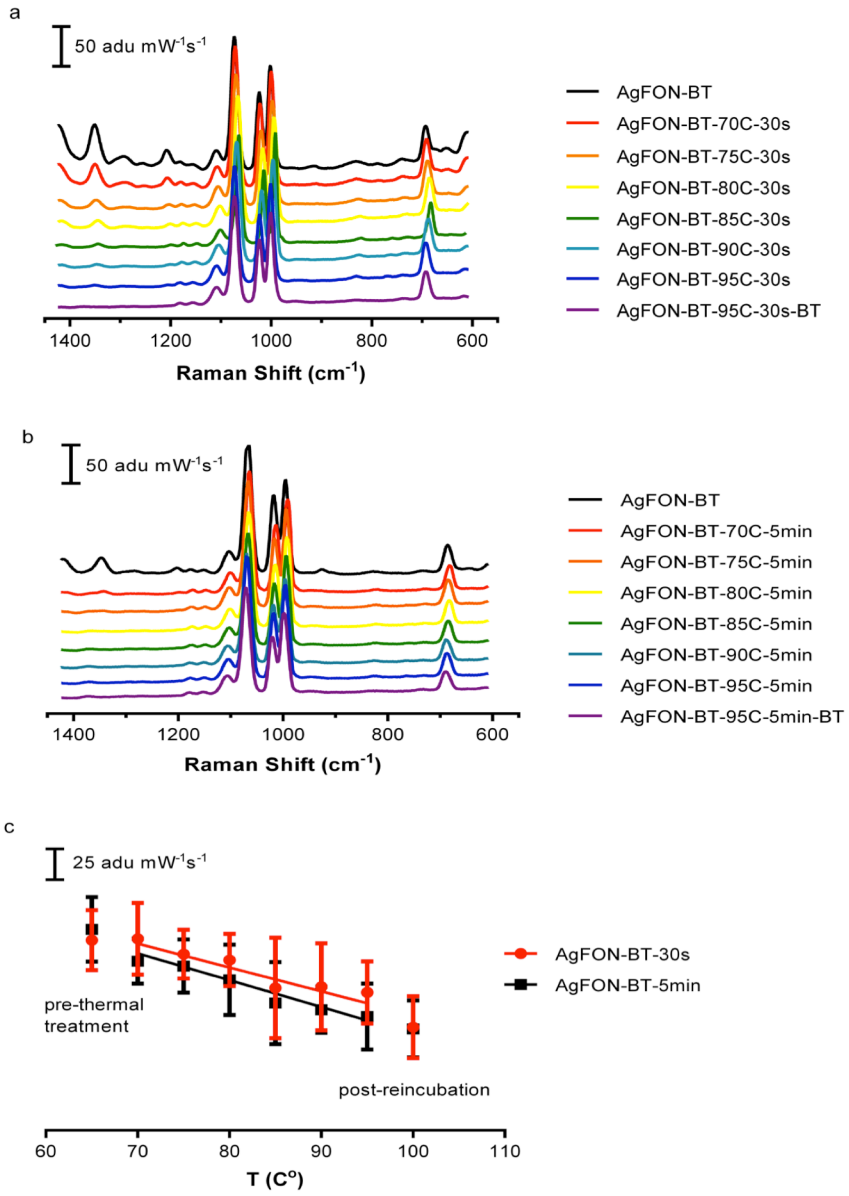

Figure 2.7. SERS of benzenethiol on AgFONs treated at elevated temperature for a) 30 s or b) 5 min. The spectra are vertically off-set for clarity, λ_{ex} = 633 nm. Each trace is the average of 10 randomly chosen spots on the AgFON *Need to include parallel details to other captions about number of averaged spectra, etc* c) shows benzenethiol SERS intensity at 1071 cm^{-1} shift decreasing with increasing temperature, the far left spots are the intensities before the thermal treatments, the far right spots are the intensities after the AgFONs reincubated with benzenethiol stock solution (the purple spectra in both (a) and (b).

2.4 Conclusions

The detection of ricin B chain in whole human blood was performed on aptamer-functionalized AgFONs *via* SERS. AgFONs were shown to be stable in whole blood for 10 days. A modification to the aptamer DNA backbone was needed to ensure stability of the aptamer for more than 1 day in whole human blood. While many attempts were made achieve reversible interaction of the aptamer and ricin B chain, the interaction persisted after substrate exposure to low pH, temperature elevation, and high ionic strength; more work is required to achieve reversibility, perhaps using a lower affinity aptamer sequence. Principle component analysis of SER spectra reveal ricin B chain detection after even 10 days in human whole blood at a concentration that would be fatal.

Chapter 3. Microfluidic-SERS Devices for One Shot Limit-of-Detection

*Adapted from:
Microfluidic-SERS devices for one-shot limit-of-detection, Campos, A.R., Kim, D., Datt, A., Gao, Z., Rycenga, M., Burrows, N., Greeneltch, N.G., Mirkin, C.A., Murphy, C.J., Van Duyne, R.P., Haynes, C.L., *Analyst*, 139, 3227–3234 (2014).

3.1 Introduction

Microfluidics is an often-used technique for sample manipulation in bioanalytical and biomedical sciences because the devices are largely biocompatible, require small (viz., nanoliter) sample volumes, create small volumes of biohazard waste, and enable faster analyses and higher throughput than many bench-top techniques. These advantages make microfluidics especially promising for biological applications and bioanalytical sensor developments, particularly when interrogated with optical detection schemes. Among the various optical detection methods that can be used in conjunction with microfluidic platforms, Raman spectroscopy is particularly interesting for bioanalytical applications because it yields an intrinsic vibrational fingerprint for detected analytes, and its performance is not compromised by water interference in aqueous samples. Normal Raman spectroscopy has inherently small scattering cross-sections, yielding poor analyte sensitivities; however, surface-enhanced Raman scattering (SERS) provides opportunities to enhance detection sensitivity significantly.[1-4] This enhancement is attributable to the large molecular dipole moment induced when a Raman-active molecule experiences the electromagnetic fields generated at the surface of nanostructured plasmonic noble metals. Practically speaking, the SERS limit of detection can reach the single-molecule detection realm, but nanomolar and picomolar analyte concentration detection is routinely observed

with high quality plasmonic substrates.[5-9] Accordingly, SERS has been employed in microfluidic platforms to identify chemical moieties in bioanalyte systems including cells, viruses, bacteria, organelles, sub-organelles, DNA, proteins, drugs, and cellular communication mediators.[8-13]

Colloidal noble metal nanoparticles are the most commonly used SERS-active substrates within microfluidic devices.[1,14-18] In general, the SERS-active nanoparticles are injected through a microfluidic channel where they encounter analyte species at a specified physical location within the device. The primary challenge with this type of approaches is that it is difficult to achieve large and consistent signal enhancement[45-49] without controlled colloidal nanoparticle aggregation.[5,18,50] It has been reported that the best SERS signal enhancement for gold nanoparticles can be achieved when nanoparticles are in contact, or at least separated by not more than 1-2 nm;[5,18,50] however, the challenge of controlling nanoparticle aggregation presents persistent experimental roadblocks related to stability, sensitivity, and reproducibility of the obtained signal both in and out of microfluidic devices. Previous work also reports unexpected loss of nanoparticles or defects in their aggregation/arrangement due to nanoparticle interactions with channel surfaces or the flow profile.[19] To avoid these difficulties, there have been several reported systems where a SERS-active substrate is incorporated into a microfluidic device.[20-21] In these reports, SERS-active substrates were largely fabricated either on glass or silicon using high-end lithography techniques, aligned, and bound to a layer containing the microfluidic channel geometries. These finely-tuned SERS-active substrates, such as

nanoholes or nanogaps,[22-27] have very high signal enhancements compared to simple colloidal nanoparticles; however, fabrication can be prohibitively expensive and requires access to specialized instrumentation for time- and labor-intensive fabrication protocols.

Herein, we present two types of proof-of-concept microfluidic-SERS sensing platforms with potential to address the aforementioned challenges: a microfluidic gold film-over-nanospheres (AuFON) platform and a flexible SERS sensor platform with nanoparticles incorporated directly into the microfluidic polymer layer. Gold was chosen over silver as the plasmonic material, despite its lower signal enhancement compared to silver, because of its stability against dissolution and oxidation, lower toxicity, and ease of surface functionalization for future bioanalytical applications.[10-11]

The microfluidic AuFON platform, as the name implies, employs a AuFON as the plasmonic component. Multiple groups have previously demonstrated, using silver film-over-nanospheres (AgFON), that noble metal FON substrates can provide strong, reproducible SERS enhancement factors.[2,22] Similar capabilities have been reported for AuFONs as well.[23-29] The most appealing aspect of FONs as SERS substrates is that, despite relatively simple and inexpensive fabrication techniques, they exhibit extraordinary signal enhancements ($10^6 \sim 10^8$) with uniform and reproducible analyte response over square centimeters of substrate areas. As such, the noble metal FONs have become the gold standard for SERS substrates. In addition to the aforementioned advantages of AuFONs over AgFONs, gold also provides better compatibility than silver with the microfabrication techniques used to combine SERS-active substrates with

polydimethylsiloxane (PDMS)-based microfluidic platforms.

For the flexible SERS sensor platform, gold nanorods (AuNRs)[37] and gold nanocubes (AuNCs)[38-39] are used as nanoparticle SERS substrates. These nanoparticles are directly dispersed into the PDMS device before curing and enable SERS detection of analytes flowing through the device. The relatively simple fabrication of this device adapts to any desired channel geometry, retains the optical transparency and flexibility of the device, and employs a relatively small number of nanoparticles. To our knowledge, there are only a few reported research efforts where nanoparticles were embedded directly into a microfluidic device.[20,31] In those studies, gold nanocomposites were created by vapor deposition or in situ synthesis onto microfluidic channels or by stamping nanocomposites onto the side of a microfluidic device. Despite the potential benefits of these methods, the in situ synthesis approach and vapor deposition frequently consume an unnecessary amount of gold and complicate further device fabrication steps. In addition, the potential of those approaches to achieve the optimally enhancing nanoparticle aggregates is dubious.

Employing PDMS-based microfluidics herein enables the realization of a portable, durable SERS sensing platform with added analytical strengths. In the proof-of-concept microfluidic-SERS sensor platforms presented herein, microfluidic channels are designed to enable easy limit-of-detection (LOD) or limit-of-quantification (LOQ) studies. The fundamental principle of the device is based on previously reported microfluidic devices, capable of creating chemical gradients,[32] with a slight modification to achieve

simultaneous detection of different concentrations of an analyte. Another advantage of the PDMS-based SERS sensor is that PDMS provides strong Raman-active bands in a 490-700 cm^{-1} shift region as an internal standard. As our results show, the presented microfluidic-SERS platforms are capable of quantitative, single experiment LOD/LOQ assessment, and demonstrate their potential for multiplexed high-throughput analysis. Further development of these proof-of-concept platforms will facilitate the development of several diagnostic devices for early disease detection and continuous monitoring of patients.

3.2 Methods and Experimental Setup

3.2.1 AuFON fabrication After silicon immersion in a base bath with 10:1:1 water:ammonium hydroxide (30%):hydrogen peroxide (30%) for an hour, 13 μL of 600-nm-diameter silica nanospheres (Bangs Laboratories, Fishers, IN) were drop cast onto the clean silicon wafer. The silica nanospheres were distributed on the silicon wafer until there were no visible mixing lines, and then the wafer was allowed to air dry. After nanosphere self-assembly and drying, 200 nm of Au (99.999 % Au Kurt J Lesker, Clairton, PA) was deposited onto the nanosphere template under vacuum, as measured by a quartz crystal microbalance (Denton Vacuum, Moorestown, NJ). The localized surface plasmon resonance (LSPR) of the substrate was measured to be λ_{max}= 790 nm using a fiber optic probe (Ocean Optics, Dunedin, Florida) with a flat gold film as the reflective standard, and the AuFONs were stored in a closed petri dish until use.

3.2.2 Au concave nanocube (AuNC) synthesis Gold concave nanocubes (AuNCs, 53 ± 10 nm in edge length (n=30), 4 nM as synthesized) were fabricated in a synthesis adapted from Rycenga et al.[38-39] In brief, Au seeds were prepared by quickly injecting 0.60 mL of ice-cold, freshly prepared $NaBH_4$ (10 mM) into a rapidly stirring solution containing 0.25 mL of $HAuCl_4$ (10 mM) and 10.0 mL of cetyltrimethylammonium chloride (CTAC, 100 mM). The seed solution was stirred for 1 minute and then left undisturbed for 2 hours. A growth solution was prepared by consecutively adding 0.50 mL of $HAuCl_4$ (10 mM), 100 μL of $AgNO_3$ (10 mM), 0.20 mL of HCl (1.0 M), then 0.10 mL of ascorbic acid (100 mM) into 10.0 mL of 0.1 M CTAC. The seed particles were serially diluted in 100 mM CTAC to generate a solution 1/1000 the concentration of the original seed solution. Particle growth was initiated by adding 0.1 mL of the diluted seeds to the growth solution. The reaction was swirled immediately after the addition of the seeds and then left undisturbed on the bench top overnight. The in-solution LSPR λ_{max} was 618 nm.

3.2.3 Au nanorod (AuNR) synthesis Gold nanorods (AuNRs, 48 ± 11 x 13 ± 2 nm (n=30), 5 nM after washing) were prepared on a two-liter scale in a millifluidic flow reactor following previously published procedures[37] based on a seeded growth approach.[40-42] Briefly summarized, two solutions were prepared, labeled “growth” and “seed”. For the growth solution, 98.55 mL of HAuCl4 (0.01M), 12.0 - 18.3 mL of

AgNO3 (0.01M), and 10.84 mL of ascorbic acid (0.1 M) were added to 0.1 M CTAB (cetyltrimethylammonium bromide) with a final volume of 1 L. For the seed solution, 2.365 mL of gold nanoparticle seeds prepared following previously established methods4 was added to CTAB (0.1M) with a final volume of 1 L. Then, these solutions were combined via peristaltic pump (Cole-Palmer Masterflex L/S) in a millifluidic reactor (Tygon polyvinyl tubing, i.d. = 2.79 mm) with: 1) polyethylene Y-mixer and joints, 2) a flow rate of approximately 8.0 mL/min, and 3) a residence time of 20 minutes. Gold nanorod suspensions were eluted from the reactor into an aqua regia-cleaned two-liter Erlenmeyer flask with magnetic

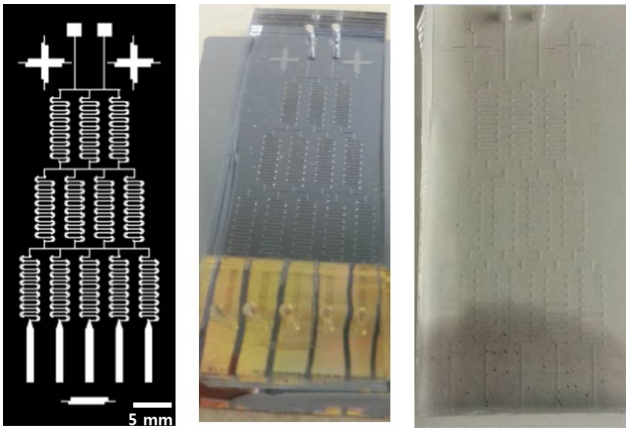

Figure 3.1. Device design (left) and photographs of microfluidic-AuFON (middle) and flexible SERS sensor (right).

stirring and held for 2–3 hours prior to purification, concentration, and characterization. Gold nanorods were concentrated and purified by washing with centrifugation. The 2 liters of suspension was divided into 50-mL centrifuge tubes and centrifuged at 11,000×g for 15 minutes. The supernatant was syphoned off, and the pellets were redispersed in 1

mL of nanopure water, each, and combined into eight centrifuge tubes filled to 40 mL with nanopure water. These were then centrifuged at 5,000×g for 25 minutes, syphoned, and dispersed in nanopure water. This process was repeated twice more with CTAB (800 μM) for dispersing the pellet. The suspension was then centrifuged one last time at 5,000×g for 25 minutes with the pellets combined into one centrifuge tube and dispersed in CTAB (800 μM). The resulting suspension was then characterized using UV-Vis-NIR spectroscopy, DLS, PALS, and a bromide ion-selective electrode. The in-solution LSPR λmax values were 526 nm and 760 nm, and the resulting nanorod concentration was 5 nM.

3.2.4 Nanoparticle characterization These colloidal nanoparticles were used in the synthesis of flexible SERS sensor platforms—detailed below—and likely retain some CTAB/CTAC moieties on their surface.[25,26] Characterization of these nanoparticles was performed by transmission electron microscopy (TEM, FEI Tecnai T12 electron microscope operating at 120 kV) and UV-vis extinction (Ocean Optics, Dunedin, Florida).

3.2.5 Microfluidic-AuFON device fabrication Standard photolithography procedures described in a previous paper were followed for device fabrication.[33] Briefly, the device design (Figure 1), printed onto a transparent film (CAD/Art Services Inc., Bandon, OR), was transferred to a blank chrome mask plate (Nanofilms, Westlake Village, CA). Then, using the mask, the design was transferred to a SU-8 photoresist

layer (Microchem, Newton, MA) on a silicon wafer. Then, de-gassed 10:1 weight ratio of Sylgard 184 resin and curing agent mixture (Ellsworth Adhesives, Germantown, WI) was cast onto the master and cured at 65 ℃ overnight to complete the PDMS channel layer. Channel dimensions were 100 μm wide and 100 μm high. For practical purposes, the terminal channels where measurements were performed had 1000 μm width. Bonding of the PDMS layer to AuFON was done via oxygen plasma treatment at 100 W for 10 seconds after inlet and outlets were punched. All fabrication steps were performed in the Minnesota Nano Center (MNC) at the University of Minnesota.

3.2.6 Flexible microfluidic-SERS sensor device fabrication Flexible SERS sensors were fabricated using the same SU-8 mold used for the microfluidic-AuFON devices. Nanoparticle solutions (1 mL of 5 nM AuNRs or 4 nM AuNCs in water) were centrifuged at 10,000×g for 10 minutes, and the supernatants were removed using a micropipette. Then, the nanoparticles were re-suspended into 100 μL of the curing agent component of Sylgard 184, mixed with 900 μL Sylgard 184 resin, de-gassed, and finally poured onto the terminal channel array area of the SU-8 mold. After 30 minutes of curing on a 65 ℃ hot plate, 10:1 resin:curing agent mixture of Sylgard 184 was poured onto the mold, covering the entire device design, and cured overnight. Then, the device layer was peeled, cut, and punched for inlets and outlets. At this stage in device fabrication, SERS measurement on the microfluidic platform was possible but often not successful, likely because a large majority of the nanoparticles were completely incased in PDMS (i.e. not

exposed to the in-channel stream of analyte). To enhance nanoparticle/analyte interaction, the PDMS layer was dry etched via reactive ion etching (75% CF_4 and 25% O_2, 100W, one hour) and then this layer was bound to another clean and flat PDMS layer via oxygen plasma treatment.

3.2.7 Analyte Solution preparation 10 mM trans-1,2-bis(4-pyridyl)ethylene (BPE, Sigma Aldrich) was prepared in ethanol, followed by dilution to 10 nM with MilliQ water (Millipore, Billerica, MA). 50 μM rhodamine 6G (R6G, Sigma-Aldrich, St. Louis, MO) stock solution was also prepared in ethanol, and the final 1 μM R6G solution was prepared by diluting the stock with MilliQ water.

3.2.8 Fluorescence microscopy An inverted microscope with a 20x objective (Nikon, Melville, NY) and a CCD camera (QuantEM, Photometrics, Tucson, AZ) was used to collect on-chip fluorescence images in three replicates. Metamorph Ver. 7.7.5 was used as the imaging software. Images of each channel were acquired with 10 ms exposure times. Once collected, the maximum fluorescence intensity, in arbitrary unit (AU_{max}), in the region was recorded from each channel.

3.2.9 SERS measurements The prepared microfluidic-AuFON device substrate was attached to the xyz stage (Thor Labs, Newton, NJ), and SERS spectra were measured with a SnRI ORS system (λex=785 nm, Snowy Range Instruments, Laramie, WY). The

LSPR lmax values the SERS substrates were 790 nm for the AuFON, 760 nm for the embedded AuNRs, and 618 nm for the embedded AuNCs; thus, the SnRI ORS system excitation wavelength is most appropriate for the AuFON and AuNR substrates. An xyz micromanipulator stage was used to achieve fine control over the measurement spot locations and focus throughout the experiment. Measurements were made across all five channels at five different positions within each channel. An averaged spectrum was collected (three replicates for 1 second each) at an incident laser power of 3 mW for each position. SERS

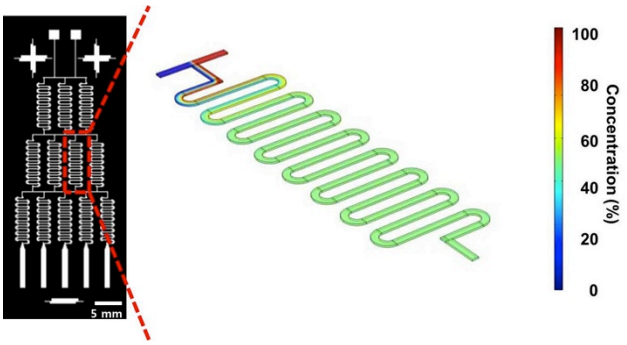

Figure 3.2. Microfluidic platform design and COMSOL modeling for the mixing process (diffusion coefficient of 1.0 x 10^{-5} cm^2/s and flow rate of 10 µL/min).

measurements were conducted after 10 minutes flow through the device to ensure that the gold surface was equilibrated to the solution-phase analyte concentration so that the measurement was not biased with time.

To be noted, a sharp Raman peak was frequently obtained at ~520 cm^{-1} shift in the flexible SERS sensors. In the literature, several studies have observed this peak during SERS measurements in a PDMS device; the most convincing identity of this peak is

mono- or poly-crystalline silicon.[35,36] For SERS measurements in the flexible SERS sensor, a silicon wafer was always present underneath the flexible SERS devices during measurements to better visualize the channels, which may have led to the sharp Raman peak. Another possibility is that the reactive ion etching chamber is frequently used for silicon etching, and a silicon wafer was present in the chamber during etching of the flexible SERS PDMS layer; as such, the Au nanoparticles may have been exposed to silicon during the etching process. This 520 cm^{-1} shift band was not considered when assessing the performance of these devices.

3.3 Results and Discussion

3.3.1 Device operation/simulation The microfluidic device used herein was designed to establish a concentration gradient of injected solutions so that a range of discrete concentrations are presented to each detection element.[32] Once solution 1 and 2 are injected through inlets 1 and 2, respectively, the solutions repeatedly mix and split while passing through serpentine channels (denoted as mixing channels, Figure 3.2). The original millifluidic design combines all branches at the end so that a linear concentration gradient of the solution is established in one wide channel downstream of the mixing channels,[20] but herein, all outcome branches are separated so that the analyte coming out of each channel can be individually monitored. To achieve the desired results, complete mixing is required within each mixing channel. Computational fluid dynamics (CFD) calculations assuming a 3-dimensional single laminar flow model were performed using

COMSOL Multiphysics 4.3 to assess the mixing process for the given channel geometry (Figure 3.2). Channel dimensions were modeled as fabricated except that the channel height was set as 50 μm with symmetry to shorten computing time. As such, in this simulation, incompressible flow and the no slip boundary condition were used with user-defined diffusion coefficients, ranging from 0.5 x 10^{-5} cm^2/s to 1.0 x 10^{-5} cm^2/s, and flow rates

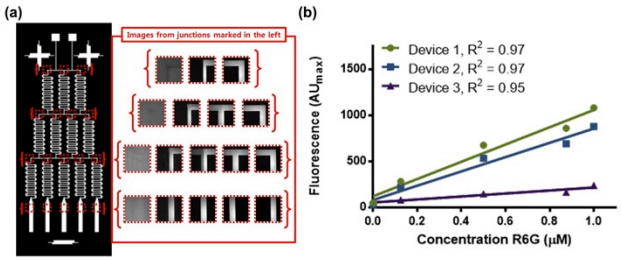

Figure 3.3. (a) Complete microfluidic device without SERS substrate - water into the left inlet and 1 μM R6G solution into the right inlet to demonstrate the device design and functionality. Red boxes on the device design denote the locations of the fluorescence images from the working device. (b) Representative fluorescence response analysis.

of 5, 10, 20, and 30 μL/minute. Figure 3.2 shows the microfluidic device design with a representative simulation data plot. The simulation results confirm that, in all given conditions, each mixing channel achieves complete mixing (i.e., the device operates as desired). In the experiments described below, a flow rate 10 μL/minute was used.

3.3.2 Fluorescence imaging Before performing SERS measurements, device performance was experimentally evaluated by fluorescence imaging. Figure 3.3a shows the actual device bound to a clean glass substrate and fluorescence images from each

location marked using red boxes. By visual inspection, the achieved fluorescence images showed the expected behavior, and thus, the obtained data were further analyzed quantitatively. Figure 3.3b summarizes fluorescence intensity data (maximum fluorescence intensity in arbitrary unit, AU_{max}) for R6G introduced into 3 representative devices. In total, seven devices were tested for linearity of fluorescence response from the channel arrays, and the average R^2 value was 0.94 ± 0.02 (mean ± standard error of mean). This linear response was further evaluated by obtaining measurements from 3 vertical locations in each of the five terminal channels of a device (Figure S1). For this assessment, fluorescence intensity from the array of five channels was obtained from 3 fixed y-axis positions of the stage, and all collected data demonstrated linear response from the array of channels with R^2 values better than 0.90.

3.3.3 SERS assessment of the microfluidic-AuFON device Having achieved the desired performance of the microfluidic portion of our sensing platform, we next evaluated SERS performance of our microfluidic-AuFON platform. As PDMS does not bind well to gold surfaces, the AuFON was intentionally removed at preferred device binding locations to expose the silicon surface, which does bind to PDMS. Then, oxygen plasma treatment was used to induce permanent bonding between the PDMS device and AuFON substrate. Once assembled as shown in Figure 3.1, a BPE solution was introduced into the device following the same procedure used for fluorescence imaging: media without BPE into one inlet and BPE solution into the other inlet using a 10

μL/minute flow rate. We started with a high concentration of BPE (10 mM). BPE is known to adsorb onto noble-metal surfaces,[43-45] so the channels were rinsed with water before SERS measurements. The LSPR λ_{max} of the in-device AuFON was 790 nm, a good plasmonic match for the SERS

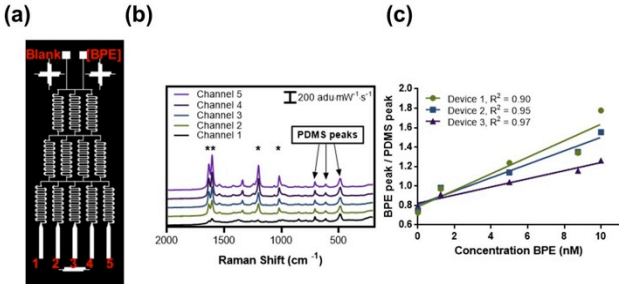

Figure 3.4. (a) Device design, (b) representative SERS spectra (BPE-characteristic bands marked with *) from the microfluidic-AuFON, and (c) SERS response analysis from 3 separate devices/substrates. Solvent vs. 10 nM BPE solution (BPE peak used for analysis: 1640 cm^{-1}) was used as the analyte system.

excitation wavelength of 785 nm. The SERS spectrum of BPE has characteristic bands at 1021, 1210, 1610, and 1640 cm^{-1} shift,[22] and all of these bands were observed in the measurement terminals (data not shown). All attempts confirmed that the characteristic BPE bands were a result of SERS, rather than normal Raman from the solution, because the SERS bands were still present after rinsing with water in the channels or after the device was allowed to dry (data not shown).

As such, a much lower concentration of BPE (10 nM) was used to further evaluate the utility of the microfluidic-AuFON platform. From the left to the right in Figure 3.4a, the expected concentrations from each outlet channel are 0, 1.25, 5, 8.75, and 10 nM. All BPE-characteristic SERS bands are obtained from individual channels with varying

intensities (Figure 3.4b) and a complete calibration curve with the assessment of LOD/LOQ was successfully obtained (Figure 3.4c). It should be noted that we observed device-to-device variations, based on differences in AuFON quality. However, irrespective of the overall quality of the AuFON, the device showed linear response to linear concentration gradients of BPE. Even though measuring BPE concentrations lower than 1 nM was not successful every time, the difference between the 0 nM channel and the 1 nM channel was always clear, and LOD evaluation by extrapolation (Figure 3.4c) yields different LOD/LOQs in the nM range (see Table 1 for a complete listing of LOD/LOQ values for all devices) for the microfluidic-AuFON devices. On a few occasions, the first channel, which should present no analyte, showed a low intensity BPE signal. This is due to an imperfection at the beginning of the device operation where BPE solution reached the detection terminal as bubbles were removed from the device, which can be easily corrected in future work.

	Fluorescence	Microfluidic-AuFON	Flexible SERS sensor	
			AuNR	AuNC
Device 1	0.30/0.90	5.76/17.46	0.69/2.09	0.86/2.61
Device 2	0.30/0.88	3.73/11.30	0.55/1.65	0.53/1.62
Device 3	0.50/1.50	2.83/8.58	0.44/1.33	0.42/1.27

Table 1. Values are in LOD/LOQ format. (Fluorescence: uM, AuFON: nM, Flexible: mM).

Interestingly, different BPE Raman bands result in differing slopes in linear regression analysis (Figure 3.5). This result is interesting because the peak heights are the product of the substrate enhancement factor (EF), Raman scattering cross-section, and concentration of the analyte. Assuming a constant EF with a known concentration of analyte in the channel, the slopes from all bands would be similar if the vibrational cross-sections were similar. Another potential explanation for this variation in slope could be due to the data processing and analysis routine where the presented data is obtained after baseline subtraction using an in-house algorithm. The algorithm is imperfect at choosing good baseline values, especially when the spectrum is crowded, and this could contribute to the variation in our linear regression analysis. Further analysis will be needed to delineate

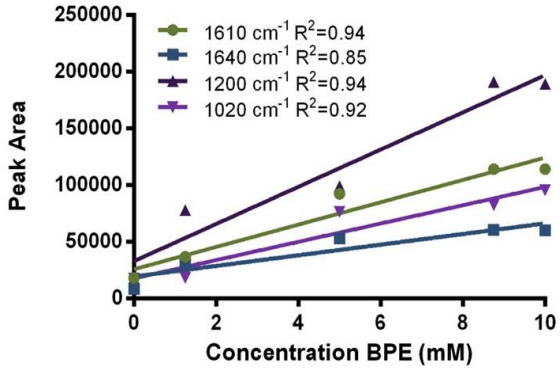

Figure 3.5. SERS response analysis a microfluidic-AuFON platform with 10 mM BPE whether this is an artifact of analysis or a true reflection of scattering cross-section differences among vibrational modes.

3.3.4 SERS assessment of the flexible microfluidic-SERS sensor device

The performance of the flexible SERS device was assessed using the same experimental system detailed above. The device performance was assessed in a step-by-

step fashion to characterize the performance of the Au nanoparticles embedded within the PDMS layer. As a preliminary experiment, a prototype straight channel microfluidic device was fabricated (Figure 3.6) with channel dimensions of 2000 μm (width) x 50 μm (height) x 25000 μm (length) with incorporated citrate-capped gold nanospheres (AuNSs). Without dry etching, a small SERS signal was recorded, indicating that at least some of the AuNSs were extruding out of PDMS surface to make contact with the in-channel analyte. However, the success rate of obtaining high quality SERS spectra was significantly lower than that achieved with devices that underwent reactive ion etching (Figure S3). Scanning electron microscopy (SEM) assessment of nanoparticle-embedded PDMS, after reactive ion etching, clearly demonstrates nanoparticles protruding from the PDMS surface. SERS spectra of 1 mM BPE and 1 mM benzenethiol, both well-known SERS probes, were successfully obtained using the preliminary flexible AuNS SERS platform (Figure 3.6c & 3.6d). All characteristic SERS bands for analytes were observed from both BPE and benzenethiol, and the enhancement factor was estimated to be between 5.9×10^4 and 4.1×10^7 (see Supplemental information for assumptions and calculation).[5] This enhancement factor range includes values higher than that achieved with the nanoparticles in solution, likely because embedded nanoparticles are no longer stabilized by citrate ligands and may occur in small aggregates.

With these preliminary data, we proceeded with well-characterized, high enhancement factor-producing AuNCs and AuNRs, both shown in Figure 3.7. All attempts to obtain LSPR measurements from the completed device were only marginally successful (Figure

S4). This is likely due to the small number density of nanoparticles in these experiments, but we could observe a slight LSPR l_{max} peak shift from the nanoparticles in a completed device when compared to the colloidal nanoparticles before incorporation into PDMS. The shift is probably due to formation of small nanoparticle aggregates within the PDMS media and the increased matrix refractive index by embedding at

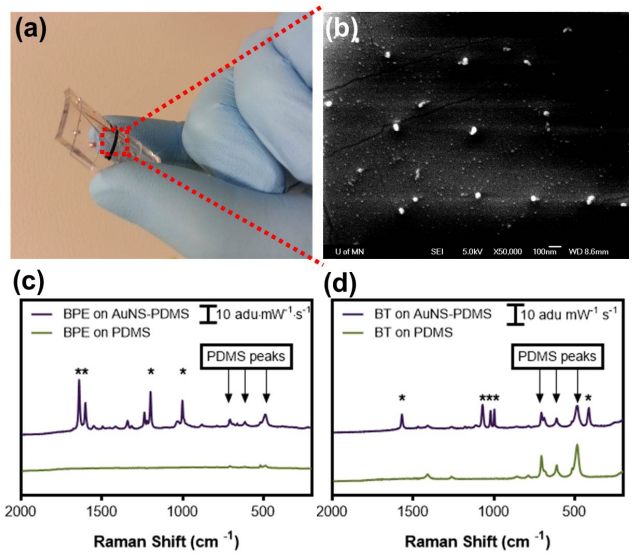

Figure 3.6. (a) Photograph of the prototype device. (b) SEM image showing nanoparticles extruding out of the PDMS surface. SERS spectra of (c) 1 mM BPE (*: BPE peaks) and (d) 1 mM benzenethiol (BT, *: BT peaks) obtained from the prototype device (λ_{ex}=785 nm, 10 second exposure, 3 mW power, and an average of 3 replicates on the Snowy Range Instrument).

least a portion of the nanoparticle in PDMS. Using the same microfluidic platform described for the microfluidic-AuFON sensor, AuNRs or AuNCs were directly embedded into the terminal channel array portion of the PDMS. 1 mM BPE was used as the analyte for this assessment; and as such, the expected concentrations for the five terminals were 0, 0.125, 0.5, 0.875, and 1 mM BPE. A linearity assessment was performed, comparing

the intensity of BPE's 1640 cm^{-1} shift band to PDMS's 490 cm^{-1} shift band (acting as an internal standard). While the LOD was higher than the microfluidic-AuFON platform, the flexible SERS sensor with both AuNRs and AuNCs also showed the expected linear response to BPE analyte (Figure 3.8). Using a PDMS peak as an internal standard yielded a moderate improvement in linearity for the AuNR devices (0.93 ± 0.01, mean ± standard error of the mean, compared to 0.90 ± 0.03). The R^2 value for AuNC devices was improved significantly (0.89 ± 0.03, mean ± standard error of the mean, compared to 0.69 ± 0.05) with this internal standard (Figure S5). Spatial variation in SERS responses within each terminal channel was also evaluated at 3 discrete, randomly chosen locations. SERS BPE band energies were similar; however, band intensities were somewhat variable. This is likely due to random NC dispersion in the PDMS or formation of localized electromagnetic hot spots. Together, these results demonstrate the utility of the embedded AuNR- and AuNC-based microfluidic-SERS sensors.

There are many opportunities for further optimization of these flexible devices during the fabrication process. For example, the exact amount of gold nanoparticles added to and protruding from the PDMS layer has not been optimized. It is already clear, as observed under dark-field microscopy (data not shown), that a thinner nanoparticle-containing PDMS layer will lead to more uniform presentation of nanoparticles on the surface of PDMS while also requiring a smaller number of nanoparticles. This will present an opportunity for more reproducible, and potentially

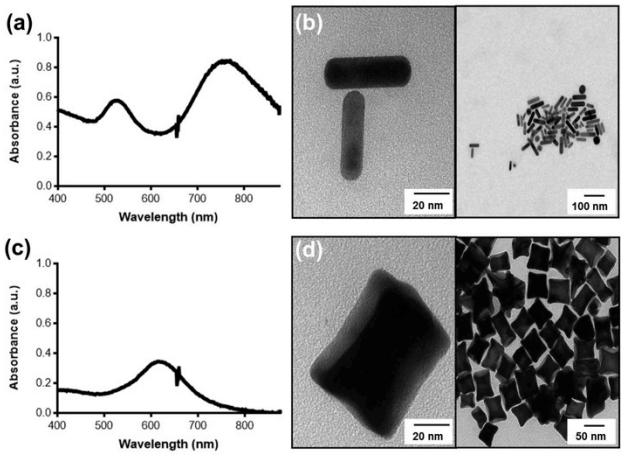

Figure 3.7. Nanoparticle characterization. LSPR measurement (a) and TEM images (b) of AuNRs and LSPR measurement (c) and TEM images (d) of AuNCs. *The extinction feature at ~680 nm is an instrumental artifact.

more sensitive, SERS measurements. Furthermore, many groups are working to optimize SERS enhancement factors by controlling gaps between nanoparticles (e.g., controlled fabrication of nanoparticle dimers or trimers).[5,18,50] In the flexible SERS sensor platform, nanoparticles are embedded and fixed with, presumably, only a portion of the nanoparticle protruding into the microfluidic channel. This may allow, for example, nanoparticle dimer formation with a reduced degree of freedom and enable extraordinarily sensitive SERS sensing.

3.4 Conclusions

Herein, we explored the use of two microfluidic SERS sensor platforms, a microfluidic-AuFON and a flexible microfluidic-SERS sensor, for on-line high enhancement factor, low volume SERS measurements. The microfluidics portion of the sensor platforms

provides desired control over the sample fluids, as simulated theoretically and verified experimentally, and varied concentrations of analyte for simultaneous assessment of LOD/LOQ by SERS measurements. While the dimension of the entire devices presented herein is relatively large (2.5 cm x 7.0 cm), because the aim here was to match the size of a standard microscope slide, the overall size can be easily adjusted as required by application or substrate dimensions. The material used for SERS detection is gold, a noble metal presenting minimum reactivity and toxicity to biological systems. Furthermore, the ease of surface functionalization of gold makes microfluidics-SERS approaches well suited for applications

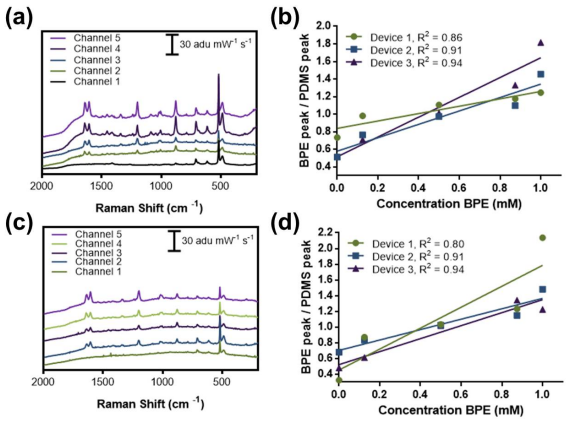

Figure 3.8. (a) Representative SERS spectra and (b) SERS response analysis from the flexible SERS sensor with embedded AuNRs, and (c) representative SERS spectra and (d) SERS response analysis from the flexible SERS sensor with embedded AuNCs. Solvent vs. 1 mM BPE solution was used as the analyte system.

where it is necessary to introduce biological functionalities (e.g., antibodies, aptamers, enzymes, nucleic acids, proteins, or small molecules).

Once incorporated with such surface functionalities, simultaneous detection of multiple analytes with high throughput should be easily achieved. Live cell imaging is another potential application for the presented sensor platforms as the flexible SERS sensor approach may provide an opportunity to allow membrane-specific SERS imaging. Further developments of our proof-of-concept microfluidic SERS sensor platforms will provide unique advantages to researchers in the bioanalytical sciences and bring significant impact in biomedical applications by providing opportunities for wearable sensors or on-site (portable) point-of-care devices.

Chapter 4. Gold Aggregates Encapsulated in Mesoporous Silica: An Ultrastable and Reversible pH Nanosensor

4.1 Introduction

Over the past decade, surface-enhanced Raman spectroscopy (SERS) has emerged as a powerful tool for biosensing applications based on the capacity to perform analyses in biological matrices with minimal interference from water.[1-5] The pH in biological systems is crucial to the stability of organisms. In particular, the pH of blood is carefully controlled to within 0.1 pH unit, and is critical for the health of vertebrates. The ability to monitor the pH of an invertebrate noninvasively through spectroscopic means would offer insight into the overall health of the organism. One critical sensing need is in intracellular pH level sensing for extended periods of time, and colloidal nanoparticle-based SERS may be one way to address this need. The current state-of-the-art continuous, long-term, intravascular pH sensor is a product named Paratrend 7+ and Neotrend. These devices can operate as optical or electrochemical detection, but suffer from several limitations including unreliable measurements with changes in blood flow, lack of robustness, bulky, and long warm-up times. Literature precedent shows the use of various SERS based systems based on gold and silver platforms for pH sensing applications; [6,7] however, these pH nanosensors have various limitations, such as toxicity in the case of silver, interference by proteins with the SERS tags in an intracellular environment, and uncontrollable aggregation of the nanoparticles.[8,9] These limitations either lead to an inherent lack of compatibility with biological systems or a sensor that

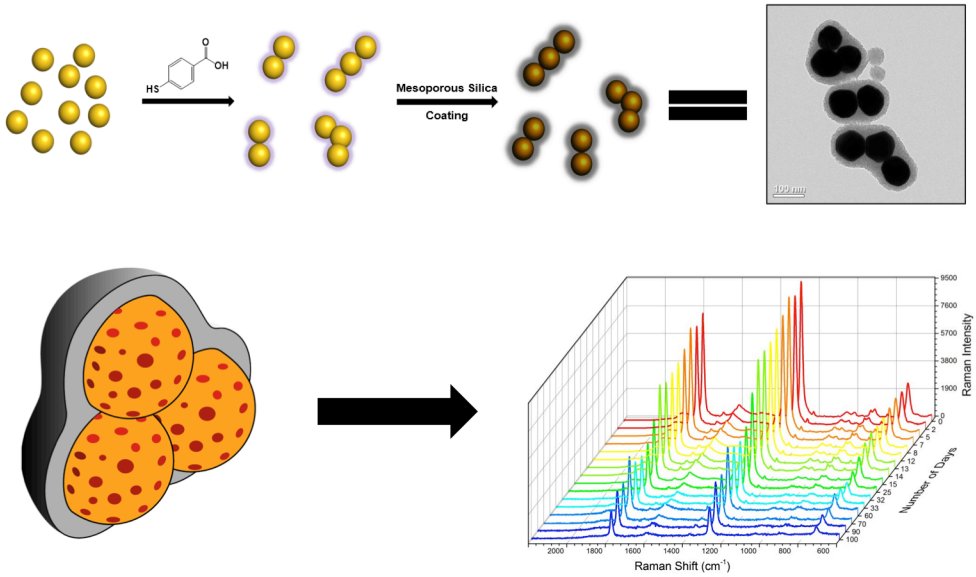

Figure 4.1. Overall synthesis and characterization of AuNPs@MBA@MS

cannot perform reproducibly. Recently, researchers have shown that encapsulating noble metal colloidal nanoparticles in a polymer or silica matrix can help combat the aggregation and stability concerns.[10, 11] A complication in using a coated SERS nanoparticle is that SERS signal transduction is a highly distance-dependent phenomenon, [12,13] where only analytes within about 5 nm of the noble-metal nanostructured surface experience the electromagnetic fields that lead to signal enhancement.[13] Thus, mesoporous silica coatings may facilitate protection of the SERS nanoparticle while also allowing analyte species to approach the plasmonic substrate.

Mesoporous silica shells offer the additional advantages of having a large surface area, tailorable chemical modification of the surface, and biocompatibility.[14]

Of the various pH nanosensors that have been fabricated, there is very little precedence for stability and reversible sensing in physiological conditions such as human whole blood. Another critical component of the pH nanosensor is the ability to recover the nanomaterial from human whole blood after the sensing experiments and then perform further measurements on the recovered nanoparticles. Recovery of the gold nanoparticles has not been shown in previous studies. The work herein demonstrates a pH nanosensing platform where a mesoporous silica-encapsulated gold nanoparticle aggregate facilitates SERS-based pH sensing in whole human blood.

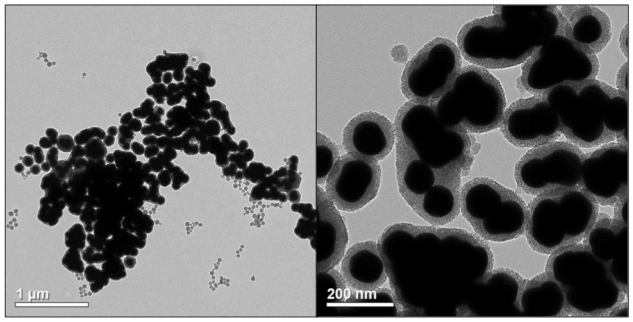

Figure 4.2. Representative TEM images of AuNPs@MBA@MS. Scale bars indicate 1 µm (left) and 200 nm (right).

4.2 Experimental

4.2.1 Materials Required. All chemicals were used as received. N-Cetyltrimethylammonium bromide (CTAB), tetraethyl orthosilicate (TEOS) were purchased from Sigma Aldrich. 2-[Methoxy(polyethyleneoxy)propyl] trimethoxysilane, (PEG-silane, MW 596-725 g/mol, 9-12 EO) was obtained from Gelest. Ammonium

nitrate (NH4NO3) and ammonium hydroxide (NH4OH, 28-30 wt% as NH3) were obtained from Mallinckrodt. Absolute anhydrous ethanol 99.5% was purchased from Pharmco-Aaper. The de-ionized (D.I.) water was generated using a Millipore Milli-Q system.

4.2.2 Characterization. Transmission electron microscopy (TEM) micrographs were taken on a JEOL 1200 EXII with a 100 kV voltage. Powder X-ray diffraction (XRD) patterns were measured on a Siemens Bruker-AXS D-5005 X-ray diffractometer using filtered Cu Kα radiation (λ= 1.5406 Å) at 45 kV and 20 mA. UV-vis measurements were performed on an Ocean Optics (Dunedin, Florida) spectrometer.

4.2.3 Preparation of mesoporous silica encapsulated gold aggregates functionalized with 4-MBA

4.2.3.1 ***Stanford Research Institute Nanoparticles:*** Nanoparticles acquired from SRI were comprised of 90 nm citrate capped Au spheres that were coated with 4-MBA, aggregated with sodium chloride, and coated with a proprietary polymer to prevent irreversible aggregation. The details of the synthesis and coating procedure remain a trade secret of SRI.

4.2.3.2 ***Mesoporous silica coating of gold aggregates:*** In a typical synthesis, 12 mg of CTAB and 2.88 mL Au aggregates (2 mg/mL) were dissolved in 21.12 mL of D.I. water under vigorous stirring at 50 °C. After 30 minutes of stirring, 424 μL of NH4OH

was added and the contents were stirred for another 15 minutes. 220 μL of 0.88 M TEOS was then added to the system and the contents were stirred for one hour. After one hour, 40 μL of PEG-silane was added to the as-synthesized colloidal solution. The mixture was stirred again at 50 °C for another 30 minutes and then the contents were transferred into a sealed vessel and hydrothermally treated at 90 °C for 24 hours. The as-synthesized solution was purified using ethanolic solution of ammonium nitrate (6 g/L). The surfactant-extracted nanoparticles were then washed twice with 99.5% anhydrous ethanol. The particles were re-dispersed in D.I. water for pH sensing measurements.

4.2.3.3 ***SERS measurements on bare gold aggregates and mesoporous silica coated gold aggregates:***

In a typical experiment, 1 ml of the nanoparticle solution is placed in a 1 dram glass vial. SERS measurements were performed using a SnowyRange instrument (Snowy Range Instruments, Laramie, WY) λ=785 nm, acquisition time 10 seconds with a laser power 3 mW.

4.2.3.4 ***Whole blood stability studies:*** To 0.5 ml of AuNPs was added 400 ul of human whole blood. The vial was sealed with parafilm and placed on an orbital shaker at room temperature to prevent coagulation of the blood.

4.3 Supplementary Figures

Figure 4.3. UV-Vis data before and after coating

Figure 4.4. Digital images showing the reversibility of the nanosensor using SDS treatment

4.4 Results

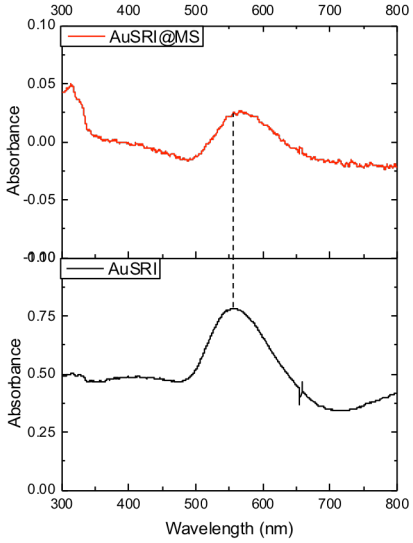

Figure 4.3. Extinction spectra of SRI nanoparticles before (AuSRI) and after mesoporous silica coating (AuSRI@MS)

These nanoparticles were coated with a 6-8 nm mesoporous silica shell that was hydrothermally treated to increase the stability of the particles.[14] To confirm that the particles were fully covered in mesoporous silica, TEM analysis was performed on the particles (Figure 4.2). To further verify that the particles are coated, UVvis measurements were performed and show a 5-10 nm wavelength shift after the coating.[15]

As detailed in Figure 4.3, the MBA is pH sensitive as the carboxylic acid is deprotonated and converted to the carboxylate ion resulting in the 1400 cm^{-1} peak. This process is reversible and can be cycled many times. The usable range of this sensor is from pH 3 to pH 10. In our experiments, the best sensitivity that we achieved was about 0.5 pH units. The purpose of coating the AuNPs with mesoporous silica is to increase stability.[14] To this end we have incubated the MS coated particles in human whole blood over the course of 100 days (Figure 4.5). After the 100-day incubation, the functionality of the pH

sensor was tested *via* a simplified acid-base titration. While the ammonium hydroxide and hydrochloric acid caused foaming of the blood the sensor still showed the characteristic 1400 cm^{-1} carboxylate peak upon base addition. In addition, the pH sensor was still reversible with the addition of acid. The capability of the sensor shows that even though the particles were in human whole blood they still functioned reasonably well. Adsorption of proteins to nanoparticles in complex matrices has been well studied.[16] While protein adsorption to nanosenors generally causes aggregation and sensor failure, the mesoporous coating ensures that the noble-metal surface and functionalization remains in tact despite protein adsorption.[16]

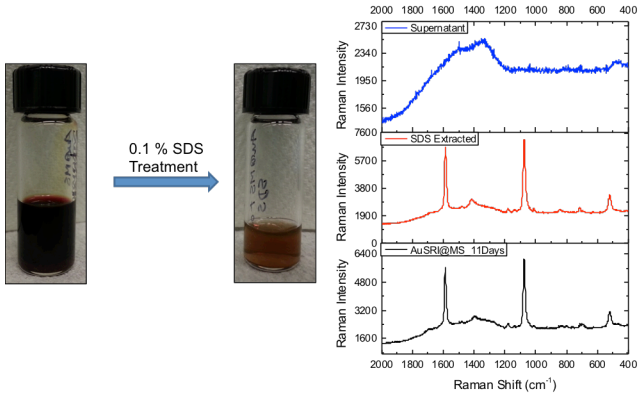

Figure 4.4. SERS Spectra of Recovered AuSRI@MS nanoparticles from human whole blood.

Recovery of the nanoparticles after exposure to blood shows the stability of the particles. The particles were recovered using two methods: bleach treatment and sodium dodecyl sulfate treatment. The first method, a 10% bleach solution for several minutes, was chosen because it is the traditional method for blood decontamination. Upon treatment of the solution with bleach, the solution color went from dark red to yellow. After centrifugation the supernatant was removed and saved for further analysis. The pellet was re-dispersed in water and exhibited a light pink color that resembled the color of the

original nanoparticle solution. Both the supernatant and the re-dispersed pellet were studied using Raman spectroscopy. Neither solution showed any of the original MBA Raman shifts. It is our hypothesis that the surface chemistry of the nanoparticles was oxidized with the bleach treatment while the Au nanoparticles remained in tact (from TEM analysis, data not shown). In order to keep the surface chemistry of the nanoparticles in tact, an SDS treatment was performed (i.e. the same protocol of centrifugation and re-dispersion was performed with SDS). Following the SDS treatment (Figure 4.4) the supernatant did not exhibit any of the MBA Raman shifts, while the re-dispersed pellet showed Raman shifts corresponding to MBA. In future experiments, the stability of the particles will be examined *in vivo* using surface-enhanced spatially offset Raman spectroscopy (SESORS).

Conclusions

While this study provided insight into the stability of mesoporous silica coated AuNPs, these results represent one replicate of stability in blood over 100 days. Due to the nature of this collaboration between SRI and the Haynes research group, the details about different batches of AuSRI nanoparticles were unavailable.

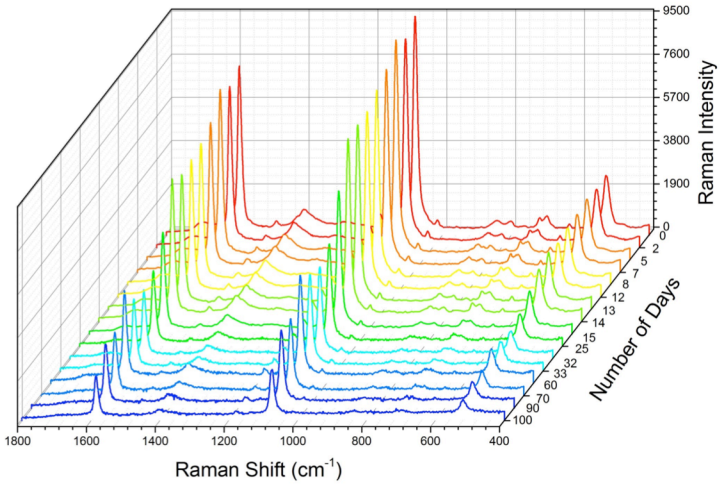

Figure 4.5. Stability of AUNP@@MBA@MS in human whole blood after 100 days

Chapter 5. An Investigation of Mesogold with Smartphone Colorimetry and Google Applications

5.1 Introduction

Spectrophotometry and colorimetry experiments are common in many high school and college chemistry courses. In many of these experiments, students utilize spectrophotometers and colorimeters to obtain absorbance or color intensity data to determine the concentration of a colored analyte in solution. Recent changes in state and national science education standards have guided teachers towards inquiry-based lab activities to support learning of classroom curriculum. The addition of International Society for Technology in Education (ISTE) technology standards for teachers and students has generated a need for lab experiments that utilize technology.[1] Recent teaching and learning models, such as Technological Pedagogical and Content Knowledge (TPACK), suggest that the use of technology combined with sound pedagogy and content knowledge improve student learning (tpack.org).[2] Recently Kehoe and Penn published a method for performing quantitative colorimetry utilizing a camera capable device, such as a smartphone, in place more traditional spectrophotometric or colorimetric equipment.[3] The use of smartphones coupled with data collection and analysis via Google applications can make sophisticated lab experiments more feasible, especially for teachers with limited budgets.[4,5] Here we describe an inquiry-based

investigation of the concentration of a mesogold colloidal gold mineral supplement, a medicinal supplement that claims to improve motor skills.[6] As smartphones and Google applications have become common tools for today's students in their everyday lives, it is sensible to exploit the technological advantages of this ubiquitous technology in the classroom. This investigation addresses this opportunity while also facilitating study of nanoscience, a topic of emerging importance and popularity in chemistry education.

5.2 Experimental Overview

5.2.1 Preparation of chemicals for standard gold nanoparticle suspension

Gold (III) chloride hydrate (10g, 484385 Sigma Aldrich, $394.50) and sodium citrate (1 kg, W302600, Sigma Aldrich, $68.00) were purchased and used as received. A 1.0 mM gold chloride solution was prepared by dissolving 0.200 g in enough Milli-Q water to produce 1.00 L of solution using a volumetric flask. A 38.8 mM sodium citrate solution was prepared by dissolving 2.00 g in enough Milli-Q water to produce 200 mL of solution using a volumetric flask.

5.2.2 Experiment

The MesoGold Colloidal Gold mineral supplement that students were given to analyze claims to have a concentration of at least 20 ppm gold particles, as indicated on the supplement's bottle and the distributor's website. Students were given the task of determining the concentration of gold nanoparticles in the supplement as well as the monetary value of the gold in a 250 mL bottle based on the determined concentration. The students synthesized a standard gold nanoparticle solution with a concentration of 100 ppm and then carried out a serial dilution with a dilution factor of one half down to at

least 6.25 ppm for calibration curve measurements. The students collected color intensity data to determine the absorbance of the gold nanoparticles in the standard solutions and the mineral supplement following Kehoe and Penn's methods for analysis.[3] Through a Beer's Law plot of the standard solutions, the students determined the concentration of the mineral supplement.

5.2.3 Preparation of 100 ppm standard gold nanoparticle solution

New or glassware cleaned with aqua regia is preferred, but not necessary as indicated by previous publication.[7] 20.0 mL of 1.0 mM gold (III) chloride stock solution was measured using a disposable 20 mL plastic pipet tip with rubber bulb and placed in a 125 mL Erlenmeyer flask. The solution was brought to 100.0 ^{o}C on a hot plate while stirring. As the solution began to boil, 2.0 mL of 38.8 mM sodium citrate stock solution was added using a disposable 10 mL plastic pipet tip with rubber bulb. The solution was allowed to continue boiling until a ruby red color was observed. The solution was removed from the heat and allowed to cool to room temperature. The solution volume was brought to 22 mL by addition of Milli-Q water to account for evaporative loss to bring the final solution concentration to 100 ppm.

5.3 Data Collection

The students photographed their dilution series along with a blank sample and a MesoGold Colloidal Gold Mineral Supplement sample in polystyrene cuvettes with a smartphone (Figure 1). Students adjusted the location and lighting in attempt to minimize shadows. The students used a free color picker application of their choice to collect three green intensity values from each sample. The students only used the green channel as it is

the most complementary to the red colored solutions and thus would yield the most quantitative results.[3]

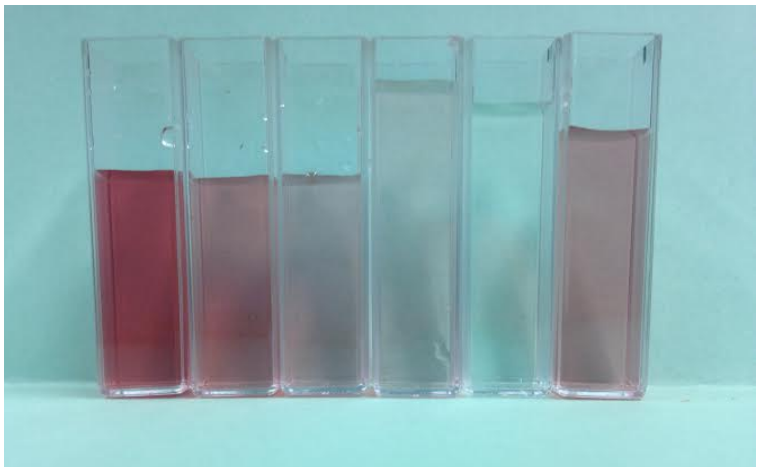

Figure 5.1. Photograph of 50 ppm, 25 ppm, 12.5 ppm, and 6.25 ppm standards, blank, and MesoGold sample respectively.

5.4 Data Analysis

The concentrations of the solutions and green intensity values collected from each group were entered into a Google Spreadsheet shared amongst the members of the group. An average green intensity was calculated and translated into an absorbance value using the spreadsheet tools and Equation 1 where I is the average green intensity of each standard solution and I_o is the average green intensity of the blank.

$$\text{Absorbance} = -\log(I/I_o) \qquad \text{(Equation 1)}$$

The concentration and absorbance values were plotted. The students used the equation for the line of best fit to determine the concentration of the mesogold sample (Figure 2).

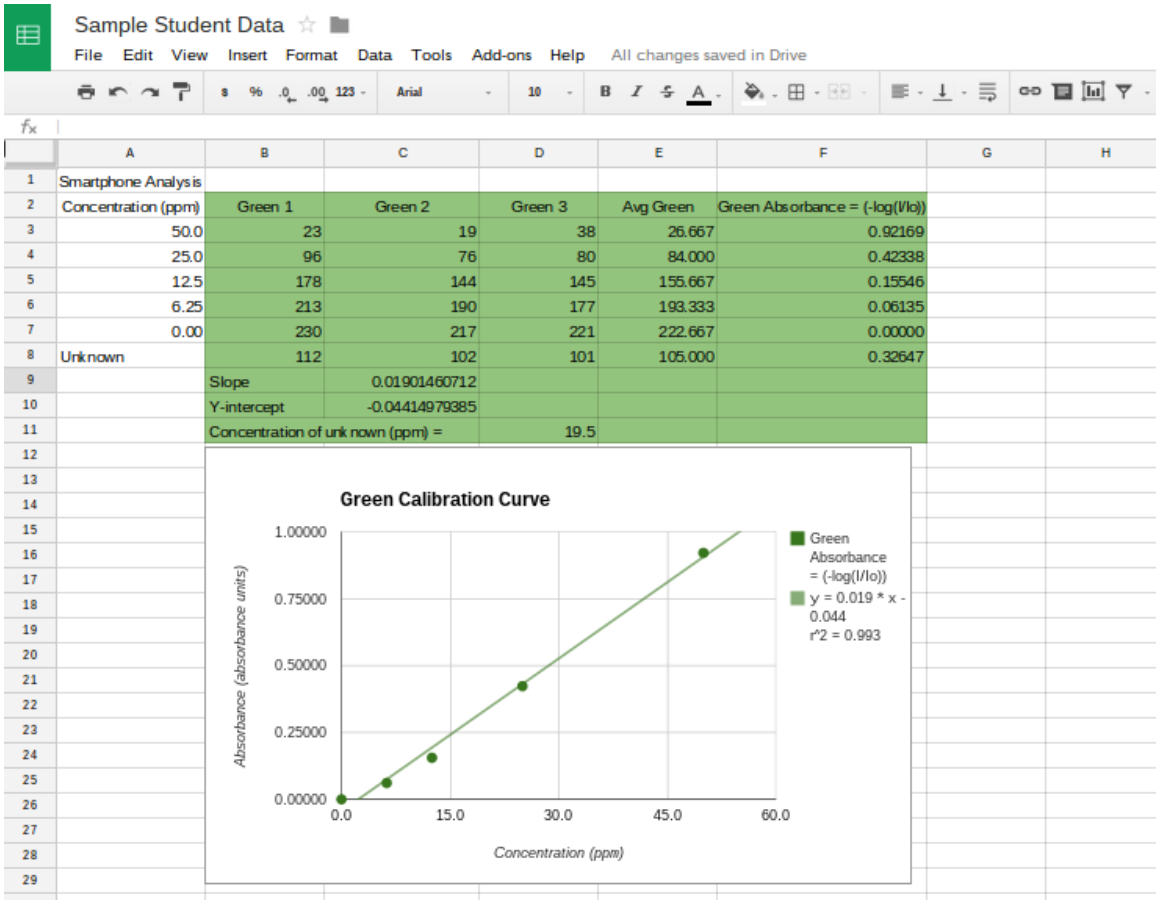

	A	B	C	D	E	F	G	H
1	Smartphone Analysis							
2	Concentration (ppm)	Green 1	Green 2	Green 3	Avg Green	Green Absorbance = (-log(I/Io))		
3	50.0	23	19	38	26.667	0.92169		
4	25.0	96	76	80	84.000	0.42338		
5	12.5	178	144	145	155.667	0.15546		
6	6.25	213	190	177	193.333	0.06135		
7	0.00	230	217	221	222.667	0.00000		
8	Unknown	112	102	101	105.000	0.32647		
9		Slope	0.01901460712					
10		Y-intercept	-0.04414979385					
11		Concentration of unknown (ppm) =		19.5				

Figure 5.2. Sample student data analysis from the colorimetric smartphone method using a Google Spreadsheet.

Following spreadsheet analysis, students generated collaborative lab reports using Google documents, while receiving timely instructor feedback through the commenting tool. Students shared their data and results with a broader audience of chemistry professionals and experts through Google hangouts.

5.5 Hazards

Gold chloride may be harmful if swallowed or inhaled and can cause irritation to the skin, eyes and respiratory tract. Skin contact with sodium citrate should be avoided as it

can cause irritation to the skin, eyes and respiratory tract. Nanoparticle solutions should be disposed of in accordance to local hazardous waste procedures. Safety glasses and gloves should be worn at all times. Clean up spills immediately and consult SDSs for complete safety information. Personal electronic devices, such as smartphones, may be placed inside clear plastic bags to limit contamination of devices with chemicals.

5.6 Discussion

12 of the 15 participating student groups successfully followed the experimental procedure and analysis. The average concentration of the MesoGold mineral supplement was determined to be 22 (±4) ppm by smartphone analysis with the advertised concentration of MesoGold as 20 ppm. The student groups that were unsuccessful in determining the concentration of mesogold by smartphone analysis had issues with dirty equipment, made mistakes in their dilution of the 100 ppm standard solution, or were unable to obtain a quality image for analysis. As previously published,[3] images that yield the best results can be acquired by using an appropriately colored background, an image acquisition application that locks the focal plane of the camera, and by minimizing fluctuations of the ambient light.

In Figure 2, representative data from the color picker app on a smartphone is represented. Google Spreadsheet offers the ability to calculate the calibration curve and correlation value for the line of best fit (in this classroom setting the students had access to Chromebooks). The functionality of Google Spreadsheet is adequate to perform the necessary analysis for these experiments, and more importantly can offer immediate

feedback to the students if their analysis is incorrect as teachers can respond to their analysis in real time. In addition, the ability to observe students performing data analysis in one shared space offers the ability to correctly assess the participation of a student working in a group. This also offers the students the opportunity to work collaboratively on a project online and contribute separately to the same document, which removes the ambiguity of assigning participation. In addition, students can work on separate aspects of the data analysis and check their work against other group members if they are unsure about the analysis.

A template of the spreadsheet was provided to the students to teach the methods that are offered in Google Spreadsheet. While students performed the analysis with guidance from the template, they distributed their workload independently. Google also offers a streamlined approach to distributing the template to the students *via* Classroom.[8] Google Classroom is available to educators with a Google Apps for Education account.

5.7 Conclusion

A camera capable device can be used to determine the concentration of mesogold in MesoGold Colloidal Gold Mineral Supplement. The combination of a camera capable device and free Google applications provides a unique and viable lab experience for high school and college chemistry students to explore fundamental chemistry concepts in the context of nanoscience. The use of Google applications facilitates efficient instruction and feedback between the students and teachers for effective collaboration.

5.8 Student Activity

5.8.1 Objective:

In this activity you will learn about nanoparticles, synthesize gold nanoparticles, and study the concentration of gold nanoparticles using a smartphone or tablet device.

5.8.2 Learning about Nanoparticles

5.8.2.1 Pre-Reading Questions:

1. Where have you heard the term nano?

2. What does the term nano mean to you?

3. What do you know about nanoscience or nanomaterials?

An Introduction to Nanoparticles:

A nanoparticle is a nanoscale particle. One nanometer is 1×10^{-9} meters. To put this in perspective, one nanometer is 10,000 times smaller than the diameter of a single human hair.[7] Nanoscience investigates the properties of nanomaterials. New and emerging applications for nanomaterials makes our understanding of them increasingly important. Nanoparticles can be found in paints, cosmetics, medicines, electronics, and food, and other places. While nanoparticles can be found in nature, but can also be

synthetically produced in laboratories. Transmission electron microscopes (TEM) are used to characterize the size and shape of nanoparticles.

The physical properties of nanoparticles are size dependant. For example, a bulk sample of gold, such as in jewelry, appears yellow, but a solution of nano-sized gold particles can appear as a variety of colors depending on their size. The variation in color is a result of how the particles interact with light. Large particles interact with light differently than small particles. The chemical properties of nanoparticles are also size dependant. For example, small particles have high surface area, giving the particles potential for high reaction speeds.

5.8.2.2 Post-Reading Questions:

1. What is the relative size of a nanoparticle?

2. How are nanoparticles characterized?

3. Why is bulk gold yellow in color, but nano-sized gold not?

4. What gives nanoparticles the potential for high speed of reaction?

5. What are some of the current applications of nanoparticles?

5.8.3 Synthesis of Gold Nanoparticle Solution (100 ppm):

5.8.3.1 Materials needed:

- 20.0 mL of 1.0 mM gold chloride ($AuCl_3$) stock solution
- 2.0 mL of 38.8 mM sodium citrate ($Na_3C_6H_5O_7 \cdot 2H_2O$) stock solution
- 125 mL Erlenmeyer flask
- stir bar
- stir/hot plate

5.8.3.2 Procedure:

- Add 20.0 mL of 1.0 mM gold chloride stock solution to a 125 mL Erlenmeyer flask.
- Bring the gold chloride solution to a boil (100^oC) while stirring on a hot plate.
- As the solution begins to boil, add 2.0 mL of sodium citrate stock solution.
- Continue to boil for 10 minutes or until a ruby red color has been observed.
- Remove the solution from heat and allow it to cool to room temperature.
- Bring solution volume to a total of 22 mL by addition of distilled water. (This will account for evaporative loss of water and will yield a final concentration of 100 ppm.)

5.8.3.3 Observations and Lab Notes:

5.8.3.4 Studying the Concentration of Gold Nanoparticles

5.8.3.5 Purpose:

Using your 100 ppm sample of gold nanoparticles as a standard, determine the concentration of gold nanoparticles in MesoGold Colloidal Gold Mineral Supplement.

What is MesoGold Colloidal Gold Mineral Supplement?:

The following was taken from the World Wellness Store's advertisement for MesoGold Colloidal Gold Mineral Supplement:

Colloidal gold is nanoparticles of pure gold suspended in pure water. The gold nanoparticles in MesoGold are a few nanometers in diameter. These particles are so small they can only be seen by the most powerful electron microscopes available today. These particles stay suspended in pure deionized water and do not fall to the bottom. It is these suspended particles that make MesoGold a true colloid. MesoGold is the most effective Colloidal Gold. Most products advertised as being colloidal gold are produced using an electrolysis process that produces gold particles that are typically 70-120 nanometers (nm) in diameter. These particles are very large compared to the nanoparticles in MesoGold. The much smaller size of the gold nanoparticles in MesoGold produce a much higher particle surface area than other brands. It is the particle surface area which determines the effectiveness of a colloid.

Gold has been known through the ages to have a direct effect on the activities of the heart and helps to improve blood circulation. It is beneficial for rejuvenating sluggish organs, especially the brain and digestive system, and has been used in cases of glandular and nervous congestion and lack of coordination. The body's temperature stabilizing mechanism is restored to balance with gold, particularly in cases of chills, hot flashes, and night sweats. Colloidal gold has a balancing and harmonizing effect on all levels of body, mind, and spirit. It is used to improve mental attitude and emotional states. It has been reported to promote a feeling of increased energy, will power, mental focus, and libido. According to many studies, colloidal gold increases mental acuity and the ability

to concentrate. Colloidal gold is thought to strengthen mental function by increasing the conductivity between nerve endings in the body and on the surface of the brain.

MesoGold should be taken in the morning on an empty stomach 15-20 minutes before eating for maximum absorption. The nominal adult dosage for MesoGold is one tablespoon (15mL) daily but optimum dosage must be determined for each individual. Most adults will find their optimum dosage will be between 1 and 4 tablespoons.

5.8.3.6 Preparation of Standard Solutions for Calibration Curve:

5.8.3.6.1 Background:

A calibration curve is a method that can be used to determine the concentration of a substance in an unknown sample by comparison of the unknown sample to a set of standard solutions with known concentrations. Your 100 ppm gold nanoparticle solution will be diluted in order to prepare the standard solutions. Dilution involves reducing the concentration of a solution by adding a particular amount of distilled water to a particular amount of stock solution. To calculate how much stock solution and distilled water are required to make an amount of a less concentrated solution the dilution equation can be used:

Equation 1: $M_1V_1 = M_2V_2$

where M_1 is the molarity of the stock solution, V_1 is the volume of the stock solution required to make the desired diluted solution, M_2 is the molarity of the desired diluted solution, and V_2 is the volume of the desired diluted solution.

Example: If 4.0 mL of a 50 ppm solution is desired the amount of 100 ppm stock solution and distilled water can be calculated as follows:

$M_1V_1 = M_2V_2$

$M_1 = 100$ ppm

$V_1 = ?$

$M_2 = 50$ ppm

$V_2 = 4.0$ mL

100 ppm (V_1) = 50 ppm (4.0 mL)

$V_1 = 2.0$ mL

2.0 mL of the 100 ppm stock solution is needed to create a 50 ppm solution. To reach a total volume of 4.0 mL, 2.0 mL of distilled water must be added.

A serial dilution involves using the previous diluted solution to make the next solution. Fill in the table below and then complete the serial dilution.

Table 1. Volumes of stock solution and distilled water for standard solutions

	50 ppm	25 ppm	12.5 ppm	6.25 ppm	3.125 ppm
Volume of Gold Nanoparticle Solution	Volume of 100 ppm Solution = 2.0 mL	Volume of 50 ppm Solution =	Volume of 25 ppm Solution =	Volume of 12.5 ppm Solution =	Volume of 6.25 ppm Solution =
Volume of distilled water	2.0 mL				
Total volume	4.0 mL	4.0 mL	4.0 mL	4.0 mL	4.0 mL

5.8.3.6.2 Collection of Image to Determine Concentration of MesoGold:

Procedure:

1. Fill a cuvette with 2.0 mL of the 50 ppm solution. Repeat this with the other standard solutions, distilled water, and the unknown.
2. Line up the cuvettes against a green or white background and foreground.

3. Position a smartphone or other camera capable device approximately 12 inches from the solutions. Adjust the positions of the solutions and smartphone or other device or the lighting to minimize shadows or glare in the images.
4. Take an image

5.8.3.6.3 Analysis of Image:

Procedure:

Analysis of the images with a color picker application can be completed on the smartphone or other camera capable device used for image collection or images can be transferred to a computer for analysis. To assist with data analysis an example data table and calculations are provide below.

1. Starting with the 50 ppm solution, use a color picker application to measure the green color intensity at three locations in the sample.
2. Repeat this for the 25 ppm solution, 12.5 ppm solution, 6.25 ppm solution, 3.125 ppm solution, and blank.
3. Calculate the average green color intensity for each solution and blank.
4. Convert each of the average green color intensities to an absorbance using equation X.
5. Prepare the calibration curve by plotting the absorbance versus concentration of each solution and blank.

6. Determine the slope and y-intercept for the line of best fit and put them into y = mx + b format. In this equation y represents the absorbance and x represents the concentration. This equation will allow for determining the concentration of the reaction mixture given an absorbance of the mixture at each time point.
7. Starting with the image used for the calibration curve measure the green color intensity of the reaction mixture at three locations.
8. Repeat this for each time point.
9. Calculate the average green color intensity of the reaction mixture at each time point.
10. Convert the average green color intensity from each time point to an absorbance using equation 6.
11. Convert the absorbance values to concentration values using the equation determined by the calibration curve in step 7.
12. Calculate ln(concentration) for each time point
13. Calculate 1/(concentration for each time point.
14. Construct three plots using Excel, Google spreadsheets, or a similar program:

a. concentration versus time
b. ln(concentration) versus time
c. 1/(concentration) versus time

15. Assess the linearity of each plot to determine the integrated rate law and the order of the reaction with respect to crystal violet. A correlation coefficient (R^2) may be useful in assessing the linearity of the plots.
16. Construct a table similar to table 2. Example calculations can be found below.

Table 2. Example data table

Time (seconds)	Measured Green Intensity #1	Measured Green Intensity #2	Measured Green Intensity #3	Calculated Average Intensity	Calculated Absorbance
30	64	67	69	66.667	0.383
40					
50					
...					

Example Calculations:

Average Intensity:

Average Intensity =Green Intensity #1 + Green Intensity #2 + Green Intensity #33= 64 + 67 + 693=66.667

Absorbance:

If the average green intensity of blank was 161

Absorbance =-log(I/Io)=-log(66.667/161)=0.383

Concentration:

If the y = mx + b equation from calibration curve was y = 0.0503x + -0.0461 (where y is the absorbance and x is the concentration)

0.383 =0.0503x+-0.0461

x = 8.517

5.8.4 Post-Lab Questions:

1. Estimate the worth of the gold in the MesoGold supplement?

Chapter 6. Conclusions and Future Work

Raman spectroscopy applied to the forensic analysis of biological solutions including blood, urine, saliva, etc is an emerging field. In Chapter 1, the analysis of blood utilizing Raman spectroscopy was reviewed and featured because of the non-destructive method of analysis and the usefulness of Raman spectroscopy in forensic science as handheld Raman spectrometers are becoming commonplace. While Raman spectroscopy is known for a lack of sensitivity, creative sample preparations and the use of nanomaterials has allowed the field to continually improve in attempts to overcome the limited Raman scattering intensities. Chapter 2 detailed the work of utilizing nanoscaled materials to enhance the signal of Raman spectroscopy for the detection of a component of the cell-binding component of ricin in human whole blood. In addition to the detection of ricin B chain at a biologically relevant concentration, the work allowed for the improvement of AgFONs as a substrate. This improvement in substrates allowed for the development of the microfluidic-SERS devices in Chapter 3.

The microfluidic-SERS devices performed remarkably well for the detection of BPE. While these devices were originally developed to be incorporated into the detection of ricin B chain in human blood, the aptamers that were used could not be observed in the channels of the device. This setback allowed for the development of nanoparticles that could be mixed with the biological solutions detailed in Chapter 4. Chapter 4 only details the beginning of this work and there is much left to be discovered. However, the

improvement of the stability of nanoparticles in biological solutions, while maintaining the ability to perform detection was proven in Chapter 4.

In the fifth chapter, an outreach activity introducing nanomaterials was organized and conducted with an AP Chemistry class from White Bear Lake High School. This work elucidates the possibilities of nanoscience to be performed with high school students on a limited budget. The students overall response was positive and helped to introduce nanoscience to a new generation of future scientists.

Bibliography

References

Chapter 1.

(1) Fleischmann, M.; Hendra, P. J.; McQuillan, A. J. *Chemical Physics Letters* **1974**, 26, 163-166.
(2) Mach, K. E.; Wong, P. K.; Liao, J. C. *Trends Pharmacol. Sci.* **2011**, *32*, 330–336.
(3) Smekal, A. *Naturwissenschaften* **1923**, *11*, 873–875.
(4) Raman, C. V.; Krishnan, K. S. *Nature* **1928**, *122*, 169–169.
(5) Raman, C. V. *Indian Journal of Physics* **1928**.
(6) Haynes, C. L.; McFarland, A. D.; Duyne, R. P. V. *Anal Chem* **2005**, *77*, 338A–346A.
(7) McCreery, R. L. In *Raman Spectroscopy for Chemical Analysis*; McCreery/Raman Spectroscopy; John Wiley & Sons, Inc.: Hoboken, NJ, USA, 2005; pp. 293–332.
(8) Willets, K. A.; Van Duyne, R. P. *Annu Rev Phys Chem* **2007**, *58*, 267–297.
(9) Jeanmaire, D. L.; Van Duyne, R. P. *Journal of Electroanalytical Chemistry and Interfacial Electrochemistry* **1977**, *84*, 1–20.
(10) Tolles, W. M.; Nibler, J. W.; McDonald, J. R.; Harvey, A. B. *Appl Spectrosc* **1977**, *31*, 253–271.
(11) Kneipp, K.; Kneipp, H.; Itzkan, I.; Dasari, R. R.; Feld, M. S. *Chemical Physics* **1999**.
(12) Anderson, M. S. *Appl. Phys. Lett.* **2000**, *76*, 3130–3132.
(13) Schatz, G. C.; Young, M. A.; Duyne, R. P. In *Surface-enhanced Raman ...*; Topics in Applied Physics; Springer Berlin Heidelberg, 2006; Vol. 103, pp. 19–45.
(14) Tyler, T. P.; Henry, A. I.; Van Duyne, R. P. *The Journal of Physical Chemistry* **2011**.
(15) Qin, L. *Science* **2005**, *309*, 113–115.
(16) Zheng, G.; Qin, L.; Mirkin, C. A. *Angew. Chem. Int. Ed.* **2008**, *47*, 1938–1941.
(17) Greeneltch, N. G.; Blaber, M. G.; Henry, A.-I.; Schatz, G. C.; Van Duyne, R. P. *Anal Chem* **2013**, *85*, 2297–2303.
(18) Jensen, T. R.; Duval, M. L.; Kelly, K. L.; Lazarides, A. A.; Schatz, G. C.; Van Duyne, R. P. *J. Phys. Chem. B* **1999**, *103*, 9846–9853.
(19) Haynes, C. L.; Van Duyne, R.P. *J Phys Chem B,* **2001**, 105, 5599-5611.
(20) Drabkin, D. L. A. *Physiological Reviews* **1951**, *31*, 345–431.
(21) Lucia, S. P.; Hunt, M. L. *The American Journal of the Medical Sciences KW* - **1947**, *213 N2* .
(22) Osgood Arthur J A2, E. E. S. *Physiological Reviews* **1944**, *24*, 46–69.

(23) Wintrobe, M. M. *Clinical Hematology (2nd ed.)* Philadelphia:Lea, 1946.
(24) Vaughan, S. L.; Brockmyre, F. *Blood* **1947**, 54–59.
(25) Virkler, K.; Lednev, I. K. *Analyst* **2010**, *135*, 512.
(26) Virkler, K.; Lednev, I. K. *Forensic Sci. Int.* **2009**, *188*, 1–17.
(27) Virkler, K.; Lednev, I. K. *Forensic Sci. Int.* **2009**, *193*, 56–62.
(28) Virkler, K.; Lednev, I. K. *Anal Bioanal Chem* **2009**, *396*, 525–534.
(29) National Institute of Justice; Justice, U. D. O. **1989**.
(30) Spalding, R. P. Identification and characterization of blood and bloodstains; in Forensic Science: an introduction to scientific and investigive techniques, **2003**. James, S. H. and Nordby, J. J. (eds.) pp. 181-201, CRC Press, Boca Raton, USA.
(31) Barni, F.; Lewis, S. W.; Berti, A.; Miskelly, G. M.; Lago, G. *Talanta* **2007**, *72*, 896–913.
(32) Webb, J. L.; Creamer, J. I.; Quickenden, T. I. *Luminescence* **2006**, *21*, 214–220.
(33) Shaler, R. C. *Forensic Science Handbook* **2002**.
(34) Sottolano, S.; Deforest, P. R. *Microscope*, **1980** , *28***,** 41–46.
(35) Virkler, K.; Lednev, I. K. *Forensic Sci. Int.* **2008**, *181*, e1–e5.
(36) Virkler, K.; Lednev, I. K. *Anal Chem* **2009**, *81*, 7773–7777.
(37) Shafer-Peltier, K. E.; Haynes, C. L.; Glucksberg, M. R.; Van Duyne, R. P. *J. Am. Chem. Soc.* **2003**, *125*, 588–593.
(38) Premasiri, W. R.; Lee, J. C.; Ziegler, L. D. *J. Phys. Chem. B* **2012**.
(39) Rein, A. J.; Saperstein, D. D.; Pines, S. H.; Radlick, P. C. *Experientia* **1976**, *32*, 1352–1354.
(40) Sato, H.; Chiba, H.; Tashiro, H.; Ozaki, Y. *J Biomed Opt* **2001**, *6*, 366–370.
(41) Premasiri, W. R.; Lee, J. C.; Ziegler, L. D. *J. Phys. Chem. B* **2012**, *116*, 9376–9386.
(42) Philip, L.; Altmann, D.; Dittmer, S. *Federation of Amer Societies for Experimental ...* **1971**.
(43) Bonifacio, A.; Dalla Marta, S.; Spizzo, R.; Cervo, S.; Steffan, A.; Colombatti, A.; Sergo, V. *Anal Bioanal Chem* **2014**.
(44) Lemler, P.; Premasiri, W. R.; Delmonaco, A.; Ziegler, L. D. *Anal Bioanal Chem* **2014**, *406*, 193–200.
(45) Mahmood, U.; Weissleder, R. *Mol. Cancer Ther.* **2003**, *2*, 489–496.
(46) Trachta, G.; Schwarze, B.; Sägmüller, B.; Brehm, G. *Journal of molecular ...* **2004**.
(47) Teh, S. K.; Zheng, W.; Ho, K. Y.; Teh, M.; Yeoh, K. G.; Huang, Z. *Br. J. Cancer* **2008**, *98*, 457–465.
(48) Stuart, D. A.; Yuen, J. M.; Shah, N.; Lyandres, O.; Yonzon, C. R.; Glucksberg, M. R.; Walsh, J. T.; Van Duyne, R. P. *Anal Chem* **2006**, *78*, 7211–7215.
(49) Shah, N. C.; Lyandres, O.; Walsh, J. T.; Glucksberg, M. R.; Van Duyne, R. P. *Anal Chem* **2007**, *79*, 6927–6932.
(50) Lee, S. H.; Bantz, K. C.; Lindquist, N. C.; Oh, S.-H.; Haynes, C. L. *Langmuir* **2009**, *25*, 13685–13693.

(51) Yuen, C.; Zheng, W.; Huang, Z. *Biosensors and Bioelectronics* **2010**.
(52) Liu, T.-Y.; Tsai, K.-T.; Wang, H.-H.; Chen, Y.; Chen, Y.-H.; Chao, Y.-C.; Chang, H.-H.; Lin, C.-H.; Wang, J.-K.; Wang, Y.-L. *Nat Comms* **2011**, *2*, 538–.
(53) Hsu, P. H.; Chiang, H. K. *J. Raman Spectrosc.* **2010**.
(54) Firdous, S.; Nawaz, M.; Ahmed, M.; Anwar, S.; Rehman, A.; Rashid, R.; Mahmood, A. *Laser Phys.* **2012**, *22*, 1090–1094–1094.
(55) Wang, Y.; Lee, K.; Irudayaraj, J. *Chem. Commun. (Camb.)* **2010**, *46*, 613–615.
(56) Stevenson, R.; Stokes, R. J.; MacMillan, D.; Armstrong, D.; Faulds, K.; Wadsworth, R.; Kunuthur, S.; Suckling, C. J.; Graham, D. *Analyst* **2009**, *134*, 1561–1564.
(57) Casella, M.; Lucotti, A.; Tommasini, M.; Bedoni, M.; Forvi, E.; Gramatica, F.; Zerbi, G. *Spectrochimica Acta Part A: Molecular and Biomolecular Spectroscopy* **2011**, *79*, 915–919.
(58) Qian, X.; Peng, X.-H.; Ansari, D. O.; Yin-Goen, Q.; Chen, G. Z.; Shin, D. M.; Yang, L.; Young, A. N.; Wang, M. D.; Nie, S. *Nat Biotechnol* **2007**, *26*, 83–90.
(59) Bashkatov, A. N.; Genina, E. A.; Kochubey, V. I.; Tuchin, V. V. *J. Phys. D: Appl. Phys.* **2005**, *38*, 2543–2555.
(60) Nielsen, K. P.; Zhao, L.; Stamnes, J. J.; Stamnes, K. *Norw Acad Sci …* **2008**.
(61) Matousek, P.; Morris, M. D.; Everall, N.; Clark, I. P.; Towrie, M.; Draper, E.; Goodship, A.; Parker, A. W. *Appl Spectrosc* **2005**, *59*, 1485–1492.
(62) Matousek, P.; Clark, I. P.; Draper, E. R. C.; Morris, M. D.; Goodship, A. E.; Everall, N.; Towrie, M.; Finney, W. F.; Parker, A. W. *Appl Spectrosc* **2005**, *59*, 393–400.
(63) Schulmerich, M. V.; Finney, W. F.; Fredricks, R. A.; Morris, M. D. *Appl Spectrosc* **2006**, *60*, 109–114.
(64) Matousek, P. *Appl Spectrosc* **2006**, *60*, 1341–1347.
(65) Schulmerich, M. V.; Dooley, K. A.; Morris, M. D.; Vanasse, T. M.; Goldstein, S. A. *J Biomed Opt* **2006**, *11*, 060502.
(66) Olds, W. J.; Jaatinen, E.; Fredericks, P.; Cletus, B.; Panayiotou, H.; Izake, E. L. *Forensic Sci. Int.* **2011**, *212*, 69–77.
(67) Eliasson, C.; Matousek, P. *Anal Chem* **2007**, *79*, 1696–1701.
(68) Schulmerich, M. V.; Cole, J. H.; Kreider, J. M.; Esmonde-White, F.; Dooley, K. A.; Goldstein, S. A.; Morris, M. D. *Appl Spectrosc* **2009**, *63*, 286–295.
(69) Macleod, N. A.; Matousek, P. *Appl Spectrosc* **2008**, *62*, 291A–304A.
(70) Matousek, P.; Draper, E. R. C.; Goodship, A. E.; Clark, I. P.; Ronayne, K. L.; Parker, A. W. *Appl Spectrosc* **2006**, *60*, 758–763.
(71) Keller, M. D.; Majumder, S. K.; Mahadevan-Jansen, A. *Opt Lett* **2009**, *34*, 926–928.
(72) Keller, M. D.; Wilson, R. H.; Mycek, M.-A.; Mahadevan-Jansen, A. *Appl Spectrosc* **2010**, *64*, 607–614.
(73) Keller, M. D.; Vargis, E.; de Matos Granja, N.; Wilson, R. H.; Mycek, M.-A.; Kelley, M. C.; Mahadevan-Jansen, A. *J Biomed Opt* **2011**, *16*, 077006–077006–

8.
(74) Holme, T. C.; Reis, M. M.; Thompson, A.; Robertson, A.; Parham, D.; Hickman, P.; Preece, P. E. *Eur J Surg Oncol* **1993**, *19*, 250–253.
(75) MJ, R. *Arch Pathol Lab Med* **1989**, *113*, 1367–1369.
(76) Haka, A. S.; Shafer-Peltier, K. E.; Fitzmaurice, M.; Crowe, J.; Dasari, R. R.; Feld, M. S. *Cancer Res.* **2002**, *62*, 5375–5380.
(77) Stone, N.; Baker, R.; Rogers, K.; Parker, A. W.; Matousek, P. *Analyst* **2007**, *132*, 899–905.
(78) Stone, N.; Faulds, K.; Graham, D.; Matousek, P. *Anal Chem* **2010**, *82*, 3969–3973.
(79) Stone, N.; Kerssens, M.; Lloyd, G. R.; Faulds, K.; Graham, D.; Matousek, P. *Chem. Sci.* **2011**, *2*, 776–780.
(80) Ma, K.; Yuen, J. M.; Shah, N. C.; Walsh, J. T., Jr.; Glucksberg, M. R.; Van Duyne, R. P. *Anal Chem* **2011**, *83*, 9146–9152.
(81) Sharma, B.; Ma, K.; Glucksberg, M. R.; Van Duyne, R. P. *J. Am. Chem. Soc.* **2013**, *135*, 17290–17293.
(82) Lucotti, A.; Tommasini, M.; Fazzi, D.; Del Zoppo, M.; Chalifoux, W. A.; Tykwinski, R. R.; Zerbi, G. *J. Raman Spectrosc.* **2012**, n/a–n/a.
(83) Li, M.; Cushing, S. K.; Zhang, J.; Suri, S.; Evans, R.; Petros, W. P.; Gibson, L. F.; Ma, D.; Liu, Y.; Wu, N. *ACS Nano* **2013**, *7*, 4967–4976.
(84) Lin, J.; Chen, R.; Feng, S.; Pan, J.; Li, Y.; Chen, G.; Cheng, M.; Huang, Z.; Yu, Y.; Zeng, H. *Nanomedicine* **2011**, *7*, 655–663.
(85) Feng, S.; Chen, R.; Lin, J.; Pan, J.; Wu, Y.; Li, Y.; Chen, J.; Zeng, H. *Biosensors and Bioelectronics* **2011**, *26*, 3167–3174.
(86) Feng, S.; Lin, D.; Lin, J.; Li, B.; Huang, Z.; Chen, G.; Zhang, W.; Wang, L.; Pan, J.; Chen, R.; Zeng, H. *Analyst* **2013**, *138*, 3967–3974.
(87) Feng, S.; Chen, R.; Lin, J.; Pan, J.; Chen, G.; Li, Y.; Cheng, M.; Huang, Z.; Chen, J.; Zeng, H. *Biosensors and Bioelectronics* **2010**, *25*, 2414–2419.
(88) Chen, X.; Huang, Z.; Feng, S.; Chen, J.; Wang, L.; Lu, P.; Zeng, H.; Chen, R. *Int J Nanomedicine* **2012**, *7*, 6115–6121.
(89) Sivanesan, A.; Witkowska, E.; Adamkiewicz, W.; Dziewit, L.; Kaminska, A.; Waluk, J. *Analyst* **2014**, *139*, 1037–1043.
(90) Cheng, I.F.; Chang, H.-C.; Chen, T.-Y.; Hu, C.; Yang, F.-L. *Sci Rep* **2013**, *3*.

(91) Faris, G.W.; Copeland, R. A. *Applied Optics,* **1997**, 36, 2686-2688.

References

Chapter 2.

1. S. Olsnes, K. Refsnes, and A. Pihl, *Nature*, 1974, **249**, 627–631.
2. R. M. Steeves, M. E. Denton, F. C. Barnard, A. Henry, and J. M. Lambert,

Biochemistry, 1999, **38**, 11677–11685.
3. B. Wang, C. Guo, M. Zhang, B. Park, and B. Xu, *J. Phys. Chem. B*, 2012, **116**, 5316–5322.
4. M. Lindauer, J. Wong, and B. Magun, *Toxins*, 2010, **2**, 1500–1514.
5. X.-Y. Chen, T. M. Link, and V. L. Schramm, *Biochemistry*, 1998, **37**, 11605–11613.
6. M. D. Keller, S. K. Majumder, and A. Mahadevan-Jansen, *Opt Lett*, 2009, **34**, 926–928.
7. M. V. Schulmerich, J. H. Cole, J. M. Kreider, F. Esmonde-White, K. A. Dooley, S. A. Goldstein, and M. D. Morris, *Appl Spectrosc*, 2009, **63**, 286–295.
8. N. A. Macleod and P. Matousek, *Appl Spectrosc*, 2008, **62**, 291A–304A.
9. P. Matousek, E. R. C. Draper, A. E. Goodship, I. P. Clark, K. L. Ronayne, and A. W. Parker, *Appl Spectrosc*, 2006, **60**, 758–763.
10. W. Cushley, M. J. Muirhead, F. Silva, J. Greathouse, T. Tucker, J. W. Uhr, and E. S. Vitetta, *Toxicon*, **22**, 265–277.
11. J. Audi, M. Belson, M. Patel, J. Schier, and J. Osterloh, *JAMA*, 2005, **294**, 2342.
12. S. M. Bradberry, K. J. Dickers, P. Rice, G. D. Griffiths, and J. A. Vale, *Toxicol Rev*, 2003, **22**, 65–70.
13. A. J. Haes, B. C. Giordano, and G. E. Collins, *Anal Chem*, 2006, **78**, 3758–3764.
14. L. S. Jackson, W. H. Tolleson, and S. J. Chirtel, *J. Agric. Food Chem.*, 2006, **54**, 7300–7304.
15. F. P. Jenkins, *Journal of the Science of Food and Agriculture*, 1963, **14**, 773–780.
16. X. He, S. Lu, L. W. Cheng, R. Rasooly, and J. M. Carter, *Journal of Food Protection*, 2008, **71**, 2053–2058.
17. L. S. Jackson, Z. Zhang, and W. H. Tolleson, *Journal of Food Science*, 2010, **75**, T65–T71.
18. S. R. Kalb and J. R. Barr, *Anal Chem*, 2009, **81**, 2037–2042.
19. T.-Y. Liu, K.-T. Tsai, H.-H. Wang, Y. Chen, Y.-H. Chen, Y.-C. Chao, H.-H. Chang, C.-H. Lin, J.-K. Wang, and Y.-L. Wang, *Nat Comms*, 2011, **2**, 538–.
20. D. S. Wilson and J. W. Szostak, *Annu. Rev. Biochem.*, 1999, **68**, 611–647.
21. M. Famulok, G. Mayer, and M. Blind, *Acc. Chem. Res.*, 2000, **33**, 591–599.
22. E. A. Lamont, L. He, K. Warriner, T. P. Labuza, and S. Sreevatsan, *Analyst*, 2011, **136**, 3884–3895.
23. L. He, E. Lamont, B. Veeregowda, S. Sreevatsan, C. L. Haynes, F. Diez-Gonzalez, and T. P. Labuza, *Chem. Sci.*, 2011, **2**, 1579–1582.
24. L. He, T. Rodda, C. L. Haynes, T. Deschaines, T. Strother, F. Diez-Gonzalez, and T. P. Labuza, *Anal Chem*, 2011.
25. C. L. Haynes, A. D. McFarland, and R. P. V. Duyne, *Anal Chem*, 2005, **77**, 338 A–346 A.
26. D. A. Stuart, J. M. Yuen, N. Shah, O. Lyandres, C. R. Yonzon, M. R. Glucksberg, J. T. Walsh, and R. P. Van Duyne, *Anal Chem*, 2006, **78**, 7211–7215.
27. W. R. Premasiri, J. C. Lee, and L. D. Ziegler, *J. Phys. Chem. B*, 2012, **116**, 9376–

9386.
28. Y. Ridente, J. Aubard, and J. Bolard, *FEBS Letters*, **446**, 283–286.
29. G. Trachta, B. Schwarze, B. Sägmüller, and G. Brehm, *Journal of molecular ...*, 2004.
30. M. Casella, A. Lucotti, M. Tommasini, M. Bedoni, E. Forvi, F. Gramatica, and G. Zerbi, *Spectrochimica Acta Part A: Molecular and Biomolecular Spectroscopy*, 2011, **79**, 915–919.
31. X. Wang, X. Qian, J. J. Beitler, Z. G. Chen, F. R. Khuri, M. M. Lewis, H. J. C. Shin, S. Nie, and D. M. Shin, *Cancer Res.*, 2011, **71**, 1526–1532.
32. M. Y. Sha, H. Xu, M. J. Natan, and R. Cromer, *J. Am. Chem. Soc.*, 2008, **130**, 17214–17215.
33. K. C. Bantz, H. D. Nelson, and C. L. Haynes, *J Phys Chem C Nanomater Interfaces*, 2012, **116**, 3585–3593.
34. N. G. Greeneltch, M. G. Blaber, A.-I. Henry, G. C. Schatz, and R. P. Van Duyne, *Anal Chem*, 2013, **85**, 2297–2303.
35. P. Negri, N. E. Marotta, L. A. Bottomley, and R. A. Dluhy, *Appl Spectrosc*, 2011, **65**, 66–74.
36. P. Lemler, W. R. Premasiri, A. Delmonaco, and L. D. Ziegler, *Anal Bioanal Chem*, 2014, **406**, 193–200.
37. T. Hasegawa, J. Nishijo, and J. Umemura, *Chemical Physics Letters*, **317**, 642–646.
38. F. S. de Siqueira e Oliveira, H. E. Giana, and L. Silveira, *J Biomed Opt*, 2012, **17**, 107004.
39. J. Romero-Pastor, C. Cardell, E. Manzano, Á. Yebra-Rodríguez, and N. Navas, *J. Raman Spectrosc.*, 2011, **42**, 2137–2142.
40. I. S. Patel, W. R. Premasiri, D. T. Moir, and L. D. Ziegler, *Journal of Raman spectroscopy : JRS*, 2008, **39**, 1660–1672.
41. C. Lee, W. Yang, and R. G. Parr, *Phys. Rev. B*, 1988, **37**, 785–789.
42. A. D. Becke, *J. Chem. Phys.*, 1996, **104**, 1040–1046.
43. A. D. Becke, *J. Chem. Phys.*, 1993, **98**, 5648–5652.
44. R. Krishnan, J. S. Binkley, R. Seeger, and J. A. Pople, *J. Chem. Phys.*, 1980, **72**, 650–654.
45. A. D. McLean and G. S. Chandler, *J. Chem. Phys.*, 1980, **72**, 5639–5648.
46. S. K. Teh, W. Zheng, K. Y. Ho, M. Teh, K. G. Yeoh, and Z. Huang, *Br. J. Cancer*, 2008, **98**, 457–465.
47. B. Mennucci, *Wiley Interdisciplinary Reviews: Computational Molecular Science*, 2012, **2**, 386–404.
48. S. Miertuš, E. Scrocco, and J. Tomasi, *Chemical Physics*, **55**, 117–129.
49. N. C. Shah, O. Lyandres, J. T. Walsh, M. R. Glucksberg, and R. P. Van Duyne, *Anal Chem*, 2007, **79**, 6927–6932.
50. A. I. Krylov and P. M. W. Gill, *Wiley Interdisciplinary Reviews: Computational Molecular Science*, 2013, **3**, 317–326.

51. Y. Wang, K. Lee, and J. Irudayaraj, *Chem. Commun. (Camb.)*, 2010, **46**, 613–615.
52. A. Barhoumi, D. Zhang, F. Tam, and N. J. Halas, *J. Am. Chem. Soc.*, 2008, **130**, 5523–5529.
53. O. Neumann, D. Zhang, F. Tam, S. Lal, P. Wittung-Stafshede, and N. J. Halas, *Anal Chem*, 2009, **81**, 10002–10006.
54. A. R. Herdt, S. M. Drawz, Y. Kang, and T. A. Taton, *Colloids and Surfaces B: Biointerfaces*, **51**, 130–139.
55. D. Shi, C. Song, Q. Jiang, Z.-G. Wang, and B. Ding, *Chem. Commun. (Camb.)*, 2013, **49**, 2533–2535.
56. A. Bonifacio, S. Dalla Marta, R. Spizzo, S. Cervo, A. Steffan, A. Colombatti, and V. Sergo, *Anal Bioanal Chem*, 2014.
57. C. A. Steinke, K. K. Reeves, J. W. Powell, S. A. Lee, Y. Z. Chen, T. Wyrzykiewicz, R. H. Griffey, and V. Mohan, *Journal of Biomolecular Structure and Dynamics*, 1997, **14**, 509–516.
58. S. Verma and F. Eckstein, *Annu. Rev. Biochem.*, 1998.
59. S. M. Nimjee, C. P. Rusconi, and B. A. Sullenger, *Annu. Rev. Med.*, 2005, **56**, 555–583.
60. S. C. Erfurth, E. J. Kiser, and W. L. Peticolas, *Proceedings of the …*, 1972.
61. P. H. Hsu and H. K. Chiang, *J. Raman Spectrosc.*, 2010.
62. G. C. Schatz, M. A. Young, and R. P. Duyne, in *Surface-enhanced Raman …*, Springer Berlin Heidelberg, 2006, vol. 103, pp. 19–45.
63. G. C. Schatz and R. P. Van Duyne, *Surface Science*, **101**, 425–438.
64. F. W. King and G. C. Schatz, *Chemical Physics*, **38**, 245–256.
65. M. A. Rothschild, M. Oratz, and S. S. Schreiber, *Hepatology*, 1988, **8**, 385–401.
66. M. V. Schulmerich, W. F. Finney, R. A. Fredricks, and M. D. Morris, *Appl Spectrosc*, 2006, **60**, 109–114.
67. M. Levy and A. E. Benaglia, *J. Biol. Chem.*, 1950, **186**, 829–847.
68. X. He, S. Lu, L. W. Cheng, R. Rasooly, and J. M. Carter, *Journal of Food Protection*, 71, 2053–2058.
69. P. Matousek, *Appl Spectrosc*, 2006, **60**, 1341–1347.
70. M. V. Schulmerich, K. A. Dooley, M. D. Morris, T. M. Vanasse, and S. A. Goldstein, *J Biomed Opt*, 2006, **11**, 060502.
71. W. Li, S. Seal, E. Megan, J. Ramsdell, K. Scammon, G. Lelong, L. Lachal, and K. A. Richardson, *J. Appl. Phys.*, 2003, **93**, 9553.

References

Chapter 3.

(1) Andreou, C.; Hoonejani, M. R.; Barmi, M. R.; Moskovits, M.; Meinhart, C. D.,

ACS Nano 2013, 7, 7157-7164.
(2) Bantz, K. C.; Meyer, A. F.; Wittenberg, N. J.; Im, H.; Kurtuluş, O.; Lee, S. H.; Lindquist, N. C.; Oh, S. H.; Haynes, C. L., Phys Chem Chem Phys 2011, 13, 11551-11567.
(3) Li, J. F.; Huang, Y. F.; Ding, Y.; Yang, Z. L.; Li, S. B.; Zhou, X. S.; Fan, F. R.; Zhang, W.; Zhou, Z. Y.; Wu, D. Y.; Ren, B.; Wang, Z. L.; Tian, Z. Q., Nature 2010, 464, 392-395.
(4) Sharma, B.; Cardinal, M. F.; Kleinman, S.; Greeneltch, N. G.; Frontiera, R. R.; Blaber, M. G.; Schatz, G. C.; Van Duyne, R. P. MRS Bulletin, 2013, 38, 615-624.
(5) Wustholz, K. L.; Henry, A. I.; McMahon, J. M.; Freeman, R. G.; Valley, N.; Piotti, M. E.; Natan, M. J.; Schatz, G. C.; Van Duyne, R. P., J Am Chem Soc 2010, 132, 10903-10910.
(6) Cao, Y. C.; Jin, R. C.; Nam, J.-M.; Thaxton, C. S.; Mirkin, C. A., J. Am. Chem. Soc., 2003, 125, 14676-14677.
(7) Cao, Y. W. C.; Jin, R. C.; Mirkin, C. A., Science, 2002, 297, 1536-1540.
(8) Aikens, C. M.; Madison, L. R.; Schatz, G. C., Nat. Photon, 2013, 7, 508-510.
(9) Li, Q.; Jiang, Y.; Han, R.; Zhong, X.; Liu, S.; Li, Z. Y.; Sha, Y.; Xu, D., Small, 2013, 9, 927-932.
(10) Neumann, O.; Zhang, D. M.; Tam, F.; Lal, S.; Wittung-Stafshede, P.; Halas, N. J., Anal Chem 2009, 81, 10002-10006.
(11) Fan, X.; White, I. M., Nat Photon 2011, 5, 591-597.
(12) Ravindranath, S. P.; Henne, K. L.; Thompson, D. K.; Irudayaraj, J., ACS Nano, 2011, 5, 4729-4736.
(13) Matschulat, A.; Drescher, D.; Kneipp, J., ACS Nano, 2010, 4, 3259-3269.
(14) Piorek, B. D.; Lee, S. J.; Moskovits, M.; Meinhart, C. D., Anal Chem 2012, 84, 9700-9705.
(15) Li, B.; Zhang, W.; Chen, L.; Lin, B. Electrophoresis 2013, 34, 2162–2168.
(16) Parisi, J.; Su, L.; Lei, Y. Lab Chip 2013, 13, 1501–1508.
(17) Mao, H.; Wu, W.; She, D.; Sun, G.; Lv, P.; Xu, J. Small 2013, 1-8.
(18) McMahon, J. M.; Henry, A. I.; Wustholz, K. L.; Natan, M. J.; Freeman, R. G.; Van Duyne, R. P.; Schatz, G. C., Anal Bioanal Chem 2009, 394, 1819-1825.
(19) Quang, L. X.; Lim, C.; Seong, G. H.; Choo, J.; Do, K. J.; Yoo, S. K., Lab Chip 2008, 8, 2214-2219.
(20) Connatser, R. M.; Cochran, M.; Harrison, R. J.; Sepaniak, M. J., Electrophoresis 2008, 29, 1441-1450.
(21) Liu, G. L.; Lee, L. P., Appl Phys Lett 2005, 87, 074101-074103.
(22) Haynes, C. L.; McFarland, A. D.; Van Duyne, R. P. Anal Chem 2005, 77, 338 A–346 A.
(23) Huang, J. A.; Zhao, A. Q.; Zhang, X. J.; He, L. F.; Wong, T. L.; Chui, Y. S.; Zhang, W. J.; Lee, S.; T., Nano Lett 2013 DOI: 10.1021/nl401920u.
(24) Lee, J. H.; Nam, J. M.; Jeon, K. S,; Lim, D. K.; Kim, H.; Kwon, S.; Lee, H.; Suh, Y. D., ACS Nano 2012, 6, 9574-9584.

(25) Qin, L. D.; Zou, S. L.; Xue, C.; Atkinson, A.; Schatz, G. C.; Mirkin, C. A., P. Natl. Acad. Sci, 2006, 103, 13300-13303.
(26) Im, H.; Bantz, K. C.; Lindquist, N.; Haynes, C. L., Oh, S.-H. Nano Lett 2010, 10, 2231-2236.
(27) Lee, S. H.; Bantz, K. C.; Lindquist, N.; Oh, S.-H.; Haynes, C. L. Langmuir 2009, 25, 13685-13693.
(28) Hulteen, J. C.; Young, M. A.; Van Duyne, R. P. Langmuir, 22, 10354-10364.
(29) Stuart, D. A.; Yonzon, C. R.; Zhang, X. Y.; Lyandres, O.; Shah, N. C.; Glucksberg, M. R.; Walsh, J. T.; Van Duyne, R. P., Anal Chem 2005, 77, 4013-4019.
(30) Giesfeldt, K. S.; Connatser, R. M.; De Jesús, M. A.; Dutta, P.; Sepaniak, M. J., J Raman Spectrosc 2005, 36, 1134-1142.
(31) Zhang, L. S.; Fang, Y.; Zhang, P. X., Chem Phys Lett 2008, 451, 102-105.
(32) Jeon, N. L.; Dertinger, S. K. W.; Chiu, D. T.; Choi, I. S.; Stroock, A. D.; Whitesides, G. M., Langmuir 2000, 16, 8311-8316.
(33) Kim, D.; Haynes, C. L., Anal Chem 2012, 84, 6070-6078.
(34) Pinkhasova, P.; Yang, L.; Zhang, Y.; Sukhishvili, S.; Du, H., Langmuir 2012, 28, 2529-2535.
(35) Chan, K.-Y.; Knipp, D.; Gordijn, A.; Stiebig, H., J Appl Phys 2008, 104, 054506-054506.
(36) Meillaud, F.; Vallat-Sauvain, E.; Shah, A.; Ballif, C., J Appl Phys 2008, 103, 054504-054505.
(37) Lohse, S. E.; Eller, J. R.; Sivapalan, S. T.; Plews, M. R.; Murphy, C. J. ACS Nano 2013, 7, 4135-4150.
(38) Rycenga, M.; Langille, M. R.; Personick, M. L.; Ozel, T.; Mirkin, C. A. Nano Letters 2012, 12, 6218-6222.
(39) Zhang, J.; Langille, M. R.; Personick, M. L. ; Zhang, K.; Li, S. ; Mirkin, C. A. J. Am. Chem. Soc., 2010, 132, 14012–14014.
(40) Murphy, C. J. J Mater Chem 2008, 18, 2173–2176.
(41) Orendorff, C. J.; Murphy, C. J. J Phys Chem B 2006, 110, 3990–3994.
(42) Sau, T. K.; Murphy, C. J. Langmuir 2004, 20, 6414–6420.
(43) Yang, W.-H.; Hulteen, J.; Schatz, G. C.; Van Duyne, R. P. J. Chem. Phys. 1996, 104, 4313–4323.
(44) Hulteen, J. C.; Young, M. A.; Van Duyne, R. P. Langmuir 2006, 22, 10354–10364.
(45) Tyler, T. P.; Henry, A. I.; Van Duyne, R. P. J. Phys. Chem. Lett. 2011, 2, 218-222.
(46) Liu, H.; Zhang, L.; Lang, X.; Yamaguchi, Y.; Iwasaki, H.; Inouye, Y.; Xue, Q.; Chen, M., Scientific Reports, 2011, 1, 112.
(47) Palonpon, A. F.; Ando, J.; Yamakoshi, H.; Dodo, K.; Sodeoka, M.; Kawata, S.; Fujita, K., Nat. Protocols, 2013, 8, 677-692.
(48) Wilson, R.; Monaghan, P.; Bowden, S. A.; Parnell, J.; Cooper, J. M., Anal Chem 2007, 79, 7036-7041.
(49) Lim, C.; Hong, J.; Chung, B. G.; deMello, A. J.; Choo, J., Analyst 2010, 135, 837-844.

(50) Zrimsek, A. B.; Henry, A.-I.; Van Duyne, R. P. J Phys Chem Lett 2013, 4, 3206-3210.
(51) Greeneltch, N. G.; Blaber, M. G.; Henry, A.-I.; Schatz, G. C.; Van Duyne, R. P. Anal Chem 2013, 85, 2297–2303.

References

Chapter 4.

(1) Anker, J. N.; Hall, W. P.; Lyandres, O.; Shah, N. C.; Zhao, J.; Van Duyne, R. P. *Nat Mater* **2008**, *7*, 442–453.
(2) Bantz, K. C.; Meyer, A. F.; Wittenberg, N. J.; Im, H.; Kurtuluş, O.; Lee, S. H.; Lindquist, N. C.; Oh, S.-H.; Haynes, C. L. *Phys Chem Chem Phys* **2011**, *13*, 11551–11567.
(3) Penn, S. G.; He, L.; Natan, M. J. *Current opinion in chemical biology* **2003**.
(4) Vo-Dinh, T.; Wang, H.-N.; Scaffidi, J. *J Biophotonics* **2009**, *3*, 89–102.
(5) Yang, J.; Palla, M.; Bosco, F. G.; Rindzevicius, T.; Alstrøm, T. S.; Schmidt, M. S.; Boisen, A.; Ju, J.; Lin, Q. *ACS Nano* **2013**, *7*, 5350–5359.
(6) Wang, F.; Widejko, R. G.; Yang, Z.; Nguyen, K. T.; Chen, H.; Fernando, L. P.; Christensen, K. A.; Anker, J. N. *Anal Chem* **2012**, *84*, 8013–8019.
(7) Bishnoi, S. W.; Rozell, C. J.; Levin, C. S.; Gheith, M. K.; Johnson, B. R.; Johnson, D. H.; Halas, N. J. *Nano Lett.* **2006**, *6*, 1687–1692.
(8) Maurer-Jones, M. A.; Bantz, K. C.; Love, S. A.; Marquis, B. J.; Haynes, C. L. *Nanomedicine (Lond)* **2009**, *4*, 219–241.
(9) Maurer-Jones, M. A.; Gunsolus, I. L.; Murphy, C. J.; Haynes, C.L. *Analytical Chemistry,* **2013**, *85*, 3036-3049.
(10) Ghosh, A.; Patra, C. R.; Mukherjee, P.;Sastry, M.; Kumar, R. *Microporous and Mesoporous Materials,* **2003**, 58, 201-211.
(11) Kang, J. S.; Taton, T. A. *Langmuir* **2012**, *28*, 16751–16760.
(12) McCreery, R. L. **2005**.
(13) Haes, A. J.; Haynes, C. L.; McFarland, A. D.; Schatz, G. C.; Van Duyne, R. P.; Zou, S. *MRS Bull.* **2011**, *30*, 368–375.
(14) Lin, Y.-S.; Abadeer, N.; Haynes, C. L. *Chem. Commun. (Camb.)* **2011**, *47*, 532–534.
(15) Angelomé, P. C.; Pastoriza-Santos, I.; Pérez-Juste, J.; Rodríguez-González, B.; Zelcer, A.; Soler-Illia, G. J. A. A.; Liz-Marzán, L. M. *Nanoscale* **2012**, *4*, 931–939.
(16) Tenzer, S.; Docter, D.; Kuharev, J.; Musyanovych, A.; Fetz, V.; Hecht, R.; Schlenk, F.; Fischer, D.; Kiouptsi, K.; Reinhardt, C.; Landfester, K.; Schild, H.; Maskos, M.; Knauer, S. K.; Stauber, R. H. **2013**, 1–10.

References

Chapter 5.

(1) International Society for Technology in Education. ISTE Standards http://www.iste.org/standards (accessed Mar 21, 2015).

(2) Technological Pedagogical and Content Knowledge. TPACK www.tpack.org (accessed Mar 21, 2015).

(3) Kehoe, E.; Penn, R. L. *J. Chem. Educ.* **2013**, *90*, 1191–1195.

(4) Bennett, J.; Pence, H. E. *J. Chem. Educ.* **2011**, *88*, 761–763.

(5) Spaeth, A. D.; Black, R. S. *J. Chem. Educ.* **2012**, *89*, 1078–1079.

(6) Purest Colloids. MesoGold® - Nanoparticle Colloidal Gold https://www.purestcolloids.com/mesogold.php (accessed Mar 21, 2015).

(7) McFarland, A. D.; Haynes, C. L.; Mirkin, C. A.; Van Duyne, R. P.; Godwin, H. A. *J. Chem. Educ.* **2004**, *81*, 544A.

(8) Google. Classroom https://classroom.google.com (accessed Mar 22, 2015).

Appendix A. Curriculum Vitae (CV)

Antonio Renteria Campos II

University of Minnesota
Department of Chemistry, College of Science and Engineering
97 Kolthoff Hall, 207 Pleasant Street S.E.
Minneapolis, MN 55455

Email: campo052@umn.edu
Phone: (612) 625-4236
Place/Date of Birth: El Paso, Texas on June 16, 1985

Education

2008	B.S., Chemistry, University of Texas at Austin, Austin, TX
2011	M.S., Chemistry, University of Minnesota, Minneapolis, MN
2015	Ph.D., Chemistry, University of Minnesota, Minneapolis, MN

Employment

2011	Research Assistant, Department of Chemistry, University of Minnesota,

Advisor: Christy L. Haynes

2010 Teaching Assistant, Waters Center of Innovation for Mass Spectrometry, Department of Chemistry, University of Minnesota, Director: Dr. Joe Dalluge

2009 Teaching Assistant, Analytical Chemistry, University of Minnesota

2008 Teaching Assistant, Analytical Chemistry, University of Texas

Project Experience

Detection of ricin B chain in human whole blood with aptamers *via* surface-enhanced Raman Spectroscopy

Gold nanoparticles for the detection of pesticides on fresh produce *via* localized surface plasmon resonance

Development of a combined microfluidic device and plasmonic surface to create a single experiment limit of detection assessment

Development of biologically stable and reversible pH sensitive gold nanosphere aggregates encapsulated in mesoporous silica

Assessment of the diffusion of small molecules to the surface of mesoporous coated gold nanorods *via* surface-enhanced Raman spectroscopy

Development of a galactose polymer for the detection of ricin on gold film-over-nanospheres substrates *via* surface-enhanced Raman spectroscopy

Technical Expertise

Raman Spectroscopy

Surface-enhanced Raman Spectroscopy

Mass Spectrometry (liquid chromatography, electrospray ionization, matrix-assisted laser desorption ionization)

Infrared Spectroscopy (IR and FTIR)

Nuclear Magnetic Resonance spectroscopy (NMR)

Atomic Force Microscopy (AFM)

Chemometric Analysis including principle component analysis (PCA) and hierarchical cluster analysis (HCA)

Awards and Recognition

2014	Federation of Analytical Chemistry and Spectroscopy Societies (FACSS) Student Poster Award
2014	Coblentz Society Student Award
2012	Federation of Analytical Chemistry and Spectroscopy Societies (FACSS) Student Poster Award
2008	National Science Foundation-Research Experience for Undergraduates (NSF-REU) Fellowship Program
2008	Department of Chemistry and Biochemistry Undergraduate Scholarship
2007	Pfizer Minority Scholarship

Peer-Reviewed Publication List

- A fresh look at the crystal violet lab with handheld camera colorimetry, Knutson, T.R., Knutson, C., Mozzetti, A., Campos, A.R., Haynes, C.L., Penn, R.L., *Journal of Chemical Education*, accepted.
- Microfluidic-SERS devices for one-shot limit-of-detection, Campos, A.R., Kim, D., Datt, A., Gao, Z., Rycenga, M., Burrows, N., Greeneltch, N.G.,

Mirkin, C.A., Murphy, C.J., Van Duyne, R.P., Haynes, C.L., *Analyst,* 139, 3227–3234 (2014).

- Rapid and ultra-sensitive *in situ* SERS detection using dielectrophoresis, Cherukulappurath, S., Lee, S. H., Campos, A.R., Haynes, C.L. and Oh, S.-H. *Chemistry of Materials*, 26, 2445-2452 (2014).

- Zeptomole detection of DNA nanoparticles by single-molecule fluorescence with magnetic field-directed localization, Cannon, B. Campos, A. R. Lewitz, Z., Willets, K. A., and Russell, R. *Anal. Biochem.* 431, 40–47 (2012)

Presentations

2014 Science Exchange (SciX), Poster Session, Reno, NV

2013 Science Exchange (SciX), Early Career Scientists in Raman Spectroscopy, Milwaukee, WI

2012 Federation of Analytical Chemistry and Spectroscopy Societies (FACSS), Poster Session, Kansas City, MO

2008 University of Texas, Department of Chemistry and Biochemistry, Scholarship Poster Session

2007 University of Texas, Department of Chemistry and Biochemistry, Scholarship Poster Session

Teaching Experience

- Analytical Chemistry (CH 456) at the University of Texas Fall 2008
- Advanced Analytical Chemistry (CH 376K) at the University of Texas Spring 2009
- Introductory Analytical Chemistry Lab (CHEM 2111) at the University of Minnesota, Fall 2009
- Process Analytical Chemistry Lab (CHEM 2121) at the University of Minnesota Spring 2010

Outreach Activities

2014	Nanotechnology outreach at White Bear Lake High School, Organized and presented to 50 AP Chemistry students about nanotechnology
2013	Green Chemistry and Green Engineering: Science for a Sustainable Future, Center for Sustainable Polymers, Volunteer for the Minnesota State Fair
2013	Student Representative of the University of Minnesota for SciX Conference
2013	Helped Organize 8th Annual "Chemistry Day" for West 7th Street Community Center
2012	Helped Organize 7th Annual "Chemistry Day" for West 7th Street Community Center

Professional Affiliations

- Society for Applied Spectroscopy (SAS)
- Coblentz Society

References

Prof. Christy Haynes (advisor)
chaynes@umn.edu
(612) 626-1096

Prof. Katherine Willets (undergraduate advisor)
kwillets@cm.utexas.edu
(512) 471-6488

Dr. Joe Dalluge (Director of the Mass Spectrometry Lab)
jdalluge@umn.edu
(612) 625-8099

Appendix B. Supporting Information Chapter 3.

1. Supplemental Data

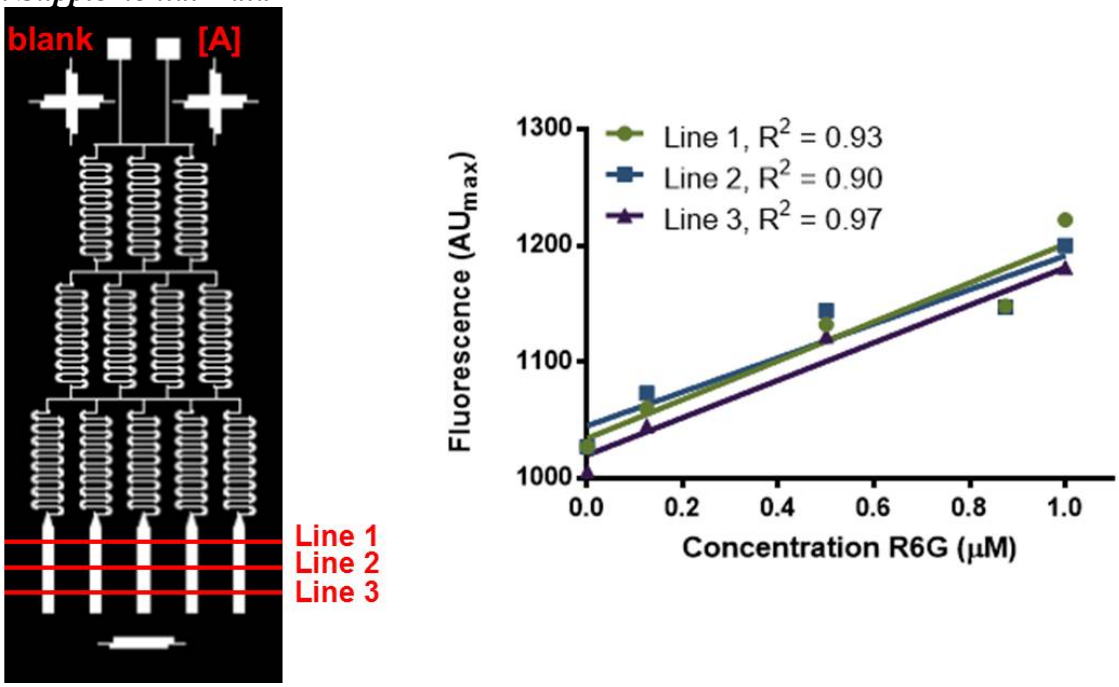

Figure S-1. (a) Device design and (b) Fluorescence response analysis for intra-device variation assessment.

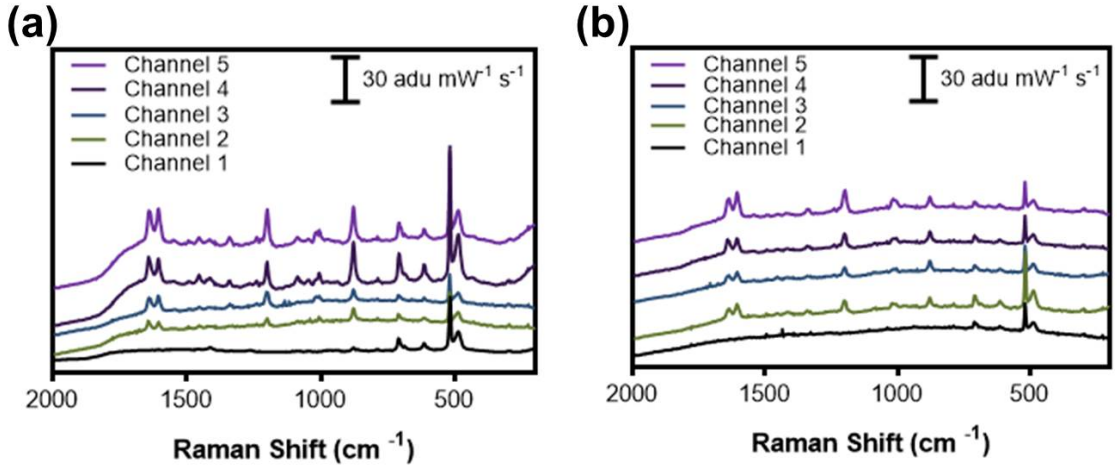

Figure S-2. 1 mM (a) BPE and (b) benzenethiol spectra obtained using the flexible SERS sensor prototype (i.e. with incorporated nanospheres).

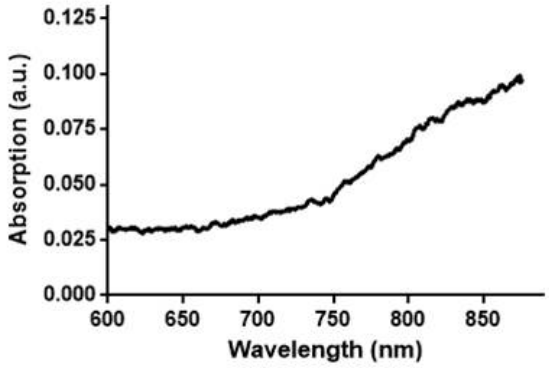

Figure S-3. Representative LSPR measurement performed on a AuNR-containing flexible SERS sensor.

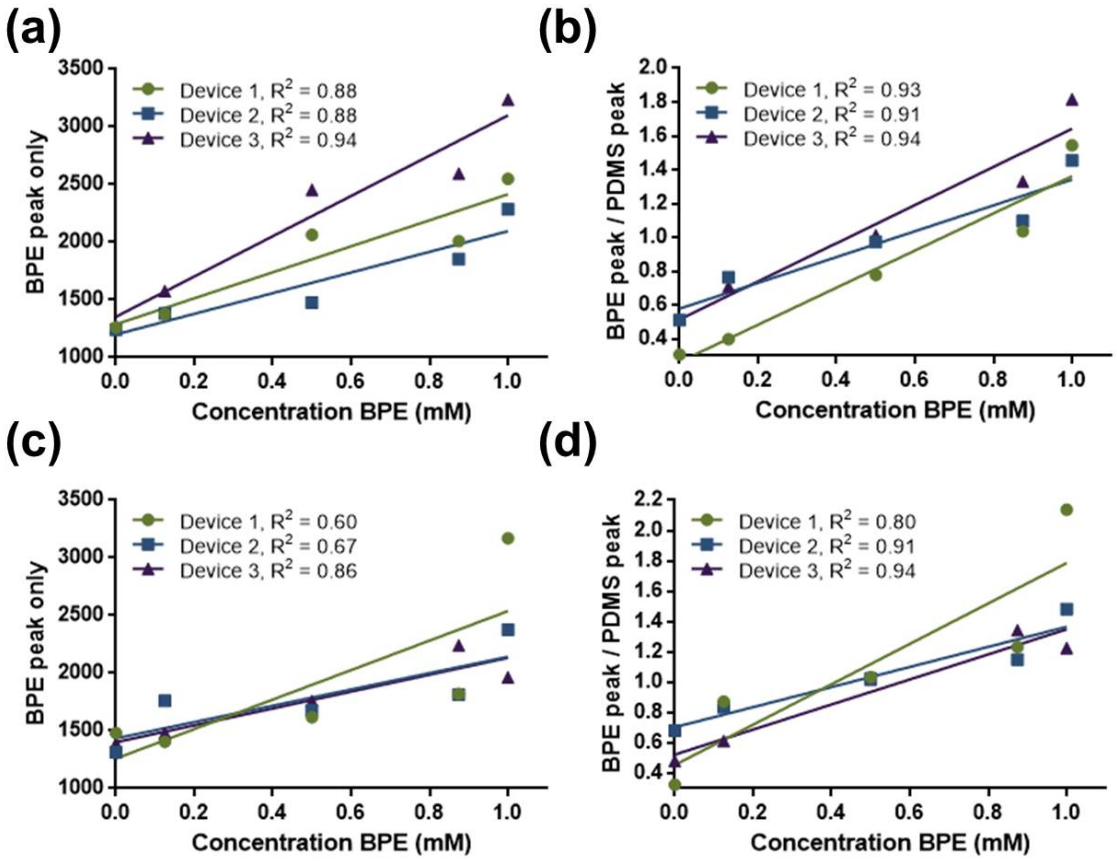

Figure S-4. SERS response analysis before (a and c) and after (b and d) the use of a PDMS peak as an intensity correction standard. (a) and (b) are from AuNR flexible SERS sensors and (c) and (d) are from AuNC flexible SERS sensors.

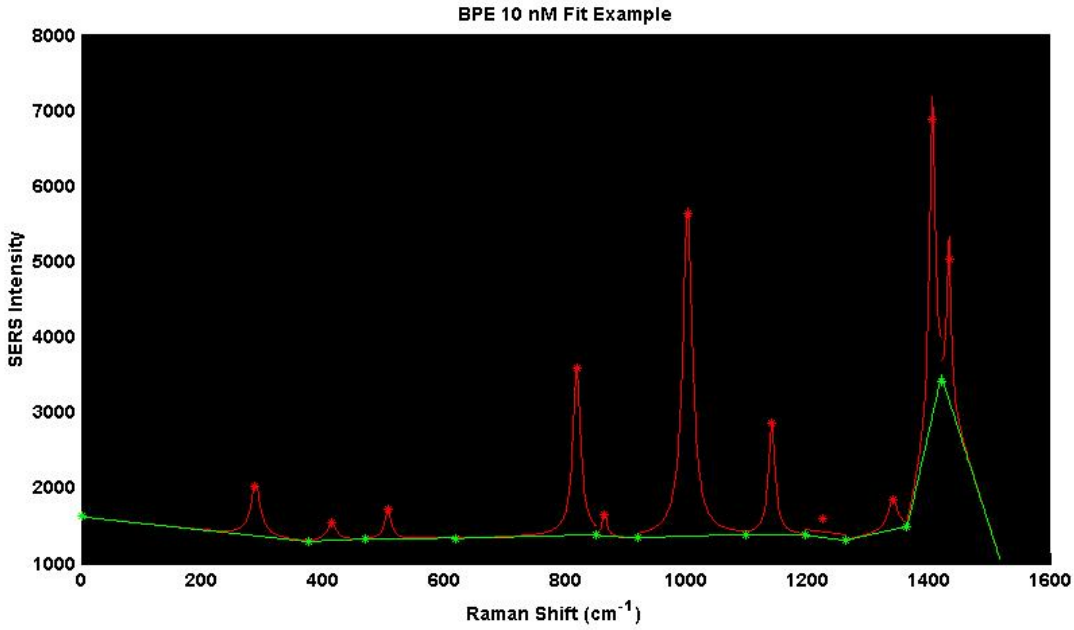

Figure S-5. MATLAB baseline fit (green line) of a BPE spectrum (red line) of a 10 nm solution of BPE. The peaks at 1610 and 1640 wavenumbers are not correctly resolved because of the overlapping nature of the peaks. The baseline fit of the peaks is not accurately fitting both peaks and therefore skews the area under the curve and does not yield the correct response. *Note: The x-axis was programmed to give the pixel number instead of the relative Raman shift in wavenumbers, however adding 200 to the x-axis gives the relative wavenumbers.

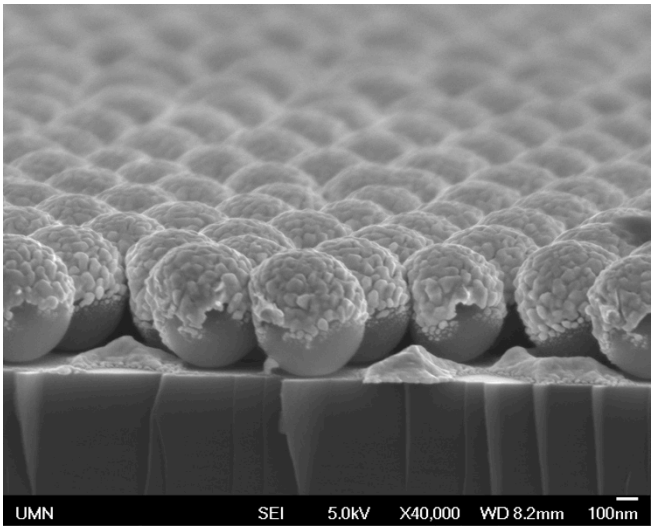

Figure S-6. SEM image of the cross-section view of the AuFON before incorporation with a PDMS microfluidic device.

2. Au nanosphere synthesis

Au nanospheres (AuNSs) for use in initial flexible SERS devices were synthesized under a nitrogen atmosphere while sonicating (Branson, Model 2510) using equimolar amounts of aqueous hydrogen tetrachloroaurate and sodium citrate for half an hour. The resulting purple solution was aged in the dark for 16 hours, with a final λ_{max} of 524 nm.[1]

3. Enhancement factor calculation

Enhancement factor calculation followed the method published by Wustholz et al (Eq. 1).[2]

$$\text{Enhancement Factor (EF)} = \frac{(N_{NRS} \times I_{SERS})}{(N_{SERS} \times I_{NRS})} \qquad \text{(Eq. 1)}$$

where N_{NRS} is the number of analyte molecules contributing to the normal Raman scattering measurement, N_{SERS} is the number of analyte molecules contributing to the

SERS measurement, I_{NRS} is the normal Raman scattering intensity of the analyte at a particular cm^{-1} shift, and I_{SERS} is SERS intensity of the analyte at an analogous cm^{-1} shift. In this calculation, we assume all molecules in the probe volume contribute equally to the measured signal. The value of N_{SERS} was estimated two different ways to account for potential variations in nanoparticle distribution in the PDMS layer: (1) uniformly using the in-device probe volume, considering excitation laser spot size (25-μm-diameter) and the microfluidic channel heights (100 μm) and (2) based on the nanoparticle coverage seen in the figure 4 SEM image (assuming that this coverage is representative and that the revealed nanoparticle surface area is hemispherical). Calculating the enhancement factor both ways presents a reasonable enhancement factor range for the flexible SERS microfluidic device. For the simple consideration of all molecules in the cylindrical probe volume experiencing enhancement (estimation #1): the laser spot size for SERS measurement (25-μm-diameter) was 490.9 μm^2 and the height of the microfluidic channel was 100 μm, yielding a probe volume (disregarding the possibility of sub-monolayer nanoparticle coverage) is:

$$490.9\ \mu m^2 \times 100\ \mu m = 4.9\times10^4\ \mu m^3$$

Using this probe volume:

$$N_{SERS} = 4.9 \times 10^4\ \mu m^3 \times \left(10^{-6}\right)^3\ m^3 \mu m^{-3} \times \frac{1 \times 10^{-3}\ mole}{10^{-3}\ m^3} \times 6.02 \times 10^{23}\ \frac{molecules}{mole} =$$

$$2.9 \times 10^{10} molecules$$

Using the SEM image in figure 4 and ImageJ software to calculate nanoparticle surface coverage (estimation #2): the nanoparticle surface area is 325.4 nm^2, and assuming each

nanoparticle presents a hemispherical surface protruding from the PDMS layer, we have a nanoparticle surface area within this imaged region of 650.8 nm^2. With a total imaged area of 4,385,700 nm^2, this yields a surface coverage of nanoparticles on the PDMS surface of 0.014%. With the laser spot size of 490.9 μm^2, the surface area of nanoparticles within the excitation laser spot is:

$$= 490.9\ \mu m^2 \times 0.00014 = 0.068\ \mu m^2$$

Assuming, optimistically, that all BPE molecules in the microfluidic channel can interact with the nanoparticles, we can get an estimated cylindrical probe volume of:

$$= 0.068\ \mu m^2 \times 100\ \mu m = 6.8\ \mu m^3$$

Thus,

$$N_{SERS} = 6.8\ \mu m^3 \times (10^{-6})^3\ m^3 \mu m^{-3} \times \frac{1 \times 10^{-3}\ mole}{10^{-3}\ m^3} \times 6.02 \times 10^{23} \frac{molecules}{mole}$$

$$= 4.1 \times 10^6 molecules$$

So, for the two assumptions, the number of molecules contributing to the measured SERS intensities range from 4.1 x 10^6 to 2.9 x 10^{10}. I_{SERS} for the 1200 cm^{-1} shift band, collected at 3 mW incident power for 10 seconds (matched to collection conditions for normal Raman spectra), was measured to be 4813 adus.

For normal Raman measurement on a 100 mM BPE solution, probe volume was determined using the scanning knife edge method[3] to be 0.0024 mm^3, and thus:

$$N_{NRS} = 1.4 \times 10^{14}$$

$$I_{NRS} = 4175 \text{ adus}$$

Thus, our estimated EF range for nanoparticles within the microfluidic device is:

$$EF = \frac{(1.4 \times 10^{14} \text{ molecules}) \times (4813 \text{ adus})}{(4.1 \times 10^{6} \text{ or } 2.9 \times 10^{10} \text{ molecules}) \times (4175 \text{ adus})} = 5.9 \times 10^{4}\text{-}4.1 \times 10^{7}$$

(1) Love, S. A.; Haynes, C. L. *Anal Bioanal Chem* **2010**, 398, 677–688.

(2) Wustholz, K. L.; Henry, A.-I.; McMahon, J. M.; Freeman, R. G.; Valley, N.; Piotti, M. E.; Natan, M. J.; Schatz, G. C.; Van Duyne, R. P. *J. Am. Chem. Soc.* **2010**, *132*, 10903-10910.

(3) Wustholz, K. L.; Henry, A.-I.; McMahon, J. M.; Freeman, R. G.; Valley, N.; Piotti, M. E.; Natan, M. J.; Schatz, G. C.; Van Duyne, R. P. *J. Am. Chem. Soc.* **2010**, 132, 10903–10910.

Appendix C. Python Coding for Principle Component Analysis

```
##########################################################################
##########
#   Copyright M. G. Blaber 2011, Edited and Updated A.R. Campos 2015
#   This file is part of SFP = Street Fighting Plasmonics
#   Street Fighting Plasmonics is free software: you can redistribute it
#   and/or modify it under the terms of the GNU General Public License as
#   published by the Free Software Foundation, either version 3 of the
#   License, or (at your option) any later version.
#
#   Foobar is distributed in the hope that it will be useful,
#   but WITHOUT ANY WARRANTY; without even the implied warranty of
#   MERCHANTABILITY or FITNESS FOR A PARTICULAR PURPOSE.  See the
#   GNU General Public License for more details.
#
#   You should have received a copy of the GNU General Public License
#   along with SFP.  If not, see <http://www.gnu.org/licenses/>.
##########################################################################
##########
#
# SFP_SERS_barcode.py
```

```
    #  version 0.03
    ##########################################################################
##########
    #Strings
    import string

    #Science
    import numpy
    from numpy import *
    from numpy.random import randn
    from scipy.interpolate import *

    #System
    import sys, os

    #Plotting
    import matplotlib
    import matplotlib.cm as cm
    import matplotlib.pyplot as plt
    from mpl_toolkits.mplot3d import Axes3D
```

```
    #Local
    from subroutines import readfile, normalize, func_deriv, smooth, remove_cosmic_rays
    ##########################################################################
##########


    #Parameters
    min_cm=200
    max_cm=2000


    variance_to_explain=0.999


    #Setup Fonts for plots etc
    matplotlib.rcParams['font.size'] = 12
    label_font_size=16
    tick_font_size=12


    lw=4.0 #Line Width
    use_colormap   =True  #If this is set to false the colormap turns into a rainbow.
    rainbow_multiplier=10 #This number should be lower for larger numbers of spectra.


    #2D Plots of data prior to PCA.
```

```
    figure_size=(8,10) #Inches
    plot_ysmooth   =True
    plot_dysmooth  =False
    plot_dydysmooth=True
    plot_binary    =True

    #3D Plots of PCA
    pca_figure_size=(10,8)
    plot_pca123    =True
    plot_pca234    =True
    include_3d_labels =False #This numbers each of the points in the 3d plot.
    #2d PCA plots.
    plot_eigenvectors=False #This are plots of the bits of the spectra which are important.
    plot_pca2d=True #Plot 6 2d plots: 1vs2, 1vs3


    ##########################################################################
##########
    #Find all of the files in the data directory.
    print "Finding data files"
    istep=0
```

```
    datalist=[]
    for datfile in os.listdir("./data/"):
        if (datfile[0] != "."):
            if os.path.isfile("./data/"+datfile):
                datalist.append("./data/"+datfile)
            #endif
        #if
    #next folder

    #Number of datasets
    ndatafiles=len(datalist)
    print "Number of datasets = %d"%(ndatafiles)

    ##########################################################################
##########
    #Sort out color table and assign colors to files
    print "Organizing Colors"
    #To edit these colors, visit: http://www.colorpicker.com/
    #Color Look up table:
    my_colors={ # string_in_filename:Color
        "dred":"#A10C01",
```

```
        "lred":"#FF8BA9",
        "lorange":"#FF8615",
        "dorange":"#D43400",
        "lgreen":"#26D800",
        "dgreen":"#257600",
        "lblue":"DodgerBlue",
        "dblue":"DarkBlue",
        "lpurple":"#CC49EB",
        "dpurple":"#6424C3"
    }

    color_data=[']*ndatafiles # Cell type stores the color information for each file.
    for id in range(ndatafiles):
        color_label=datalist[id].replace('./data/','').split('_')[0]
        if not color_label[0]==".":
            try:
                color_data[id]=my_colors[color_label]
            except:
                print "Oops! There is no valid color identifier in %s. The Color label found is
""%s"" "%(datalist[id],color_label)
                raise
```

```
        #try
      #if
   #for

   #Define Rainbow Spectra:
   rainbow_data=['']*ndatafiles
   for id in range(ndatafiles):
      rainbow_data[id]=cm.Set1(id*rainbow_multiplier)
   #for

   ####################################
   #Save the list of filenames and colors to disk
   print "Saving list of filenames and colors to disk"
   f=open("data_list.txt",'w')
   for id in range(ndatafiles):
      f.write("%d %s %s\n"%(id,datalist[id],color_data[id]))
   #for
   f.close()

   ##########################################################################
##########
```

```
    #Allocate Storage of raw dataset.

    ncm=1*int(max_cm-min_cm)+1
    xs = linspace(min_cm,max_cm, ncm)
    print "Interpolate data from %d cm-1 to %d cm-1 in %d steps"%(min_cm,max_cm,ncm)

    #STORAGE ARRAY
    print "Allocating the storage matrix"
    data_set=zeros((ndatafiles,ncm))
    print "size(data_set) = ",shape(data_set)

    ##########################################################################
##########

    id=-1
    for datfile in datalist:

        id+=1
```

```
print "%5d%5d %s"%(id,ndatafiles,datalist[id].replace('./data/',''))

#Read the data file. 1 and 2 are the column numbers that are being read.
raw_data=readfile(datalist[id],1,2)

#if this is the first id, then allocate the x and y arrays
if(id == 0 ):
   nrawx=len(raw_data)
   rawx=zeros([ndatafiles,nrawx])
   rawy=zeros([ndatafiles,nrawx])
   y_raw_smooth=zeros([ndatafiles,nrawx])
   y_smooth=zeros([ndatafiles,ncm])
   dy_smooth=zeros([ndatafiles,ncm])
   dydy_smooth=zeros([ndatafiles,ncm])
#if

#Save the Raw data
for ix in range(nrawx):
   rawx[id,ix]=raw_data[ix,0]
   rawy[id,ix]=raw_data[ix,1]
#for
```

```
#Remove Cosmic Rays. If you still have cosmic rays. Try decreasing max_diff.
remove_cosmic_rays(rawy[id,:],max_diff=2)

#Normalize The Data
normalize(rawy[id,:])

#smooth data
y_raw_smooth[id,:]=smooth(rawy[id,:],window_len=20,window='hanning')

#Create a function describing the smoothed y data.
y_smooth_f = UnivariateSpline(rawx[id,:],y_raw_smooth[id,:],s=0.000001)
#Create an array containing the smoothed data
y_smooth[id,:]=y_smooth_f(xs)

#Perform the first derivative calculation
for icm in range(ncm):
    dy_smooth[id,icm] = func_deriv(y_smooth_f,xs[icm])
#for

#smooth data
```

```
    #dy_smooth[id,:]=smooth(dy_smooth[id,:],window_len=50,window='hanning')



    #interpolate the dy_smooth
    dy_smooth_f = UnivariateSpline(xs[:],dy_smooth[id,:],s=0.000001)

    #Perform the second derivative calculation
    for icm in range(ncm):
       dydy_smooth[id,icm] = func_deriv(dy_smooth_f,xs[icm])
    #for

    #smooth data
    #dydy_smooth[id,:]=smooth(dydy_smooth[id,:],window_len=50,window='hanning')

    #Save the interpolated data.
    for icm in range(ncm):
       data_set[id,icm]=sign(dydy_smooth[id,icm])/2.0
    #for

#next datafile
```

```
    print "Done Reading Data Files"

    ##########################################################################
##########
    ##########################################################################
##########


    if (plot_ysmooth):
        plt.figure(1, figsize=figure_size, dpi=96, facecolor='w', edgecolor='k')
        plt.ylabel('Smoothed Intensity',fontsize=label_font_size)
        plt.xlabel('Wavenumber (cm^-1)',fontsize=label_font_size)
        for id in range(ndatafiles):
            mc=color_data[id] if use_colormap == True else rainbow_data[id]
            plt.plot(rawx[id,:],y_raw_smooth[id,:]+(id),c=mc,linewidth=lw,label="id
%d"%id)
        #next plot
        plt.legend(loc='best')
        plt.savefig('figures/PCA_YSmooth.png',dpi=300)
        plt.savefig('figures/PCA_YSmooth.pdf')
```

```
        plt.show()
    ##########################################################################
##########
    if (plot_dysmooth):
        plt.figure(2, figsize=figure_size, dpi=96, facecolor='w', edgecolor='k')
        plt.ylabel('First Derivative',fontsize=label_font_size)
        plt.xlabel('Wavenumber (cm^-1)',fontsize=label_font_size)
        for id in range(ndatafiles):
            mc=color_data[id] if use_colormap == True else rainbow_data[id]
            plt.plot(xs[:],dy_smooth[id,:]+(id)/30.0,c=mc,linewidth=lw,label="id %d"%id)
        #next plot
        plt.legend(loc='best')
        plt.savefig('figures/PCA_dYSmooth.png',dpi=300)
        plt.savefig('figures/PCA_dYSmooth.pdf')
        plt.show()
    #if
    ##########################################################################
##########
    if (plot_dydysmooth):
        plt.figure(2, figsize=figure_size, dpi=96, facecolor='w', edgecolor='k')
        plt.ylabel('Second Derivative',fontsize=label_font_size)
```

```
        plt.xlabel('Wavenumber (cm^-1)',fontsize=label_font_size)
        for id in range(ndatafiles):
            mc=color_data[id] if use_colormap == True else rainbow_data[id]
            plt.plot(xs[:],dydy_smooth[id,:]+(id)/80.0,c=mc,linewidth=lw,label="id %d"%id)
        #next plot
        plt.legend(loc='best')
        plt.savefig('figures/PCA_dYdYSmooth.png',dpi=300)
        plt.savefig('figures/PCA_dYdYSmooth.pdf')
        plt.show()
    #fi
    ##########################################################################
##########
    if (plot_binary):
        plt.figure(2, figsize=figure_size, dpi=96, facecolor='w', edgecolor='k')
        plt.ylabel('Binary',fontsize=label_font_size)
        plt.xlabel('Wavenumber (cm^-1)',fontsize=label_font_size)
        for id in range(ndatafiles):
            mc=color_data[id] if use_colormap == True else rainbow_data[id]
            offset=5.0*std(data_set[id,:])
            plt.plot(xs[:],data_set[id,:]+offset*id,c=mc,linewidth=0.5*lw,label="id %d"%id)
        #next plot
```

```
        plt.legend(loc='best')
        plt.savefig('figures/PCA_Binary.png',dpi=300)
        plt.savefig('figures/PCA_Binary.pdf')
        plt.show()
    #fi



    ##########################################################################
##########
    ##########################################################################
##########
    print "----------------------------------------------------------------"
    print "Starting PCA"

    import pca

    #Normalize the data
    data_set -= data_set.mean() / data_set.std()

    #Perform the Single Value Decomposition.
```

```
    p = pca.PCA(data_set, fraction=variance_to_explain )

    ##########################################################################
##########
    print "Number of PCs = %d"%(p.npc)

    #print the eigenvalues an the sum of the variance.
    #Only the first 3 or 4 numbers are important.
    print "%3s%20s%20s"%("i","EigenValue","Sum of Variance")
    for i in range (p.npc):
      print "%3d%20.5f%20.5f"%(i,p.eigen[i],p.sumvariance[i])
    #for

    pcs = p.pc()  # d' Vt' x

    nobs,nvars=data_set.shape
    print "Shape of Data, nobs, nvars = ", nobs,nvars

    nobs,npcs=pcs.shape
    print "Shape of pcs, npcs, nvars = ", npcs,nobs
```

```
#Plot Principal Components 1-3
if (plot_pca123):
    fig=plt.figure(6, figsize=pca_figure_size, dpi=96, facecolor='w', edgecolor='k')
    ax = fig.gca(projection='3d')
    mc=color_data if use_colormap == True else rainbow_data
    ax.scatter(pcs[:,0],pcs[:,1],pcs[:,2], c=mc, marker='o',s=100.0)
    if(include_3d_labels):
        for i in range(len(pcs[:,0])):
            ax.text(pcs[i,0],pcs[i,1],pcs[i,2], "%d"%i, color='black',fontsize=12)
        #for
    #if
    plt.xticks(fontsize=tick_font_size+4)
    plt.yticks(fontsize=tick_font_size+4)
    ax.set_xlabel('PC 1',fontsize=label_font_size)
    ax.set_ylabel('PC 2',fontsize=label_font_size)
    ax.set_zlabel('PC 3',fontsize=label_font_size)
    plt.savefig('figures/3D_PC123.pdf')
    plt.savefig('figures/3D_PC123.png',dpi=600)
    plt.show()
#IF
```

```
#Plot Principal Components 2-4
if (plot_pca234):
    fig=plt.figure(7, figsize=pca_figure_size, dpi=96, facecolor='w', edgecolor='k')
    ax = fig.gca(projection='3d')
    mc=color_data if use_colormap == True else rainbow_data
    ax.scatter(pcs[:,1],pcs[:,2],pcs[:,3], c=mc, marker='o',s=100.0)
    if(include_3d_labels):
        for i in range(len(pcs[:,0])):
            ax.text(pcs[i,1],pcs[i,2],pcs[i,3], "%d"%i, color='black',fontsize=12)
        #for
    #if
    plt.xticks(fontsize=tick_font_size+4)
    plt.yticks(fontsize=tick_font_size+4)
    ax.set_xlabel('PC 2',fontsize=label_font_size)
    ax.set_ylabel('PC 3',fontsize=label_font_size)
    ax.set_zlabel('PC 4',fontsize=label_font_size)
    plt.savefig('figures/3D_PC234.pdf')
    plt.savefig('figures/3D_PC234.png',dpi=600)
    plt.show()
```

```
    #IF


    #Plot eigenvectors of PCA.
    if (plot_eigenvectors):
        plt.figure(2, figsize=figure_size, dpi=96, facecolor='w', edgecolor='k')
        plt.ylabel('Eigenvector',fontsize=label_font_size)
        plt.xlabel('Wavenumber (cm^-1)',fontsize=label_font_size)
        #plt=pylab.scatter(pcs[:,1],pcs[:,2],marker='+',s=400)
        for ipc in range(npcs):
            mc=rainbow_data[ipc]
            offset=5.0*std(p.Vt[ipc])
            plt.plot(xs[:],p.Vt[ipc]+offset*ipc,c=mc,linewidth=lw/2.0,label="PC
%d"%(ipc+1))
        #for
        plt.xlim( (min_cm, max_cm) )
        plt.xticks(fontsize=tick_font_size)
        plt.yticks(fontsize=tick_font_size)
        #plt.legend()
        plt.legend(loc='best')
        plt.savefig('figures/PCA_Eigenvectors.png',dpi=300)
        plt.savefig('figures/PCA_Eigenvectors.pdf')
```

```
    plt.show()
#IF


if (plot_pca2d):
    fig=plt.figure(9, figsize=(12,8), dpi=96, facecolor='w', edgecolor='k')
    fig.subplots_adjust(left=0.08,right=0.95,wspace = 0.4,hspace=0.2)
    sp=[231,232,233,234,235,236]
    xl=[1,1,1,2,2,3]
    yl=[2,3,4,3,4,4]
    ax=['']*6
    for ip in range(6):
        print ip,sp[ip]
        ax[ip]=fig.add_subplot(sp[ip])
        ax[ip].set_xlabel('PC%1d'%xl[ip],fontsize=label_font_size)
        ax[ip].set_ylabel('PC%1d'%yl[ip],fontsize=label_font_size)
        mc=color_data if use_colormap == True else rainbow_data
        ax[ip].scatter(pcs[:,xl[ip]-1],pcs[:,yl[ip]-1], c=mc, marker='o',s=100.0)
    #next plot
    plt.savefig('figures/PCA_2D.png',dpi=300)
    plt.savefig('figures/PCA_2D.pdf')
    plt.show()
```

```
    #fi



    out_file = open("barcode-eigenvectors.dat", 'w')
    for i in range(len(xs)):
        out_file.write("%f %f %f %f %f
%f\n"%(xs[i],p.Vt[0,i],p.Vt[1,i],p.Vt[2,i],p.Vt[3,i],p.Vt[4,i]))
    out_file.close()


    out_file = open("barcode-eigenvalues.dat", 'w')
    for i in range(len(datalist)):
        out_file.write("%d %s %f %f %f
%f\n"%(i,datalist[i],pcs[i,0],pcs[i,1],pcs[i,2],pcs[i,3]))
    out_file.close()


    sys.exit()
```

Sub Routines

```
    ##########################################################################
##########
```

```
    import numpy
    from numpy import zeros,concatenate
    debug=False
    ##########################################################################
##########


    def readfile(filename, colx, coly):


        in_data=zeros((0,2))


    #This is pretty much the fastest way possible to read a file.
        file = open(filename)
        iline=0
        idataline=0
        for line in file:
            if " " in line:
                splitter=" "
            elif "," in line:
                splitter=","
            #if
            iline=iline+1
```

```
    s=line.strip().split(splitter)
    if(len(s)!=0):
        char1=s[0][0]
        if ( char1 == "#" or char1 == "!" or char1=="%" or char1=="W" ):
            #print("%s"%(line))
            donothing=1 #This is a placeholder. It  does nothing..
        else:
            #Make sure there are enough columns on this line
            if (len(s) < max(colx,coly) ):
                print "Error on line %d. Not enough columns"%(iline)
            else:
                idataline=idataline+1
                in_data=concatenate( ( in_data, [[float(s[colx-1]),float(s[coly-1])]] ) )
            #if
        #if
    #if
#for

ndata=len(in_data)
if(debug):
    print "Length of the file in lines = %d"%(iline)
```

```
            print "%7d:%14.8f %14.8f"%(0,in_data[0][0],in_data[0][1])
            print "%7d:%14.8f %14.8f"%(ndata,in_data[ndata-1][0],in_data[ndata-1][1])
        #if

        return in_data

    #end function

    ##########################################################################
##########

    def normalize(data):
        maxy=max(data[:])
        miny=min(data[:])
        norm_factor=maxy-miny
        for ix in range(len(data)):
            data[ix]=(data[ix]-miny)/norm_factor-0.5
        #for

    #def
```

```
    ##########################################################################
##########

    def func_deriv(f,x):
        #F is the function we're taking the derivative of, x is the parameter to give to f.
        # A ... X ... B
        dyb=0
        dya=5
        dx=0.002
        iloop=0
        while(abs(abs(dyb)-abs(dya))>0.001):
            dx=dx/2.0

            xa=x-dx
            xb=x+dx

            ya=f(xa)
            y=f(x)
            yb=f(xb)

            dya=y-ya
```

```
            dyb=yb-y

            iloop=iloop+1

            if (iloop>10):
               print "Derivative does not converge"
               return nan
            #if

         #while

         return (dya/dx+dyb/dx)/2.0
      #def func_deriv

      ##########################################################################
##########

      def remove_cosmic_rays(x,max_diff=10):


         if x.ndim != 1:
```

```
        raise ValueError, "smooth only accepts 1 dimension arrays."

    nx=len(x)

    stdev=numpy.std(x)
    #print stdev

    for i in range(1,nx):
        if ( abs(x[i]-x[i-1])>max_diff*stdev ):
            x[i]=x[i-1]
        #if
    #for

#end function

##########################################################################
##########

def smooth(x,window_len=10,window='hanning'):
    """smooth the data using a window with requested size.
```

This method is based on the convolution of a scaled window with the signal.
The signal is prepared by introducing reflected copies of the signal
(with the window size) in both ends so that transient parts are minimized
in the begining and end part of the output signal.

input:
    x: the input signal
    window_len: the dimension of the smoothing window; should be an odd integer
    window: the type of window from 'flat', 'hanning', 'hamming', 'bartlett', 'blackman'
        flat window will produce a moving average smoothing.

output:
    the smoothed signal

example:

t=linspace(-2,2,0.1)
x=sin(t)+randn(len(t))*0.1
y=smooth(x)

see also:

```
    numpy.hanning, numpy.hamming, numpy.bartlett, numpy.blackman, numpy.convolve
    scipy.signal.lfilter

    TODO: the window parameter could be the window itself if an array instead of a string
    """

    if x.ndim != 1:
        raise ValueError, "smooth only accepts 1 dimension arrays."

    if x.size < window_len:
        raise ValueError, "Input vector needs to be bigger than window size."


    if window_len<3:
        return x


    if not window in ['flat', 'hanning', 'hamming', 'bartlett', 'blackman']:
```

```
        raise ValueError, "Window is on of 'flat', 'hanning', 'hamming', 'bartlett',
'blackman'"

    x0=x[window_len-1:0:-1]
    xn=x[-1:-window_len:-1]
    s=numpy.r_[x0,x,xn]
    #print(len(s))
    if window == 'flat': #moving average
        w=numpy.ones(window_len,'d')
    else:
        w=eval('numpy.'+window+'(window_len)')

    y=numpy.convolve(w/w.sum(),s,mode='valid')

    #print "x0 = ",len(x0)
    #print "x  = ",len(x)
    #print "xn = ",len(xn)
    #print "y  = ",len(y)
    lx0=len(x0)
    if lx0 % 2 != 0:
        lx0=lx0+1
```

```
    #if
    #print "x0 = ",lx0
    ly=len(y)
    y=y[lx0/2:ly-len(xn)/2]

    #print "y  = ",len(y)

    return y

#end function
```

Principle Component Analysis

```
#!/usr/bin/env python
""" a small class for Principal Component Analysis
Usage:
    p = PCA( A, fraction=0.90 )
In:
    A: an array of e.g. 1000 observations x 20 variables, 1000 rows x 20 columns
    fraction: use principal components that account for e.g.
        90 % of the total variance

Out:
```

p.U, p.d, p.Vt: from numpy.linalg.svd, A = U . d . Vt

p.dinv: 1/d or 0, see NR

p.eigen: the eigenvalues of A*A, in decreasing order (p.d**2).

eigen[j] / eigen.sum() is variable j's fraction of the total variance;

look at the first few eigen[] to see how many PCs get to 90 %, 95 % ...

p.npc: number of principal components,

e.g. 2 if the top 2 eigenvalues are >= `fraction` of the total.

It's ok to change this; methods use the current value.

Methods:

The methods of class PCA transform vectors or arrays of e.g.

20 variables, 2 principal components and 1000 observations,

using partial matrices U' d' Vt', parts of the full U d Vt:

A ~ U' . d' . Vt' where e.g.

U' is 1000 x 2

d' is diag([d0, d1]), the 2 largest singular values

Vt' is 2 x 20. Dropping the primes,

d . Vt 2 principal vars = p.vars_pc(20 vars)

U 1000 obs = p.pc_obs(2 principal vars)

U . d . Vt 1000 obs, p.obs(20 vars) = pc_obs(vars_pc(vars))

fast approximate A . vars, using the `npc` principal components

Ut 2 pcs = p.obs_pc(1000 obs)

V . dinv 20 vars = p.pc_vars(2 principal vars)

V . dinv . Ut 20 vars, p.vars(1000 obs) = pc_vars(obs_pc(obs)),

fast approximate Ainverse . obs: vars that give ~ those obs.

Notes:

PCA does not center or scale A; you usually want to first

A -= A.mean(A, axis=0)

A /= A.std(A, axis=0)

with the little class Center or the like, below.

See also:

http://en.wikipedia.org/wiki/Principal_component_analysis

http://en.wikipedia.org/wiki/Singular_value_decomposition

Press et al., Numerical Recipes (2 or 3 ed), SVD

PCA micro-tutorial

iris-pca .py .png

```
"""

from __future__ import division
import numpy as np
dot = np.dot
    # import bz.numpyutil as nu
    # dot = nu.pdot

__version__ = "2010-04-14 apr"
__author_email__ = "denis-bz-py at t-online dot de"

#...............................................................................
class PCA:
    def __init__( self, A, fraction=0.90 ):
        assert 0 <= fraction <= 1
        # A = U . diag(d) . Vt, O( m n^2 ), lapack_lite --
        self.U, self.d, self.Vt = np.linalg.svd( A, full_matrices=False )
        assert np.all( self.d[:-1] >= self.d[1:] )  # sorted
        self.eigen = self.d**2
        self.sumvariance = np.cumsum(self.eigen)
        self.sumvariance /= self.sumvariance[-1]
```

```
    self.npc = np.searchsorted( self.sumvariance, fraction ) + 1
    self.dinv = np.array([ 1/d if d > self.d[0] * 1e-6  else 0
                           for d in self.d ])

def pc( self ):
    """ e.g. 1000 x 2 U[:, :npc] * d[:npc], to plot etc. """
    n = self.npc
    return self.U[:, :n] * self.d[:n]

# These 1-line methods may not be worth the bother;
# then use U d Vt directly --

def vars_pc( self, x ):
    n = self.npc
    return self.d[:n] * dot( self.Vt[:n], x.T ).T  # 20 vars -> 2 principal

def pc_vars( self, p ):
    n = self.npc
    return dot( self.Vt[:n].T, (self.dinv[:n] * p).T ) .T  # 2 PC -> 20 vars

def pc_obs( self, p ):
```

```
        n = self.npc
        return dot( self.U[:, :n], p.T )  # 2 principal -> 1000 obs

    def obs_pc( self, obs ):
        n = self.npc
        return dot( self.U[:, :n].T, obs ) .T  # 1000 obs -> 2 principal

    def obs( self, x ):
        return self.pc_obs( self.vars_pc(x) )  # 20 vars -> 2 principal -> 1000 obs

    def vars( self, obs ):
        return self.pc_vars( self.obs_pc(obs) )  # 1000 obs -> 2 principal -> 20 vars


class Center:
    """ A -= A.mean() /= A.std(), inplace -- use A.copy() if need be
        uncenter(x) == original A . x
    """
        # mttiw
    def __init__( self, A, axis=0, scale=True, verbose=1 ):
        self.mean = A.mean(axis=axis)
```

```
        if verbose:
            print "Center -= A.mean:", self.mean
        A -= self.mean
        if scale:
            std = A.std(axis=axis)
            self.std = np.where( std, std, 1. )
            if verbose:
                print "Center /= A.std:", self.std
            A /= self.std
        else:
            self.std = np.ones( A.shape[-1] )
        self.A = A

    def uncenter( self, x ):
        return np.dot( self.A, x * self.std ) + np.dot( x, self.mean )


#...............................................................................
if __name__ == "__main__":
    import sys
```

```
csv = "iris4.csv"  # wikipedia Iris_flower_data_set
   # 5.1,3.5,1.4,0.2  # ,Iris-setosa ...
N = 1000
K = 20
fraction = .90
seed = 1
exec "\n".join( sys.argv[1:] )  # N= ...
np.random.seed(seed)
np.set_printoptions( 1, threshold=100, suppress=True )  # .1f
try:
   A = np.genfromtxt( csv, delimiter="," )
   N, K = A.shape
except IOError:
   A = np.random.normal( size=(N, K) )  # gen correlated ?

print "csv: %s  N: %d  K: %d  fraction: %.2g" % (csv, N, K, fraction)
Center(A)
print "A:", A

print "PCA ..." ,
p = PCA( A, fraction=fraction )
```

```
print "npc:", p.npc
print "% variance:", p.sumvariance * 100

print "Vt[0], weights that give PC 0:", p.Vt[0]
print "A . Vt[0]:", dot( A, p.Vt[0] )
print "pc:", p.pc()

print "\nobs <-> pc <-> x: with fraction=1, diffs should be ~ 0"
x = np.ones(K)
# x = np.ones(( 3, K ))
print "x:", x
pc = p.vars_pc(x)  # d' Vt' x
print "vars_pc(x):", pc
print "back to ~ x:", p.pc_vars(pc)

Ax = dot( A, x.T )
pcx = p.obs(x)  # U' d' Vt' x
print "Ax:", Ax
print "A'x:", pcx
print "max |Ax - A'x|: %.2g" % np.linalg.norm( Ax - pcx, np.inf )
```

```
    b = Ax  # ~ back to original x, Ainv A x
    back = p.vars(b)
    print "~ back again:", back
    print "max |back - x|: %.2g" % np.linalg.norm( back - x, np.inf )

# end pca.py
```